BUBBLES AND SOFT-MATERIALS: FROM COMPUTATIONAL MODELING TO APPLICATIONS.

Thesis submitted for the fulfilment of the requirements for the Degree of Doctor of Philosophy

by

Armand Anthony Shams

School of Science & Technology,

Department of Mechanical Engineering & Aeronautics,

October 2023.

To my loved ones.

Acknowledgments

Embarking on this Ph.D. has been akin to navigating uncharted waters, and I have been fortunate to have a crew of supporters guiding me through every storm.

First and foremost, I would like to express my deepest gratitude to Prof. Gavaises, my advisor. His unwavering support, insightful guidance, and constant encouragement have been invaluable throughout this journey. I am deeply grateful for his mentorship and the opportunities he has provided me.

I would also like to extend my heartfelt thanks to Dr. Paquette and Dr. Papoutsakis for their scientific support and moral guidance during the first two years of my Ph.D. Their expertise and advice were crucial in shaping my research and helping me navigate the early challenges of this endeavor.

A special thanks goes to Saeed; our friendship has been a cornerstone of this journey. We have pushed each other forward, celebrated each milestone together, and faced every challenge with mutual support. I could not have asked for a better friend and colleague.

My appreciation also extends to the A306 crew. The camaraderie and friendships we forged have made this journey not only bearable but truly enjoyable. Although we started as colleagues, many of us have become lifelong friends, and I cherish the memories we created together.

I am profoundly grateful to my family and Elina for their continuous support, love, and understanding. Their encouragement has been my anchor, and their belief in me has kept me motivated through the toughest times.

Finally, I would like to thank City University for providing the necessary facilities that enabled this research and the European Commission for the generous research grant that made this work possible. Your support has been instrumental in the completion of this thesis.

ABSTRACT

Bubbles and ultrasound in biomedical applications often involve large to extreme deformations of the surrounding medium which conventional models fail to handle. The present work introduces a novel unified numerical model for compressible multi-material flows with block-structured adaptive mesh refinement. The five-equation diffuse interface model is expanded to include Eulerian hyperelasticity. This is done by tracking deformations of all solid materials with a conservation law for the elastic stretch tensor. Thus, the model is applicable to any arbitrary number of interacting fluid and solid materials. Subsequently, the capabilities of the model are showcased by investigating the potential for mechanical, and later by incorporating complex thermodynamics, thermal damage in ultrasound-induced collapse of air bubbles near soft materials. Firstly, the results reveal that soft materials primarily experience tensile forces during these interactions, suggesting potential tensile-driven injuries that may occur in relevant treatments. The bubble radius was found to play a crucial role in dictating the stresses experienced by the tissue, underscoring its significance in medical applications. It is documented that while early bubble dynamics remain relatively unaffected by changes in shear modulus of the soft material, at later stages the penetration processes and the deformation shapes, exhibit notable variations. Secondly, the lack of accuracy of commonly used equation of states (EoS) such as the stiffened-gas (SG) EoS is depicted through a compression case and spherical bubble collapse. It was found that the SG EoS can lead to up to 800% error in the predicted temperature at a 10GPa compression compared to the IAPWS EoS. Moreover, the fake temperature front observed in the spherical bubble collapse when using SG is alleviated by using IAPWS, the Modified Tait or the MNASG EoSs. Then, the rigid-wall heating in lithotripter pulse induced collapse of an air bubble is investigated. A significant temperature increase of 25K was observed at the lowest selected standoff distance which could lead to thermal damage. Thirdly, motived by the latest work on temperature predictions by real-fluid EoSs, the multi-material model was extended to complex thermodynamics. The temperatures induced in ultrasound-driven bubble collapses near soft materials was examined utilizing the RKPR EoS in tabulated format and the MNASG in parametric form. Three primary heating mechanisms were identified, with the highest temperature resulting from post-collapse shock. Findings reveal smaller bubbles induce stronger shocks and higher temperatures, while

increased standoff distances diminish maximum temperatures due to spherical shock propagation and rapid gas cooling on approaching soft materials.

PRESENT CONTRIBUTION

The major contributions and novelty of the present thesis can be summarized in the following points:

- **Development of a multi-material diffusive interface model incorporating complex thermodynamics with block-structured adaptive mesh refinement.**

A novel model based on the five-equation DIM is outlined, augmented by the kinematic equations of the stretch tensor. Unlike the previously published Eulerian hyperelasticity models, the current model only uses a single kinematic equation to track all deformations. Moreover, previous publications utilized the HLLC Riemann solver where the shear waves were modeled as a contact discontinuity, thus making the shear waves overly diffusive. Here, the HLLD Riemann solver was utilized, which introduces a family of slow waves used to model the shear waves. A block-structured AMR with local time-stepping was utilized to accurately solve the different scales of the multi-material flow and preserve the sharpness of the interfaces and waves. Later, the model is extended to include complex thermodynamic utilizing an iterative method to compute the mixture pressure. The thermodynamics of each material can be separately modelled by using different EoSs in tabulated or parametric form.

- **A comprehensive analysis of mechanical loads experienced by the soft material during ultrasound-induced bubble collapse.**

The findings of the study reveal that the tissue predominantly experiences tensile forces compared to compressive or shear forces, indicating that injuries are predominantly tensile-driven. The areas of maximum tensile forces where tissue injury could incur are shown. Furthermore, the bubble radius is identified to play a pivotal role in the stresses experienced by the soft material, emphasizing its importance in medical applications. Meanwhile, variations in shear modulus, while having a minimal impact on early bubble dynamics, noticeably influence the penetration process in later stages as well as the shape of the deformations.

- **Prediction of temperature using real-fluid equation of state.**

The deficiencies of common EoSs for the liquid state ought to both the unphysical specific heat ratio and the absence of terms considering repulsive molecular effects, is demonstrated. It is observed that the SG EoS leads to above 800% error in temperature rise compared to the

prediction obtained with the IAPWS one, at the highest compression of 10 GPa investigated. Moreover, the more complex and accurate modified Tait and IAPWS EoS can resolve and eliminate the spurious liquid temperature front that is predicted when the SG EoS is used, and which can be as high as 400 K.

- **Temperatures produced during ultrasound-driven collapse of air bubbles near soft materials.**

After showing the importance of using real-fluid EoS for predicting temperature, the complex thermodynamics methodology previously employed is incorporated into the multi-material model to study the heating in ultrasound-induced bubble collapse near a soft material. The findings reveal that three heating mechanisms are present. Firstly, the ultrasound propagating inside the soft material. Secondly, the shock emitted by the bubble's collapse which is the mechanism that produces the highest temperature although momentary. Thirdly, after the bubble collapses, it migrates toward the soft material and makes contact heating it up in the process. However, the bubble contact mechanism becomes less important as the standoff distance increases since the gas has time to cool down while moving downstream. Meanwhile, the heating experienced by the shock emitted at the bubble's collapse is observable at all standoff distances although greatly diminished. Furthermore, the analysis showed that smaller bubbles produce higher temperatures, especially upon collapse, and significantly enhance heating when in contact with the soft material.

DECLARATION

I hereby declare that the content of this dissertation is original and has not been submitted in whole or in part for consideration for any other degree or qualification in this, or any other university. This dissertation is my own work, except where specific reference is made to a joint effort in the text and acknowledged accordingly.

I grant powers of discretion to the University Librarian to allow the thesis to be copied in whole or in part without further reference to me. This permission covers only single copies made for study purposes, subject to normal conditions of acknowledgment.

TABLE OF CONTENTS

LIST OF FIGURES

LIST OF TABLES

NOMENCLATURE

Abbreviations

0D	Zero-Dimensional
1D	One-Dimensional
2D	Two-Dimensional
3D	Three-Dimensional
ALE	Arbitrary-Lagrangian-Eulerian
AMR	Adaptive Mesh Refinement
AUSM	Advection Upstream Splitting Method
BEM	Boundary Element Method
BIM	Boundary Integral Method
CFD	Computational Fluid Dynamics
CFL	Courant–Friedrichs–Lewy
DIM	Diffuse Interface Method
ESWL	Extracorporeal Shock Wave Lithotripsy
FEM	Finite Element Method
FSI	Fluid-Structure Interaction
GFM	Ghost Fluid Method
HIFU	High Intensity Focused Ultrasound
HLL	Harten-Lax-van Leer
HLLC	Harten-Lax-van Leer-Contact
HLLD	Harten-Lax-van Leer discontinuities
IAPWS	International Association for the Properties of Water and Steam
IB	Immersed Boundary
IG	Ideal Gas

MNASG	Modified Noble-Able Stiffened Gas
MUSCL	Monotonic Upstream-centered Scheme for Conservation Laws
NASG	Noble-Able Stiffened Gas
NIST	National Institute of Standards and Technology
PR	Peng-Robinson
RKPR	Redlich-Kwong-Peng-Robinson
SG	Stiffened Gas
SWL	Shock Wave Lithotripsy
UC	Ultrasonic Cavitation
UCA	Ultrasound Contrast Agent
VOF	Volume Of Fluid
WENO	Weighted Essentially Non-Oscillatory

1 INTRODUCTION

1.1 MOTIVATION

Bubbles and ultrasound have found vast medical applications, ranging from diagnostic to therapeutic procedures [1], [2], [3]. Ultrasound Contrast Agents (UCAs) are encapsulated microbubbles, either liquid-filled or gas-filled with a lipid or protein layer, introduced into the bloodstream for enhanced sonographic visualization, utilizing the acoustic signals they emit under ultrasound fields and the resulting backscattering for targeted imaging [4]. High-intensity focused Ultrasound (HIFU) is a therapeutic technique utilizing ultrasound waves to thermally ablate targeted tissues, particularly in cancer treatments [5], by generating localized heat, although concerns exist regarding its safety and potential tissue damage [6]. Histotripsy, an alternative to HIFU, aims to mechanically create tissue lesions without thermal coagulation, utilizing the shear stress from the expanding and contracting cavitation cloud for tissue bisection [7]. Alternatively, boiling histotripsy leverages HIFU-induced boiling for precise tissue emulsification using longer pulses and lower peak pressures, driven by shock fronts, tissue heating, and localized boiling, offering more predictable outcomes than conventional cavitation-based histotripsy [8]. Extracorporeal Shock Wave Lithotripsy (ESWL) is a non-invasive treatment for urinary lithiasis that utilizes focused shock waves to fragment kidney and ureteral stones, primarily through the generation and collapse of cavitation bubbles; however, this mechanism can also induce trauma to thin-walled vessels in the kidneys and adjacent tissues, leading to potential complications such as hemorrhage and inflammation [9].

1.2 PROBLEM DESCRIPTION

Understanding the dynamics of air bubbles in a liquid medium near soft biological tissues is crucial for enhancing the effectiveness and safety of medical treatments such as High-Intensity Focused Ultrasound (HIFU), Histotripsy, and Extracorporeal Shock Wave Lithotripsy (ESWL). These procedures rely on precise control of bubble dynamics to avoid unintended tissue damage and improve therapeutic outcomes.

In this research, we investigate the behavior of an air bubble introduced in a liquid medium, situated close to a soft material. The system is subjected to ultrasound waves, which induce

oscillations and potential collapse of the bubble. This setup mimics conditions found in various medical treatments, where understanding bubble dynamics is essential for optimizing therapeutic efficacy and minimizing side effects. It is important to note that our study considers air bubbles and does not account for the presence of vapor bubbles.

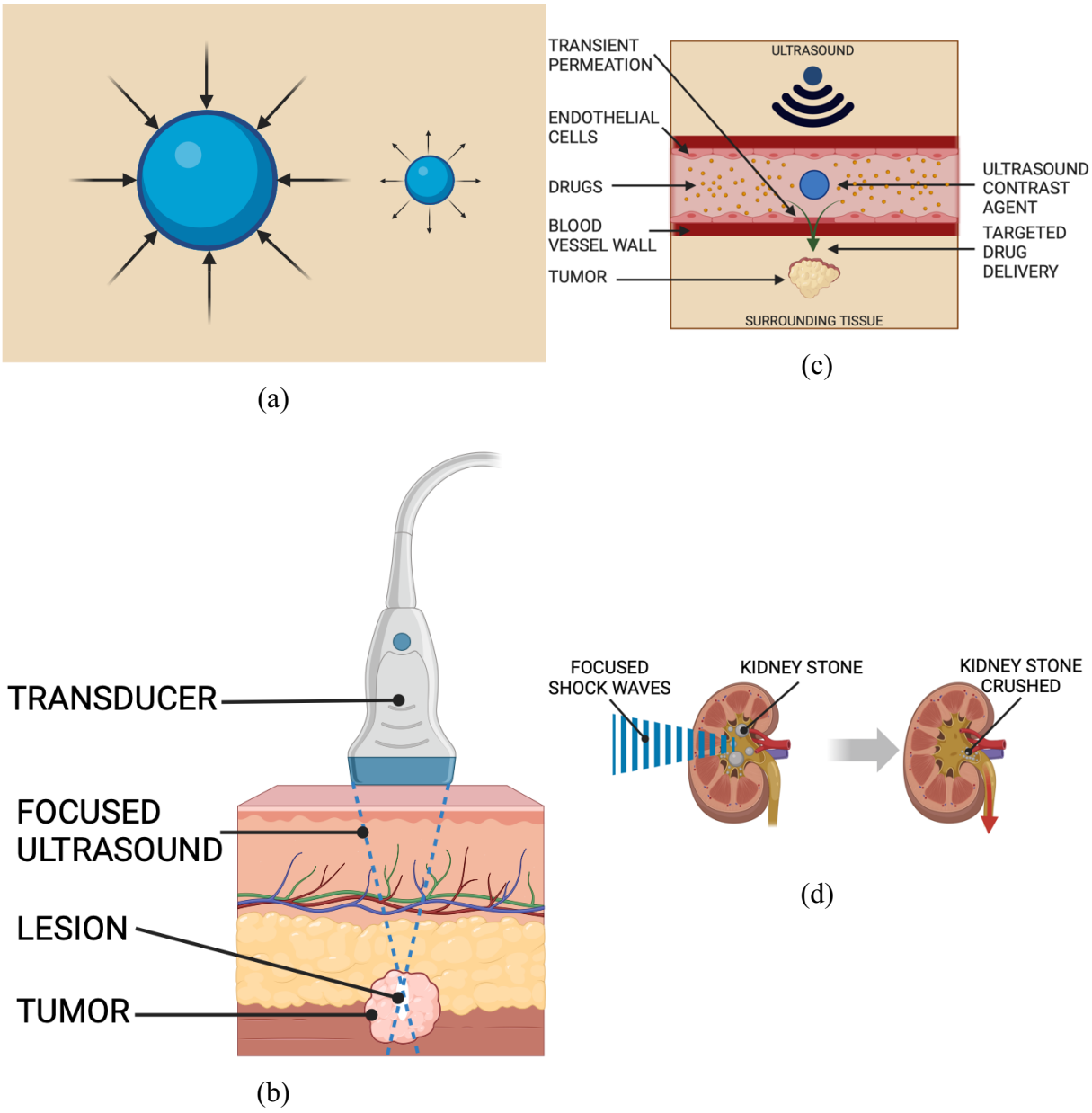

Figure 1-1. Problem Context: Bubble Dynamics in Medical Ultrasound Treatments (a) Bubble Dynamics Under Compression and Expansion. (b) High-Intensity Focused Ultrasound (HIFU) Therapy. (c) Targeted Drug Delivery Using Ultrasound Contrast Agents. (d) Extracorporeal Shock Wave Lithotripsy (ESWL) Process.

Figure 1-1(a) illustrates the compression and expansion phases of an air bubble in a liquid or tissue medium. During these phases, the bubble undergoes significant deformations due to

external forces such as ultrasounds, which can impact the surrounding soft tissue and can lead to damage.

The problem involves several complexities due to the interactions between different phases—gas within the bubble, the surrounding liquid, and the soft biological tissue. Each phase has distinct physical properties, and their interactions can lead to complex phenomena. For example, the bubble can undergo significant deformations due to the ultrasound waves, affecting the liquid and the soft material in various ways. Traditional FSI models often struggle to accurately capture these large deformations and the resulting stresses and strains in the soft material.

Moreover, biological tissues exhibit non-linear and anisotropic mechanical properties, meaning their response to mechanical loading can vary significantly based on factors such as strain rate and direction of loading. Accurately modeling these properties is crucial for predicting tissue behavior under dynamic conditions.

Figure 1-1(b) demonstrates the HIFU therapy process. A transducer emits focused ultrasound waves that target a tumor, creating lesions and ablating the cancerous tissue. Accurate modeling of bubble dynamics and thermal effects is essential to optimize the treatment and avoid damage to surrounding healthy tissues.

Figure 1-1(c) shows the use of ultrasound contrast agents for targeted drug delivery. Ultrasound waves cause microbubbles to permeate endothelial cells, facilitating drug delivery to tumors. This process relies on precise bubble dynamics to ensure effective and safe drug delivery.

Figure 1-1(d) illustrates the ESWL process, where focused shock waves are used to fragment kidney stones. The shock waves cause the stones to break into smaller pieces, which are then passed out of the body. Understanding the bubble dynamics during shock wave exposure is critical to minimizing tissue damage and improving treatment efficacy.

Thermodynamic variations add another layer of complexity. The rapid compression and expansion of the bubble can lead to significant changes in temperature and pressure, especially in the liquid medium. These thermodynamic changes can impact tissue integrity and must be accurately modeled to predict potential thermal damage.

Key challenges in this problem include accurately tracking the interfaces between the bubble, liquid, and soft material, managing the high computational demands of simulating such

systems, and obtaining reliable experimental data for validation. Addressing these challenges is essential for developing robust computational models that can enhance the safety and efficacy of medical treatments involving ultrasound-induced bubble dynamics. By improving our understanding and control of these processes, this research aims to contribute to better patient outcomes and more effective therapeutic techniques.

1.3 State of the Art

1.3.1 Models for FSI

The numerical resolution of those flows is challenging due to their multi-physics character. The most common fluid-structure interaction (FSI) approach is to partition the resolution of the fluid and solid domains. A coupling strategy is then adopted where both solvers are either one-way or two-way coupled through boundary conditions [10]. The Arbitrary Lagrangian-Eulerian (ALE) method combines Lagrangian and Eulerian descriptions for fluid-structure interactions by adjusting the computational mesh in response to structural movements[11]. This flexibility allows it to accommodate both fluid and structural dynamics. However, a significant drawback is its vulnerability to large deformations. Such deformations can lead to mesh tangling and degradation of mesh quality, necessitating frequent remeshing, which can be computationally expensive and complex [12]. The Immersed Boundary (IB) method, on the other hand, employs a unique approach by using separate grids for fluid and solid [13]. The solid structure is conceptually "immersed" into the Eulerian fluid grid, and their interaction is governed by boundary conditions at the interface. This method offers versatility, especially for intricate geometries. However, it can face challenges during large deformations, particularly in accurately representing the fluid-structure interface. A notable issue is the potential smearing of the interface, leading to possible non-physical oscillations near the immersed boundary, which can compromise the solution's accuracy [14]. Conversely, Eulerian methods are suitable for simulating large deformations, decoupling material, and spatial coordinates. Recent advancements in Eulerian elasticity [15], [16], [17], [18], [19], [20] paired with sharp [21] or diffuse interface methods [15] enable FSI applications with multiple materials. Notable

methods with sharp interfaces include the Ghost Fluid Method (GFM) [21], [22], [23] and the cut-cell method [24], [25], [26]. Both methods suffer either from introducing non-conservative terms or complex reconstructions, mixed-cell algorithms challenging to implement, and small-cell instability. Numerous DIMs for multi-fluid flows are reported [27], [28], [29], [30], [31], [32], [33], encompassing bubble dynamics [34], [35], [36], droplet fragmentation [31], complex thermodynamics [37], [38], [39], and cavitation sub-grid models [39], [40], [41], [42], [43], [44]. The multi-fluid model [29] was integrated with Eulerian hyperelasticity, although tracking multiple solids is computationally prohibitive. A single deformation tensor for multiple materials was first proposed in [45] but resulted in significant errors at large density gradients. Alternatively, a single conservation law for the deformation tensor was presented in [17] and later associated with the Allaire DIM [27]. In [34] the inability of the Allaire DIM to accurately capture bubble dynamics due to thermodynamic incompatibility [46] was highlighted. Recently, the current authors proposed a formulation [47] based on the Kapila DIM [33] and the conservation law for the stretch tensor from [17] which is extended here to include complex thermodynamics for any materials [48].

1.3.2 BUBBLE-SOFT MATERIALS NUMERICAL STUDIES

A few numerical studies have been published on the topic of bubble collapse or oscillation near soft materials. In [49] investigated bubble oscillations near a fluid-fluid interface utilizing a Boundary Integral Method (BIM), highlighting that depending on the density ratio, bubbles could either gravitate towards or be repelled from the interface. The authors of [50] expanded the previous work by adding elasticity to the interface, unveiling the emergence of mushroom-shaped bubbles. This phenomenon was experimentally substantiated in [51]. Following in [52] investigated shock-induced bubble jetting in proximity to viscous fluids, concluding that increased tissue viscosity can significantly reduce jet penetration depth. In [53] studied shock bubble interaction near soft and rigid boundaries modeled as fluids during lithotripsy using an improved Ghost Fluid Method (GFM). The impulse from the bubble's collapse was linked to tissue displacement, potentially causing tissue damage or stone fragmentation. In [36] studied the potential injury mechanisms in shockwave lithotripsy in

blood vessels utilizing a multi-fluid DIM, discovering that as bubble confinement increases, so do the pressures and deformations on the vessel wall. In [54] utilized a free Lagrangian method to investigate the impingement of high-speed liquid jets resulting from shock-induced collapsing bubbles. Their findings showed that these jets exerted such significant compression on aluminum that it led to both pitting and plastic deformation. The authors of [55] investigated bubble shapes and maximum jet velocity when subject to an ultrasound forcing near different soft materials using BEM with linear elasticity. In [56] studied the ultrasonic forcing of a UCA bubble above a tissue layer with rigid backing using a BIM. The re-expansion of the toroidal bubble could separate the tissue layer from the rigid backing, a mechanism identified as "peeling". In [57] utilized a two-dimensional Finite Element Method (FEM) to analyze bubble–blood–vessel interactions, showing that vessel constraints can shift a bubble's resonance frequency, causing asymmetric oscillations and inducing potentially damaging shear stress on the vessel wall. The study emphasized the role of the bubble's resonance frequency and ultrasound contrast agent shell elasticity in these dynamics. In [58] utilized a BEM to investigate microbubble dynamics in elastic micro-vessels under ultrasound forcing. Their findings highlighted that when the bubble and vessel's radii are comparable, the ultrasound forcing can cause the bubble to elongate within the vessel, forming counter jets that deform the vessel wall. In [59] investigated the impact of a shockwave on a bubble near various solid materials and the effect of the acoustic impedance on the shockwave emissions and liquid jet strength. They utilized a partitioned approach where the fluid was solved using a compressible multi-fluid solver and the solid using a FEM solver. Lastly, the work of [60] utilized an Eulerian multi-material DIM [61] with AMR to investigate the shock-induced bubble collapse near solid materials during lithotripsy. Their findings highlight the importance of the bubble stand-off distance on the shapes of the bubble and of the tissue. While these studies provide valuable insight into the bubble dynamics: collapse pressure, liquid jet velocities, and shape of the bubble; very little focus if any has been placed on the stresses developed in soft materials.

1.3.3 NUMERICAL STUDIES OF TEMPERATURE FIELDS DURING BUBBLE-SOLID INTERACTION

Few numerical studies have been published investigating temperature fields during bubble collapse near solid walls. The work of [83] is the most relevant to the present investigation; numerical simulations to examine the temperature variations arising from the collapse of a gas bubble near a solid surface, under varying stand-off distances and driving pressures were presented. The study highlighted two distinct mechanisms responsible for peak temperatures along the wall: reflection of the shock produced by bubble collapse for larger stand-off distances, and direct contact of the bubble for shorter distances. A scaling for fluid temperature prediction and an analytical heat transfer model were proposed, suggesting potential melting for soft, temperature-sensitive materials due to repeated bubble collapses. In [84] utilized a hybrid thermal lattice Boltzmann method to delve into nonisothermal laser-produced single cavitation bubble dynamics. Their findings emphasized high pressures and temperatures during the bubble's final collapse due to rapid internal vapor compression and explored the effects of nondimensional distances from a solid boundary on bubble behavior. Nevertheless, no attention was paid to the thermal damage mechanisms and focused on demonstrating the capability of the method. In [85] employed a pressure-based compressible fluid model to explore the thermodynamic effects during bubble collapse near a rigid boundary. Their numerical results were validated with experimental data on bubble shapes and the Keller-Kolodner equation. A substantial heat generation during bubble collapse was identified. Notably, their findings highlight the initial standoff's influence on the peak internal temperature, which increases in the collapse phase and decreases during the rebound. To the best of the author’s knowledge, no numerical study focusing on temperature and complex thermodynamics of ultrasound-induced bubble collapse near a soft material has been reported yet.

1.4 IMPORTANCE OF THERMODYNAMICS

In addition to accurately modeling the bubble-soft material interactions under an ultrasound pulse, accurate modeling of the thermodynamics is also crucial. The rise in temperature during medical applications like HIFU, Histotripsy, and ESWL is a significant concern, primarily because of the risk of thermal injury to surrounding tissues [62]. HIFU aims at elevating the temperature to induce tissue ablation and coagulation [63], although the heating of the intervening tissue is a concern [6]. In ESWL, shock waves disintegrate kidney stones, but the associated heat from the propagation of the repeated pulses and the collapse of cavitation bubbles can pose risks to surrounding tissues [9]. Both cavitation and the conversion of ultrasound absorption to heat contribute to these temperature changes, emphasizing the need to model cavitation-induced heating for the safety and efficacy of these treatments [64]. The vast majority of numerical bubble dynamics studies utilize the stiffened gas (SG) [65], [66], [67], [68], [69], [70] or Tait [71], [72], [73], [74], [75], [76], [77] EoSs. Although these two EoSs are easy to implement, they are unable to describe the liquid thermodynamic behavior appropriately as the first one uses an unphysical specific heat ratio while the latter does not account for density changes due to temperature variations. Therefore, thermal effects were not discussed in these studies. In a previous publication, the current authors compared the ideal gas (IG) to real gas EoSs: Helmholtz [78], Peng-Robinson (PR) [79], and Redlich-Kwong Peng-Robinson (RKPR) [80]. It was shown that the IG EoS largely overpredicts the temperature of the gas during bubble collapse. Similarly, the SG EoS used for liquid thermodynamics is not able to provide temperature predictions due to an unphysical specific heat ratio. Alternatively, the Noble-Able-Stiffened-Gas (NASG) EoS is an improvement of the SG EoS by adding repulsive forces to reduce the density error [81]. Later, in [82], it was shown that the NASG EoS overpredicts the water density at low pressures when using the saturation value as the reference state. The reference states of the variables were modified resulting in new coefficients, referred to as the modified-NASG (MNASG).

1.5 PUBLICATIONS

Peer-Reviewed Journal Publications (newest first):

- A. Shams, S. Bidi and M. Gavaises, "Investigation of temperatures produced during ultrasound-driven collapse of air bubbles near soft materials", awaiting publication.
    - **Armand Shams**: Conceptualization, Data curation, Formal analysis, Investigation, Methodology, Software, Validation, Visualization, Writing – original draft, Writing – review & editing. **Saeed Bidi**: Conceptualization, Methodology, Writing – review & editing. **Manolis Gavaises**: Conceptualization, Funding acquisition, Project administration, Resources, Supervision, Writing – review & editing.
- S. Bidi, A. Shams, P. Koukouvinis and M. Gavaises, "Prediction of shock heating during ultrasound-induced bubble collapse using real-fluid equations of state", *Ultrasounds Sonochemistry*, https://doi.org/10.1016/j.ultsonch.2023.106663.
    - CRediT authorship contribution statement: **Saeed Bidi**: Conceptualization, Data curation, Formal analysis, Investigation, Methodology, Software, Validation, Visualization, Writing – original draft, Writing – review & editing. **Armand Shams**: Conceptualization, Data curation, Formal analysis, Investigation, Methodology, Software, Validation, Visualization, Writing – original draft, Writing – review & editing. **Manolis Gavaises**: Conceptualization, Funding acquisition, Project administration, Resources, Supervision, Writing – review & editing.
- A. Shams, S. Bidi and M. Gavaises, "Investigation of ultrasound-induced collapse of bubbles near soft materials", *Ultrasounds Sonochemistry*, https://doi.org/10.1016/j.ultsonch.2023.106723.
    - CRediT authorship contribution statement: **Armand Shams**: Conceptualization, Data curation, Formal analysis, Investigation, Methodology, Software, Validation, Visualization, Writing – original draft, Writing – review & editing. **Saeed Bidi**: Conceptualization, Methodology, Writing – review & editing. **Manolis Gavaises**: Conceptualization, Funding acquisition, Project administration, Resources, Supervision, Writing – review & editing.

- S. Bidi, P. Koukouvinis, A. Papoutsakis, A. Shams, M. Gavaises "Numerical study of real gas effects during bubble collapse using a disequilibrium multiphase model", *Ultrasounds Sonochemistry,* vol. 90, November 2022, 106175, https://doi.org/10.1016/j.ultsonch.2022.106175.
    - CRediT authorship contribution statement: **Saeed Bidi**: Conceptualization, Methodology, Software, Validation, Formal analysis, Investigation, Data curation, Writing - original draft, Writing - review & editing, Visualization. **Phoevos Koukouvinis**: Conceptualization, Methodology, Software, Validation, Formal analysis, Data curation, Writing - review & editing, Supervision. **Andreas Papoutsakis**: Writing - review & editing, Supervision. **Armand Shams**: Conceptualization, Methodology. **Manolis Gavaises**: Conceptualization, Resources, Writing - review & editing, Supervision, Project administration, Funding acquisition.

Conference Proceedings (newest first):

- A. Shams, S. Bidi and M. Gavaises, "Development of a multi-material diffuse interface model with Eulerian hyperelasticity", IICR-7 2023.
- S. Bidi, A. Shams, P. Koukouvinis and M. Gavaises, "One step towards capturing liquid thermodynamics in bubble collapse using tabulated data" IICR-7 2023.
- A. Shams, A. Papoutsakis and M. Gavaises, "Investigation of the Fluid Structure Interaction of collapsing bubbles in the proximity of or engulfed within biological soft tissue", CAV 2021.

1.6 OBJECTIVES

The cavitation literature focusing on potential mechanisms for material damage due to bubble collapse mostly does not model solid dynamics due the complexity of fluid-structure interaction solvers. Additionally, the traditional FSI approaches fail under large to extreme deformations common to biological flows. Henceforth, the primary aim herein is to develop a

unified model of continuum mechanics for compressible multi-material flows appropriate to biomedical applications.

The main objectives of the present thesis are summarized as follows:

1. To develop and implement a compressible diffuse interface multi-material model with block-structured adaptive mesh refinement capable of simulating biological flows accurately and efficiently.
2. To investigate the mechanical loading of soft materials in ultrasound-induced bubble collapse and the mechanisms contributing to mechanical tissue damage.
3. To examine the importance of using real-fluid EoS for accurate temperature predictions and to expand the proposed multi-material model to complex thermodynamics.
4. To elucidate the temperatures induced during ultrasound-driven bubble collapse near soft-materials and identify the potential thermal damage mechanisms.

1.7 THESIS OUTLINE

The main body of the present thesis is organized, as described below:

Chapter 2 introduces the developed multi-material model, its governing equations, the thermodynamic closure, and the numerical methods used to discretize it. Stringent validation cases for the model are also presented.

Chapter 3 investigates the mechanical loading of soft materials in ultrasound-induced bubble collapse. A parametric study is conducted to demonstrate the effects of the bubble radius, standoff distance and shear moduli on the bubble-soft material dynamics and the stresses developed.

Chapter 4 examines the lack of accuracy of common EoSs in bubble collapse and the necessity to use real-fluid EoSs when predicting temperatures. A lithotripter pulse induced bubble collapse near a rigid wall using real-fluid EoSs is presented along with predictions of temperatures. This is **joint work** where the first and second authors had equal contributions.

CRediT authorship contribution statement: **Saeed Bidi**: Conceptualization, Data curation, Formal analysis, Investigation, Methodology, Software, Validation, Visualization, Writing –

original draft, Writing – review & editing. **Armand Shams**: Conceptualization, Data curation, Formal analysis, Investigation, Methodology, Software, Validation, Visualization, Writing – original draft, Writing – review & editing. **Manolis Gavaises**: Conceptualization, Funding acquisition, Project administration, Resources, Supervision, Writing – review & editing.

Chapter 5 expands the multi-material model to real-fluid EoSs and elucidates the temperatures produced during ultrasound-driven bubble collapse near soft-materials. The potential for thermal damage was assessed by identifying three heating mechanisms. A parametric study on the bubble radius and standoff distance is also performed to understand their impact on heating.

Chapter 6 highlights the major conclusions of the present work and presents recommendations for future studies and applications.

Chapter 7 summarizes the peer-review journal and conference proceedings publications produced from the present work.

2 METHODOLOGY

2.1 GOVERNING EQUATIONS

The non-conservative seven equation of [86] is known to be the most general and complete diffuse interface model able to capture complex wave patterns. Indeed, this full disequilibrium model considers each phase to have its own pressure, velocity and temperature. The time scales of these variables at equilibrium conditions are modeled by source terms. However, since the time scales for equilibration are small, it leads to stiff source terms, making its numerical resolution challenging. To overcome this, in this work, a reduced model is used by applying stiff mechanical relaxation leading to the well-known five-equation model of [33] with a single pressure, velocity, and deviatoric strain in the mixture regions. The multi-component flow model is extended with a kinematic equation for the elastic stretch tensor incorporating Eulerian hyperelasticity. In the limit of 2 materials, the model results in a non-conservative volume faction equation, two mass, one momentum, one energy conservation equations, and in addition, nine non-conservative elastic stretch equations. The resulting model can accurately simulate fluid-structure interactions for any number of material interfaces and can exhibit complex wave patterns where both acoustic and stress waves are captured. In this paper, the focus is placed on ultrasound-driven bubble collapse near soft materials at time scales where inertial forces dominate. Hence, the effect of surface tension, viscosity, mass transfer, and phase transition are neglected, see [87][88][89] for justification. For $l = 1, \dots, N$ materials:

$$\frac{\partial}{\partial t}\begin{pmatrix} \alpha_{(l)} \\ \alpha_{(l)}\rho_{(l)} \\ \rho u_i \\ \rho E \\ \bar{V}_{ij}^e \end{pmatrix} + \frac{\partial}{\partial x_k}\begin{pmatrix} \alpha_{(l)}u_k \\ \alpha_{(l)}\rho_{(l)}u_k \\ \rho u_i u_k - \sigma_{ik} \\ \rho E u_k - u_i\sigma_{ik} \\ \bar{V}_{ij}^e u_k - u_i \bar{V}_{kj}^e \end{pmatrix} = \begin{pmatrix} (\alpha_{(l)} + K_{(l)})\dfrac{\partial u_k}{\partial x_k} \\ 0 \\ 0 \\ 0 \\ \dfrac{2}{3}\overline{V}_{ij}^e \dfrac{\partial u_k}{\partial x_k} - u_i \dfrac{\partial \bar{V}_{kj}^e}{\partial x_k} \end{pmatrix}, \tag{1}$$

where the scalar fields α_i, ρ_i, u_i, E are the volume fraction, the density, the velocity, and the total energy, $\boldsymbol{\sigma}$ the stress tensor, $\overline{\boldsymbol{V}}^e$the symmetric left unimodular stretch tensor. The compression and expansion of each phase in the mixture region are modeled by $K_{(l)}\frac{\partial u_k}{\partial x_k}$ where:

$$K_{(l)} = \alpha_{(l)}\left(\frac{\rho c_p^2}{\rho_{(l)} c_{(l)}^2} - 1\right), \tag{2}$$

with the pressure equilibrium speed of sound [30], a generalization of Wood's speed of sound expressed as:

$$c_p = \left(\rho \sum_{l=1}^{N} \frac{\alpha_{(l)}}{\rho_{(l)} c_{(l)}^2} \right)^{-\frac{1}{2}}. \quad (3)$$

The mixture total energy is:

$$E = e + |\boldsymbol{u}|/2, \quad (4)$$

where e is the mixture specific internal energy and $\boldsymbol{u}$ is the velocity vector. The following mixture rule for the internal energy applies:

$$e = \sum_{l=1}^{N} Y_{(l)} e_{(l)}(\rho_{(l)}, p, \overline{\boldsymbol{B}}), \quad (5)$$

where $e_{(l)}$ are the specific internal energies of each phase, $Y_{(l)}$ are the mass fractions of each phase, $\overline{\boldsymbol{B}} = \overline{\boldsymbol{F}}^{\boldsymbol{T}} \overline{\boldsymbol{F}}$ is the unimodular part of the left Cauchy Green strain tensor and $\overline{\boldsymbol{F}}$ is the unimodular deformation tensor. The mass fractions of each phase are given by:

$$Y_{(l)} = \frac{\alpha_{(l)} \rho_{(l)}}{\rho}, \quad (6)$$

The specific internal energy e for each material is defined by an equation of state (EoS) and a constitutive law where the hydrodynamic and elastic contributions are separated [19] with the following form:

$$e_{(l)}\left(\rho_{(l)}, p, \overline{\boldsymbol{B}}\right) = e_{(l)}^{h}\left(\rho_{(l)}, p\right) + e_{(l)}^{s}\left(\rho_{(l)}, \overline{\boldsymbol{B}}\right), \quad (7)$$

The hydrodynamic part $e_{(l)}^{h}$ depends only on the density and pressure while the elastic part $e_{(l)}^{s}$ depends on the density and strain tensor. A major advantage of this additive decomposition is the decoupling between the two contributions. The pressure is only defined by the hydrodynamic energy and the deviatoric stress tensor is only defined by the elastic energy. The stiffened gas EoS is used for the hydrodynamic energy:

$$p_{(l)} = \left(\gamma_{(l)} - 1\right) \rho_{(l)} e_{(l)} - \gamma_{(l)} p_{\infty,(l)}, \quad (8)$$

where $\gamma_{(l)}$, and $p_{\infty,(l)}$ are parameters of the EoS. The speed of sound of each material is defined as:

$$c_{(l)}^2 = \frac{\gamma_{(l)}(p + p_{\infty,(l)})}{\rho_{(l)}} + \frac{4}{3}\frac{\mu_{(l)}}{\rho_{0(l)}} \quad (9)$$

The elastic energy is subject to the choice of the strain energy density function. The Neo-Hookean model was chosen here as it is a popular non-linear constitutive relationship used in biomedical applications to model tissue:

$$e_{(l)}^s\left(\rho_{(l)}, (\bar{\boldsymbol{B}})\right) = \frac{\mu_i}{2\rho_{0i}}(\bar{I}_1 - 3), \quad (10)$$

where $\bar{I}_1$ is the first invariant of the unimodular left Cauchy Green strain tensor defined as:

$$\bar{I}_1 = tr\big(dev(\bar{\boldsymbol{B}})\big), \quad (11)$$

with $dev(\bar{\boldsymbol{B}}) = \bar{\boldsymbol{B}} - tr(\bar{\boldsymbol{B}})\boldsymbol{I}$ is the matrix deviator and $tr(\bar{\boldsymbol{B}})$ is the trace. The Cauchy stress tensor is derived from the constitutive law:

$$\boldsymbol{\sigma} = \frac{2}{J}\boldsymbol{B}\frac{\partial W}{\partial \boldsymbol{B}}, \quad (12)$$

where $J = \det(\boldsymbol{F})$ is the Jacobian of the deformation tensor. For a Neo-Hookean constitutive law, the Cauchy stress tensor can be expressed as follows:

$$\boldsymbol{\sigma} = -p\boldsymbol{I} + \frac{\rho\mu}{\rho_0} dev(\bar{\boldsymbol{B}}), \quad (13)$$

where p is the mixture pressure, ρ is the mixture density, ρ_0 is the initial mixture density of the materials and μ is the mixture shear modulus. The above formulation of the stress tensor allows modeling of both solids and fluids. For the latter, the shear modulus is zero, thus resulting in a spherical stress tensor and no elastic energy contribution. The mixture density is defined according to the mixture rule:

$$\rho = \sum_{l=1}^{N} \alpha_{(l)}\rho_{(l)}. \quad (14)$$

The saturation constraint equation is required to evaluate the volume fraction of the phases:

$$\sum_{l=1}^{N} \alpha_{(l)} = 1. \quad (15)$$

2.2 THERMODYNAMIC CLOSURE

The thermodynamic assumptions that affect the materials involved in bubble dynamic cases can play a detrimental role in the temperature distributions and even the dynamics of bubble collapse, although to a much lesser extent. The EoS can play a detrimental role in capturing the aforementioned variations of density during bubble collapse and can shed light on dissipation mechanisms. Further, the formulation of the EoS has a more intrinsic role, as it can affect the predictions of compression heating of the liquid, and thus, consequently influencing the temperature distribution and the heat transfer (from gas to liquid, or from the liquid to nearby solid/soft walls). In fact, in the former work of the authors [90], the relevant EoS has been demonstrated to greatly affect compression heating of the bubble contents during strong bubble collapses with the initial pressure ratio (defined as the ratio of external pressure to internal pressure $t = 0$ s) of 353, leading to differences of 4,000K (or nearly 70%), between the commonly used IG EoS and real-fluid models. Similar effects, even though to a lesser extent can manifest in the liquid, as it will be further demonstrated here. Demonstrating an excellent accuracy and wide range of applicability in our previous work [90], the RKPR EoS is employed in this study for the gas phase in tabulated format with bilinear interpolation as a time-efficient numerical implementation compared to on-the-fly utilization of the parametric form [91].

2.2.1 TAIT EOS

This is a polytropic-type EoS [92], [93] which originally relates liquid pressure to density. The original form of Tait EoS reads as:

$$p = \frac{\rho_0 c_0^2}{n} + \left(\left(\frac{\rho}{\rho_0}\right)^n - 1\right) + p_0 \qquad (16)$$

where $p, \rho,$ and c are pressure, density, and speed of sound, respectively. Subscript 0 denotes the reference state. Moreover, exponent n is set to 7.15 for weakly compressible liquids such as water [94]. Whereas being rather simple and accurate in predicting liquid densities, it fails to describe density variations due to temperature and therefore, compression heating. This is

indeed the case for all EoS that links density to pressure only, i.e., having the form $p = f(\rho)$. This observation stems from the fact that, in general, entropy can be written as [95]:

$$ds = \frac{c_p}{T} dT + \frac{1}{\rho^2}\left(\frac{\partial \rho}{\partial T}\right)_p dp \qquad (17)$$

The implication of this equation is that for any EoS written in the form of $p = f(\rho)$, the partial derivative $\left(\frac{\partial \rho}{\partial T}\right)_p$ is zero, hence entropy changes are a function of temperature only. It becomes thus apparent that in such cases, no matter how much a liquid will be compressed in a reversible and adiabatic manner (i.e., isentropic) it will not heat up, and thus the relevant dissipation effects are ignored. The Tait equation of state has been used in improved extensions of the Rayleigh-Plesset equation, such as Keller-Miksis [96] or Gilmore models [97], or resolved 2D/3D bubble dynamic cases [98], [99], [100]. Alternative forms that incorporate temperature-related effects have been proposed in the past discussed in [101], see for example Koop [102] or Saurel [103]; however, in both cases the authors have used a simplified representation for internal energy without considering density variation effects.

Even though common liquids are characterized by weak compressibility, the immense conditions taking place during bubble collapse can produce significant compressions in the order of many GPa. Furthermore, since in reality the liquid density is affected by temperature also, the aforementioned compression will produce heating of the liquid. On the other hand, the simple liquid EoSs that consider density variations of density due to temperature can greatly overestimate this heating. A particular example of such a model, commonly used in bubble dynamics [104], [105], is the SG EoS (for which is the interested reader can refer to the work of Flatten et al. [106] for fundamental thermodynamic relations). To illustrate the deviations that such simplified models can produce, the performance of the simplified and advanced EoSs are compared with the most accurate database IAPWS [107] as a reference formulated in NIST Refprop [108] in the next section.

2.2.2 MODIFIED TAIT EOS

Expressing (16) for density, an alternative proposed hereafter has the following form:

$$\rho = \left(\frac{p}{\rho_0 c_0^2 f_1(T)} + 1\right)^{1/n} \rho_0 f_2(T) \quad (18)$$

where $f_1(T)$ and $f_2(T)$ are functions that need to be determined. Any candidate formula, as the above, can be fitted to IAPWS datasets using NIST Refprop [108]. Two main parameters are required:

1. The speed of sound should vary with respect to temperature and, at high pressures, decrease with increase of temperature. Here a function in the form of $f_1(T) = \sqrt{\left(\frac{a}{T}\right)}$ was chosen.
2. The isobaric density variation with respect to temperature should have an inflexion point, due to the presence of the critical point. Naturally, this can be expressed by using a sigmoid function, such as *tanh*. Hence, a suitable candidate can have the form:

$$\rho(p,T) = \left(\frac{p}{\rho_0 c_0^2 \sqrt{aT_1/T}} + 1\right)^{1/n} \rho_0 \left[1 - b.\tanh\left(\frac{T - T_1}{T_2}\right)\right] \quad (19)$$

The selected functions $f_1(T)$ and $f_2(T)$ are produced via data fitting taking numerical stability into account. The incentive behind the general monotonicity is provided in each point, i.e.: (a) speed of sound decreases with respect to temperature and (b) existence of inflection points in density near the critical point. The aforementioned density function defines also the specific volume, $\upsilon = \frac{1}{\rho}$. Calibration of this formulation is done using IAPWS database, for a range of $280 - 2000$ K and $1000 - 10^9$ Pa. After calibration, the following values for the coefficients are obtained: $T_1 = 650$ K, $T_2 = 550$ K, $a = 0.277096868$, $b = 0.659026$, $\rho_0 = 708.9997$ $\frac{kg}{m^3}$ and $n = 2$. In the image below, red points correspond to IAPWS database, whereas the surface is the plot of the fitted $\rho(p,T)$ function.

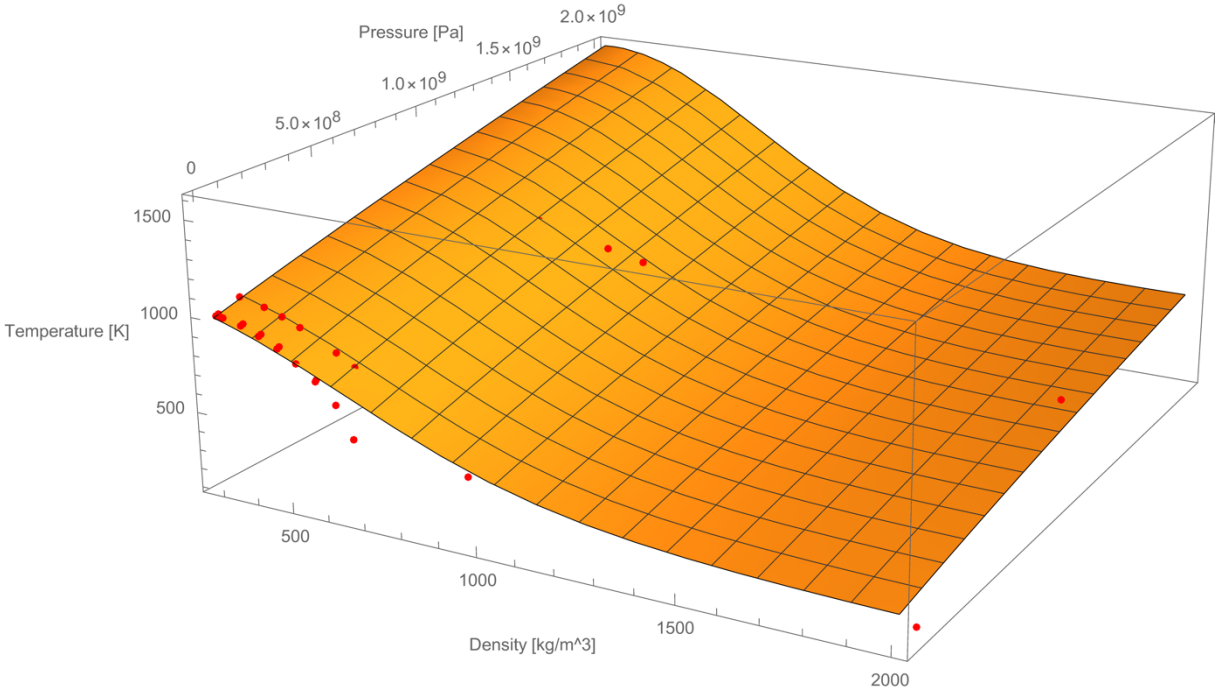

Figure 2-1. IAPWS data on the surface plot of $\rho(p,T)$ where the red dots correspond to the IAPWS database.

Apart from density relation to pressure and temperature, thermodynamic relations for the enthalpy, entropy, speed of sound need to be defined. For heat capacity at constant pressure there are constraints to be satisfied for the EoS to be consistent. From the definition of enthalpy $dh = c_p dT + \left(v - T\frac{dv}{dT}\right)dp$, it must be an exact differential. Hence, c_p and specific volume are linked, as follows:

$$\frac{dc_p}{dp} = \frac{d}{dT}\left(v - T\frac{dv}{dT}\right) \Rightarrow c_p = \int_{p_{ref}}^{p} \frac{d}{dT}\left(v - T\frac{dv}{dT}\right)dp + C_1(T) + C_2. \quad (20)$$

The integral above comes directly from the choice of EoS; the only degree of freedom for adjusting c_p to a reasonable value comes from the functions $C_1(T)$ and C_2. C_1 and C_2 are fitted using experimental data to adjust the theoretical expression for c_p so that it matches observed values. After fitting, C_2 = 10334 $\frac{J}{kg.K}$ and $C_1 = -4.889(T - 300)$. Also, the enthalpy function can then be obtained by integrating:

$$dh = c_p dT + \left(v - T\frac{dv}{dT}\right)dp. \quad (21)$$

Similarly, entropy can be obtained by integrating:

$$ds = \frac{c_p}{T}dT + \frac{1}{\rho^2}\frac{d\rho}{dT}dp. \quad (22)$$

Further, various derivatives of density and enthalpy can be defined, once the respective formulation is obtained, as $\frac{dh}{dT}$, $\frac{dh}{dp}$, $\frac{d\rho}{dT}$, and $\frac{d\rho}{dp}$, which can be further used to define speed of sound:

$$c = \sqrt{\frac{\rho\frac{dh}{dT}}{\rho\frac{d\rho}{dp}\frac{dh}{dT} + \frac{d\rho}{dT}\left(1 - \rho\frac{dh}{dp}\right)}}, \quad (23)$$

and heat capacity at constant volume, c_v, as:

$$c_v = c_p - \frac{\left(\frac{1}{v}\frac{dv}{dT}\right)^2}{\left(\frac{1}{\rho}\frac{d\rho}{dp}\right)\rho}. \quad (24)$$

2.2.3 NOBLE ABEL STIFFENED GAS (NASG) AND MNASG EOSS

The SG EoS involves molecular attractive and agitative forces. The aim of the Noble Abel Stiffened Gas (NASG) is to add repulsive forces to the SG EoS to reduce the density error as shown in [81]:

$$p = (\gamma - 1)\frac{(e - q)}{(v - b)} - \gamma p_\infty, \quad (25)$$

where q, p_∞, and b are the fluid heat bond, a characteristic constant, and co-volume as the volume of the molecules pack, respectively, all depending on the medium. More specifically, the molecular agitation is included in the term $(\gamma - 1)(e - q)$ while the repulsive forces are represented by $(v - b)$. The term γp_∞ represents the attractive effects leading to matter cohesion in liquid and solid states. It is noted that setting $q = b = 0$ recovers the original SG EoS. The temperature-based representation of the NASG EoS is derived from the Maxwell rules [81]:

$$T = \frac{(v-b)(p+p_\infty)}{(\gamma-1)c_v}, \quad (26)$$

in which c_v is heat capacity at constant volume. Also, the speed of sound in NASG is obtained from:

$$c^2 = \frac{\gamma v^2 (p+p_\infty)}{(v-b)}. \quad (27)$$

The NASG coefficients for liquid water are presented in Table 1. These coefficients have been found to match well experimental data inside the temperature range [300-500 K] [81].

Table 1. NASG coefficients for liquid water

$c_v\left(\frac{J}{kgK}\right)$	γ	$p_\infty(Pa)$	$b\left(\frac{m^3}{kg}\right)$	$q\left(\frac{J}{kg}\right)$
3610	1.19	7028×10^5	6.61×10^{-4}	-1177788

In [82], it was shown that the NASG EoS overpredicts the water density at low pressures when using the saturation value as the reference state. Therefore, the reference states of the variables were modified to generate new values for p_∞ and b as indicated in Table 2. The resulted thermodynamic closure is the MNASG EoS [82].

Table 2. MNASG coefficients for liquid water

$c_v\left(\frac{J}{kgK}\right)$	γ	$p_\infty(Pa)$	$b\left(\frac{m^3}{kg}\right)$	$q\left(\frac{J}{kg}\right)$
3610	1.19	6217.8×10^5	6.7212×10^{-4}	-1177788

It is noted that a set of $\gamma = 4$, $p_\infty = 6 \times 10^8$, and $b = q = 0$ converts the above formula to the common SG EoS for water.

2.2.4 COMPARISON OF THE LIQUID MODELS

To demonstrate the applicability of the modified Tait EoS both in terms of temperature and density prediction, isentropic compression of liquid water is examined in Figure 2-2. The

compression starts from 1 bar and 288.15 K. After compression at a given pressure ratio, the water density and temperature increase. As shown below, in the range of calibration the accuracy is rather decent, below 10%, both in terms of temperature and density prediction. In Figure 2-3, a similar test is demonstrated with the SG EoS with the same initialization. As shown, the SG EoS tends to dramatically over-predict the resulting compression heating at high pressures. At a pressure ratio of 10^5, i.e., when liquid is compressed to 10 GPa, the SG EoS predicts a temperature increase of roughly 1282 K. Contrary to this prediction, the IAPWS data predicts a temperature rise of roughly 169 K, almost an order of magnitude lower that the SG prediction. Similarly, a significant error in density prediction of ≈ 50% with the SG EoS is observed at this compression ratio.

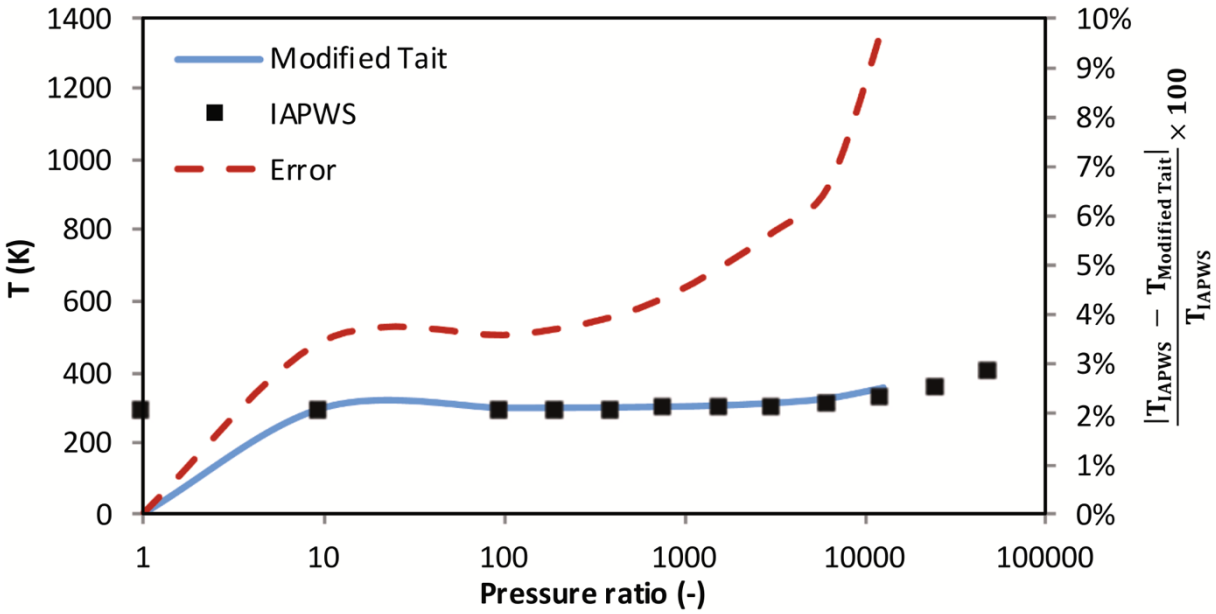

(a)

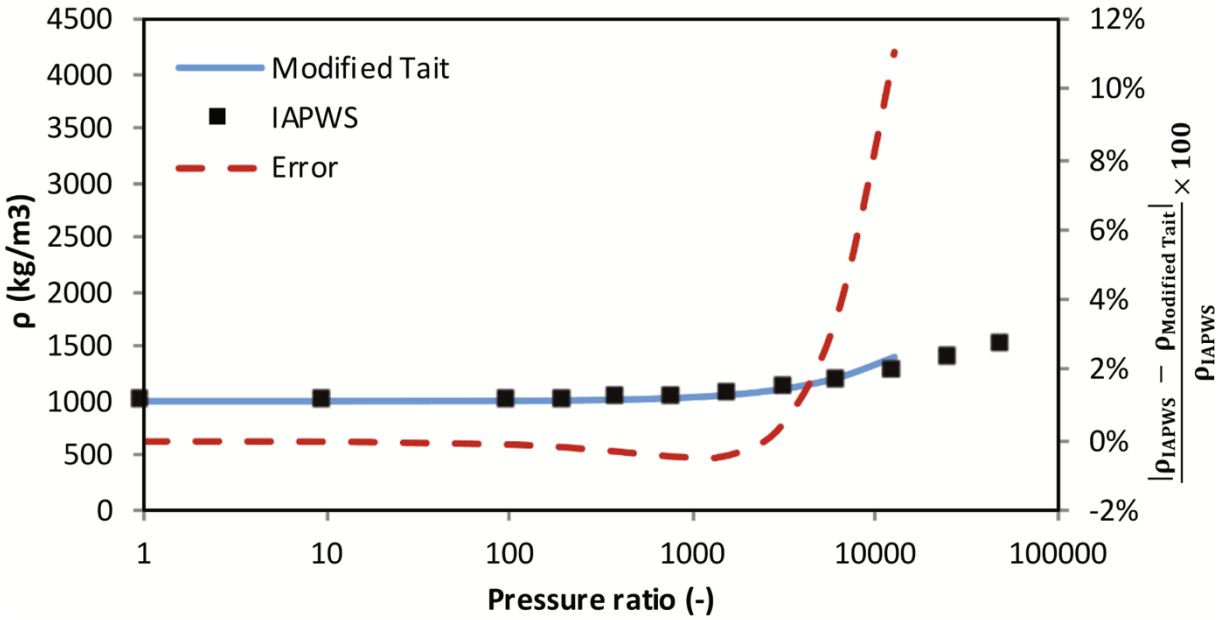

(b)

Figure 2-2. Comparison of temperature (a) and density (b) obtained with the modified Tait EoS and the IAPWS data at different compression ratios. Squares represent the IAPWS reference, the blue line results of the Modified Tait EoS and the red line is the error in percentage corresponding to the right axis.

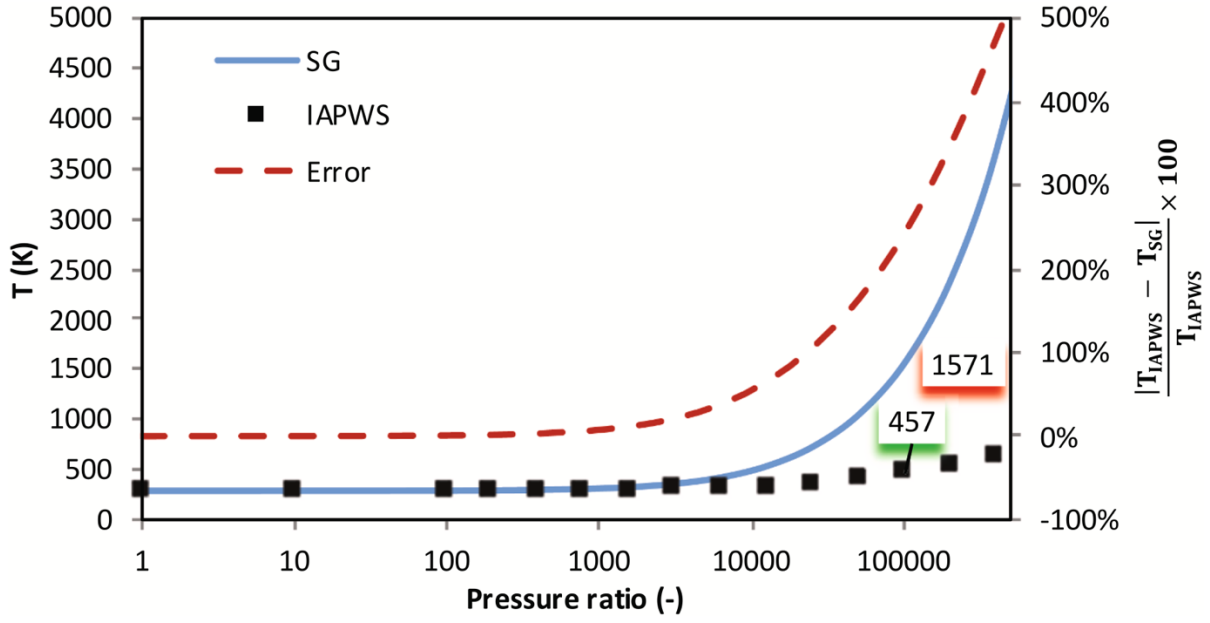

(a)

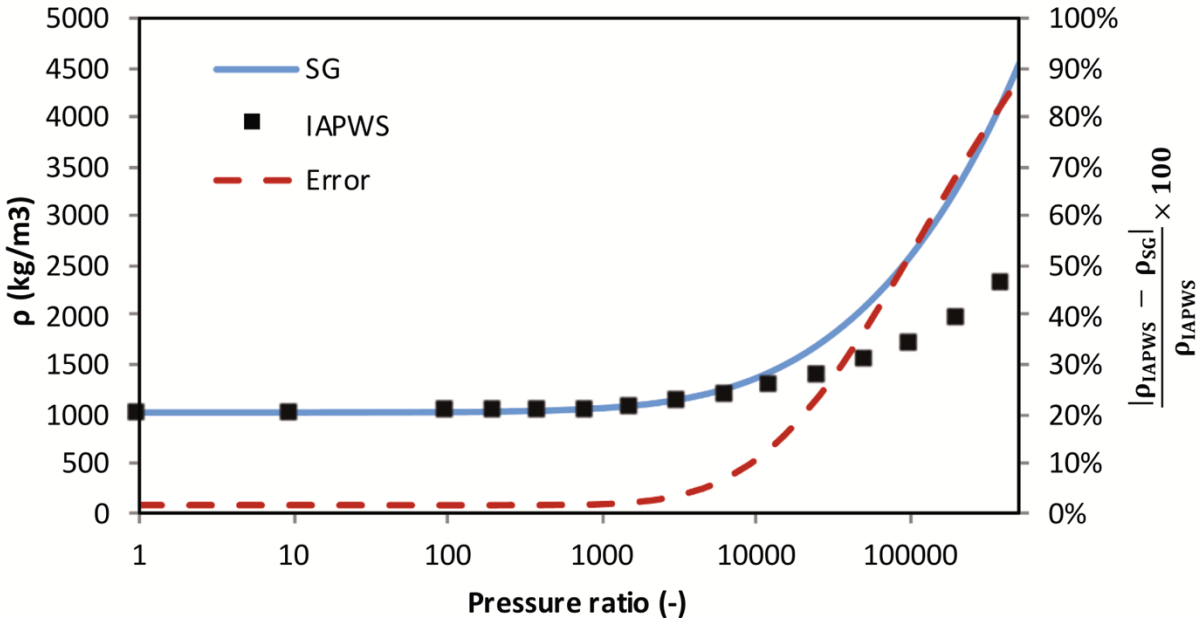

(b)

Figure 2-3. Comparison of temperature (a) and density (b) obtained with the SG EoS commonly used in bubble dynamic studies and the IAPWS data at different compression ratios. Squares represent the IAPWS reference, the blue line results of the SG EoS and the red line is the error in percentage corresponding to the right axis.

It becomes apparent that the above can play an important role in studies involving heat transfer of collapsing bubbles; over/under-prediction of liquid temperature due to the adopted EoS can affect the heat fluxes to/from the bubble. Even more, the overestimation of compression heating can be observed even at passing shock waves, emitted during bubble collapses as will be shown in the results section.

Advanced models such as IAPWS come with a larger complexity, which makes them rather cumbersome to implement. Whereas tabulation methods can be applied (see [90], [109]) to speed up calculations, their inherent ability to capture phase transitions can cause problems with the numerical solution of the flow equations. Hence, it is of interest to devise robust and versatile thermodynamic closures for liquids, that can be used for bubble collapse investigations.

2.3 NUMERICAL METHODS

The system of basic equations described above is hyperbolic and can be cast into semi-conservative form to be solved by a Godunov-type scheme [110]:

$$\frac{\partial \boldsymbol{q}}{\partial t} + \frac{\partial \boldsymbol{F}^k}{\partial x_k} = \boldsymbol{s}_{non-cons} + \boldsymbol{s}_g, \tag{28}$$

where $\boldsymbol{q}$ is the vector of state variables, $\boldsymbol{F}^k$ are the vectors of fluxes in the respective directions x, y, z, $\boldsymbol{s}_{non-cons}$ is the vector of non-conservative source terms, and $\boldsymbol{s}_g$ is the vector of geometrical source terms. The vector of state variables, vectors of fluxes, and non-conservative source terms are expressed as:

$$\boldsymbol{q} = \begin{pmatrix} \alpha_{(l)} \\ \alpha_{(l)}\rho_{(l)} \\ \rho u_i \\ \rho E \\ \bar{V}^e_{ij} \end{pmatrix}, \boldsymbol{F}^k = \begin{pmatrix} \alpha_{(l)}u_k \\ \alpha_{(l)}\rho_{(l)}u_k \\ \rho u_i u_k - \sigma_{ik} \\ \rho E u_k - u_i\sigma_{ik} \\ \bar{V}^e_{ij}u_k - u_i\bar{V}^e_{kj} \end{pmatrix}, \boldsymbol{s}_{non-cons} = \begin{pmatrix} (\alpha_{(l)} + K_{(l)})\dfrac{\partial u_k}{\partial x_k} \\ 0 \\ 0 \\ 0 \\ \dfrac{2}{3}\bar{V}^e_{ij}\dfrac{\partial u_k}{\partial x_k} - u_i\dfrac{\partial \bar{V}^e_{kj}}{\partial x_k} \end{pmatrix}. \tag{29}$$

The geometrical source term is defined as:

$$\boldsymbol{s}_g = -\frac{\beta}{r}\begin{pmatrix} 0 \\ \alpha_{(l)}\rho_{(l)}u_r \\ \rho u_r^2 - \sigma_{rr} + \sigma_{\theta\theta} \\ \rho u_r u_z - \sigma_{rz} \\ \rho E u - (u_r\sigma_{rr} + u_z\sigma_{rz}) \\ \frac{1}{3}\bar{V}^e_{ij}u_r - \delta_{i\theta}\bar{V}^e_{ij}u_r \end{pmatrix}, \tag{30}$$

where $\beta = 1$ when the coordinate system is cylindrical and $\beta = 2$ when the coordinate system is spherical. After spatially integrating the conservation law (28) by taking the volume integral and applying the divergence theorem we obtain the finite volume discretization:

$$\begin{aligned} \frac{d\boldsymbol{q}_{i,j,k}}{dt} = {} & \frac{1}{\Delta x_i}\left[\boldsymbol{F}^x_{i-1/2} - \boldsymbol{F}^x_{i+1/2}\right] + \frac{1}{\Delta y_j}\left[\boldsymbol{F}^y_{j-1/2} - \boldsymbol{F}^y_{j+1/2}\right] \\ & + \frac{1}{\Delta z_k}\left[\boldsymbol{F}^z_{k-1/2} - \boldsymbol{F}^z_{k+1/2}\right] + \boldsymbol{s}_{i,j,k}. \end{aligned} \tag{31}$$

The cell-averaged vector of state variables and the face-averaged vectors of fluxes are defined as:

$$\boldsymbol{q}_{i,j,k} = \frac{1}{V_{i,j,k}} \iiint_{I_{i,j,k}} \boldsymbol{q}(x,y,z,t)dxdydz, \quad (32)$$

$$\boldsymbol{F}_{i+1/2,j,k} = \frac{1}{\Delta y_j \Delta z_k} \iint_{A_{i+1/2,j,k}} \boldsymbol{F}(x,y,z,t)dydz. \quad (33)$$

The fluxes at the cell faces are computed using an approximate Riemann solver. The Harten, Lax, and van Leer (HLL) Riemann solver and its derivatives, are solutions for wave propagation problems. The HLL method uses a wave configuration that separates three constant states and assumes that wave speeds can be estimated from these initial states. The HLL-contact (HLLC) scheme expands on this by handling four states separated by a contact discontinuity. However, this does not accurately represent the conditions in solids where additional families of characteristics related to shear wave speeds exist. The HLLD approach used here [111][18] accounts for this by introducing the concept of multiple slower waves between the fastest waves and the contact discontinuity. The piece-wise linear MUSCL reconstruction was used on the primitive variables to reconstruct the states at the faces to avoid spurious oscillations at the material interfaces [112][35].

2.3.1 Temporal Integration

After the spatial derivatives are approximated, a semi-discrete system composed of ordinary differential equations in time is obtained where a two-step time integration was applied [113] resulting in a second-order temporal integration:

$$\boldsymbol{q}_{i,j,k}^{n+\frac{1}{2}} = \boldsymbol{q}_{i,j,k}^{n} + \frac{1}{2}\Delta t \boldsymbol{\mathcal{L}}\left(\boldsymbol{q}_{i,j,k}^{n}\right), \quad (34)$$

$$\boldsymbol{q}_{i,j,k}^{n+1} = \boldsymbol{q}_{i,j,k}^{n} + \Delta t \boldsymbol{\mathcal{L}}\left(\boldsymbol{q}_{i,j,k}^{n+\frac{1}{2}}\right), \quad (35)$$

where $\boldsymbol{\mathcal{L}}$ is the right-hand side of (31), and n is the timestep index. The timestep size Δt is determined using the acoustic-based Courant–Friedrichs–Lewy (CFL) number.

2.3.2 ADAPTIVE MESH REFINEMENT

The numerical methods used in this work have been developed and implemented within the AMReX framework [114][115]. This is a C++-based framework that allows for solving partial differential equations using block-structured adaptive mesh refinement algorithms. In [116] structured adaptive mesh refinement (AMR) method was used to solve the hyperbolic system detailed below utilizing adaptive refinement in space and time. The computational mesh is broken down into logically rectangular sub-grids where cells have the same resolution. The sub-grids, also called patches, are organized into a hierarchy of embedded levels. The lowest resolution grids at level 0 spans across the entire computational domain. A refinement criterion is utilized for generating finer levels from the coarser ones at a user-defined interval of timesteps. Cells at level l are r_l-times finer than at level $l-1$ with $\Delta \boldsymbol{x}_l = \Delta \boldsymbol{x}_{l-1}/r_l$ and $\Delta t_l = \Delta t_{l-1}/r_l$ where $r_l \in \mathbb{N}, r_l \geq 2$ for $l > 0$ and $r_0 = 1$. A subcycling-in-time approach was utilized where the coarse grid solution is advanced in time ignoring the finer levels. Then the finer levels are advanced recursively while using the coarser levels as boundary conditions. At the coarse-fine interfaces, the ghost cells are determined using conservative linear interpolation in space and time. The solution on the coarse grids needs to be corrected by the finer levels to ensure global conservation. Therefore, once a fine level has reached the same physical time as the coarser level a synchronization step is applied. The volume averages of the coarse cells are corrected to be equal to the volume averages of the finer cells. Additionally, the area and time-weighted fluxes at the coarse-fine interfaces are also corrected by the sum of the fine fluxes.

2.4 VALIDATION AND VERIFICATION

In this section, verification studies against well-known benchmark cases are presented. To showcase the numerical model's ability to capture bubble dynamics, we simulate the collapse of a spherical gas bubble in an infinite water medium at different pressure ratios. Additionally,

to evaluate the accuracy of the model to predict fluid-solid interactions and wave transmission across material interfaces, a semi-analytical wave propagation case is conducted.

2.4.1 SPHERICAL BUBBLE COLLAPSE

A common benchmark case for multi-phase flow solvers is the comparison against the Keller-Miksis equation [34] [117][118]. The effects of surface tension and viscosity are ignored. Two cases are presented, corresponding to a low $p_f/p_b = 20$ and a high initial pressure ratio $p_f/p_b = 353$; for the former a grid convergence study was also performed. In both cases the initial bubble radius $R_0 = 1$ mm where the domain size $L = 50R_0$. Spherical coordinates with $\beta = 2$ and a base mesh of 512 cells in the radial direction have been employed. A grid convergence study was conducted, and it was found that 2 levels of refinement is sufficient to match the Keller-Miksis solution. At the center of the bubble, a symmetry boundary condition was used. At the far-field, an outflow boundary condition was imposed. The pressure is initialized uniformly inside the bubble and gradually increases in the water medium according to [34]:

$$p(R) = p_f + \frac{R_0}{r}(p_b - p_f), \tag{36}$$

where $p_f$is the far-field pressure, r is the radial coordinate and p_b is the bubble pressure. The initial water density is $\rho_{water} = 998.2$ kg $\cdot$ m^{-3} and the stiffened gas parameters are $\gamma_{water} = 4.4$ and $p_{\infty,water} = 6 \cdot 10^8$ Pa. The initial air density is $\rho_{air} = 1.225$ kg. m^{-3} and the stiffened gas parameters are $\gamma_{water} = 1.4$ and $p_{\infty,air} = 0$ Pa which results in considering an ideal gas. For the first case, an initial low-pressure ratio of $p_f/p_b = 20$ is considered. The bubble radius is normalized by its initial radius R_0 and time is normalized by the Rayleigh collapse time [118] expressed as:

$$t_c = 0.915R_0\sqrt{\frac{\rho_{water}}{p_f}}. \tag{37}$$

The Keller Miksis solution was solved using Julia [119] and the DifferentialEquations.jl [120] package with Rosenbrock temporal integration. In Figure 2-4, the bubble radius evaluation is depicted for both cases; excellent agreement was found. The low-pressure case

was run with the base grid, one level, and two levels of refinement. The latter was found to fit the solution and hence chosen for the high-pressure case. The rebound and minimum radius observed in the high-pressure ratio case are smaller due to the compressibility effects. In fact, the present results show the capability of the method to capture compression and expansion rates accurately.

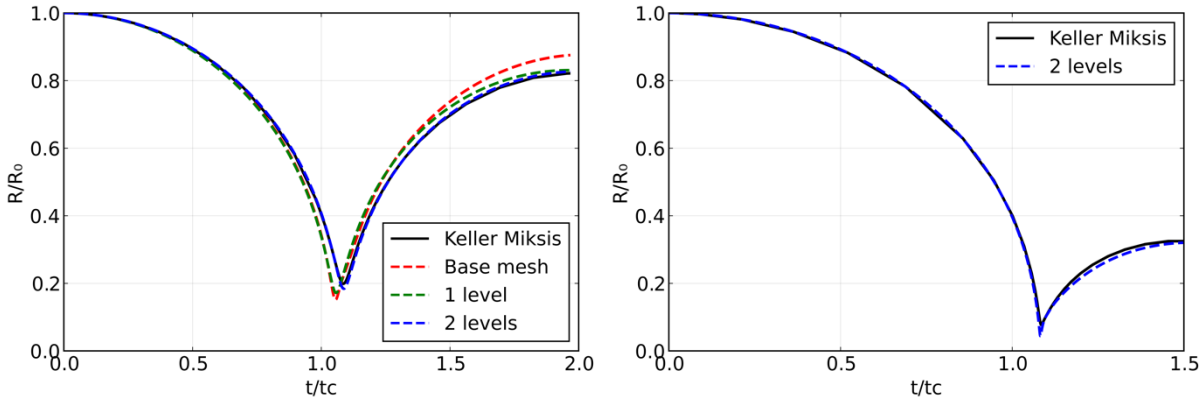

Figure 2-4. Temporal evolution of the normalized bubble radius over normalized time for both spherical bubble collapse cases. (a) Low pressure ratio $p_f/p_b = 20$ with 3 different AMR grids. (b) High-pressure ratio case $p_f/p_b = 353$ with 2 levels of refinement.

2.4.2 SEMI-ANALYTICAL WAVE TRANSMISSION ACROSS A FLUID/SOLID INTERFACE

A semi-analytical wave propagation case is presented as shown in Figure 2-5a. A 3D domain is utilized where the upper half is the fluid material, and the lower half is solid. In the fluid medium, a spherical pressure wave is generated from a monopole source, similar to a spherical shock emitted by a collapsing bubble. The monopole source is standing at a distance H from the planar fluid/solid interface. To validate the results between the semi-analytical solution and the numerical results, two sensors R_1, and R_2 were placed in the fluid and solid medium, respectively. The sensors were placed symmetrically at a distance $L_1 = 2.5$ mm from the axis of symmetry and at a distance $L_2 = 1.45$ mm above and below the planar interface.

The dynamic pressure was recorded at the sensor inside the fluid medium. Additionally, the horizontal and vertical velocities were recorded inside the solid medium.

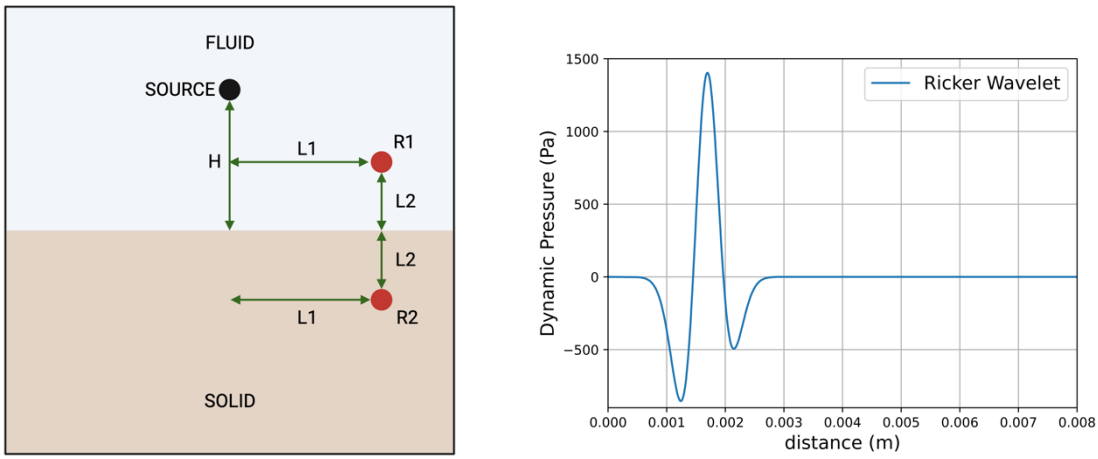

(a) (b)

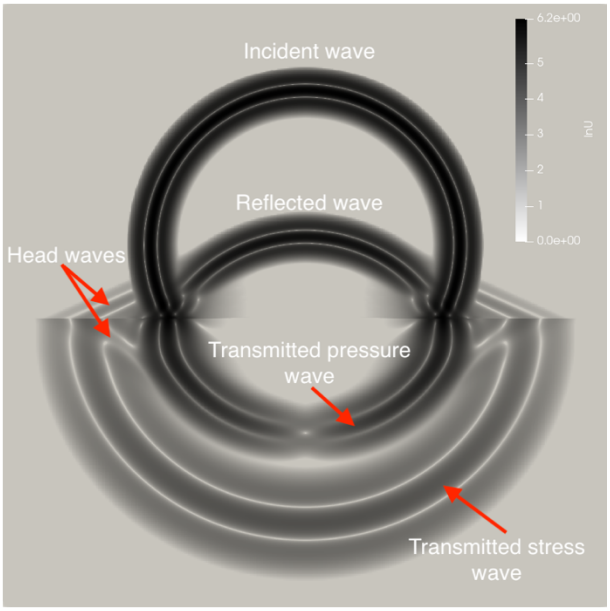

(c)

Figure 2-5. (a) Wave transmission across fluid/solid interface schematic. (b) Pressure profile of the Ricker wavelet generated from the monopole source. (c) Velocity magnitude at t=3us. The incident and reflected waves in the fluid, the transmitted stress and pressure waves as well as head waves in both materials are clearly captured.

The Ricker wavelet was chosen for the spherical pressure wave because its well-defined analytical solution makes it ideal for assessing the solver's accuracy and ability to capture wave

dynamics. The wavelet was prescribed as an initial condition in the fluid medium where the pressure at a distance r from the source is expressed as:

$$p(r) = p_0 + \frac{Q(-r/c_0)}{r}, \quad (38)$$

$$Q(s) = (1 - 2\pi^2 f_0^2 (s + s_1)^2)\mathrm{e}^{-\pi^2 f_0^2 (s+s_1)^2}, \quad (39)$$

with p_0 the hydrostatic pressure, c_0 the speed of sound of the fluid medium, f_0 is the frequency of the wavelet and s_1 is a constant that controls the initial position of the wavelet. The parameters used are given in Table 2-3.

Table 2-3. Thermodynamic and wavelet parameters of the semi-analytical wave transmission problem.

Ricker wavelet		**Fluid**		**Solid**	
$\boldsymbol{f_0}$(MHz)	1.43	ρ_f(kg/m^3)	1000	ρ_s(kg/m^3)	1995
$\boldsymbol{s_1}$**(μs)**	0.85	γ_f	6.59	γ_s	3.4
$\boldsymbol{H}$(mm)	2.9	$p_{\infty,f}$(MPa)	410	$p_{\infty,s}$(Pa)	4591545000
$\boldsymbol{p_0}$(MPa)	0.101	μ_f(Pa)	0	μ_s(Pa)	10728633195

In the presented problem, the maximum dynamic pressure within the fluid is two orders of magnitude less than the hydrostatic pressure. Thus, we can interpret the impacting wave as a small disturbance, and therefore this can be modeled as an acoustic wave propagating through a homogenous fluid medium. Under the assumption of linear elasticity and isotropy of the solid material, the overall problem can be solved analytically by coupling the linear acoustic wave equation with the equation of motion for a linear elastic solid. Such an analytical solution can be obtained with the Cagniard-de Hoop method [121]. A semi-analytical solution was computed using the open-source software, Gar6more3D [122].

The simulation was carried out in axisymmetric coordinates with $\beta = 1$ to save computational time. The computational domains span 8 mm in the axial direction and 16 mm in the vertical direction. A symmetry boundary condition was imposed at the center axis and outflow boundary conditions at all the other boundaries. The base mesh consists of 256 cells in

the axial direction and 512 cells in the vertical direction. The adaptive mesh refinement was allowed to refine up to 2 levels according to the magnitude of the density gradient. A CFL number of 0.4 was used to compute the timestep. The thermodynamic parameters for the simulation can be found in Table 2-3. The velocity magnitude is shown in Figure 2-5a where the incident and reflected waves in the fluid, the transmitted stress and pressure waves as well as head waves in both materials are clearly captured. The numerical results are compared to the semi-analytical solution of Gar6more3D [122] in Figure 2-6 where an excellent agreement is found.

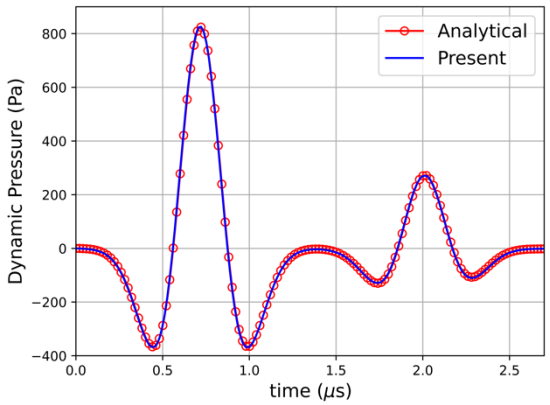

(a)

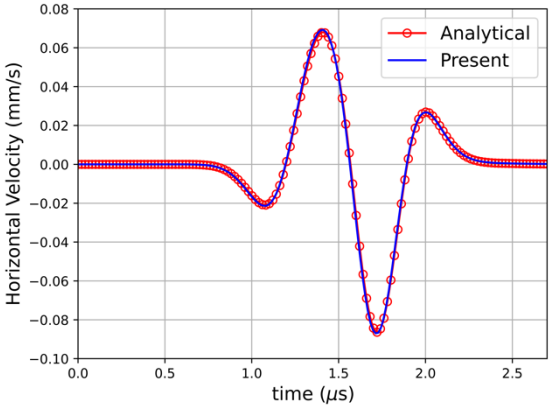

(b)

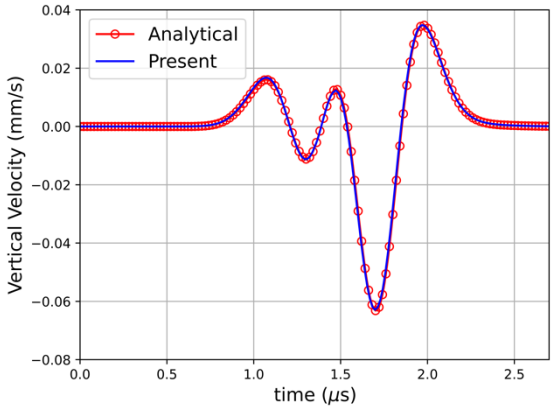

(c)

Figure 2-6. Comparison between the present numerical results and the semi-analytical results of Gar6more3D [122] for (a) the dynamic pressure, (b) horizontal velocity, and (c) vertical velocity.

2.4.3 ULTRASOUND BUBBLE RIGID WALL INTERACTION

The ultrasound-bubble rigid wall interaction is validated against published results [123]. The case features a 35MPa lithotripter pulse impacting an air bubble of initial radius R_0 above a rigid wall at a distance D. The schematic of the case is shown in Figure 2-7a. The computational domain spans $L_x = 5R_0$ and $L_y = 10R_0$ where $R_0 = 50$ µm. To save computational time, the simulations were conducted using an axisymmetric formulation with $\beta = 1$. The base mesh of $N_x = 256$ and $N_y = 512$ cells is used, resulting in 131,072 initial cells prior to refinement; the corresponding mesh spacing is $\Delta x = 9.76 \cdot 10^{-4}$ mm. Two levels of refinement have been used. The top boundary is used to propagate the lithotripter pulse while an outflow boundary condition is imposed on the right and lower boundaries; the left boundary is the axis of symmetry. A CFL number of 0.1 was imposed to preserve the explicit scheme's numerical stability. The density of the water is initially $\rho_{water} = 998.2\ \mathrm{kg \cdot m^{-3}}$ while the thermodynamic parameters for the water are $\gamma_{water} = 6.59$, $p_{\infty,\mathrm{water}} = 4049$ atm, and $b_{water} = q_{water} = 0$ as reported in [123]. The parameters for the air are $\gamma_{air} = 1.4$, $p_{\infty,\mathrm{air}} = 0 = q_{air} = 0$ which results in considering an ideal gas with an initial density $\rho_{air} = 1.225\ \mathrm{kg.m^{-3}}$.

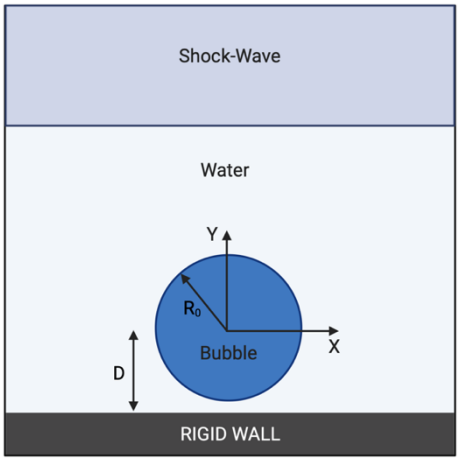

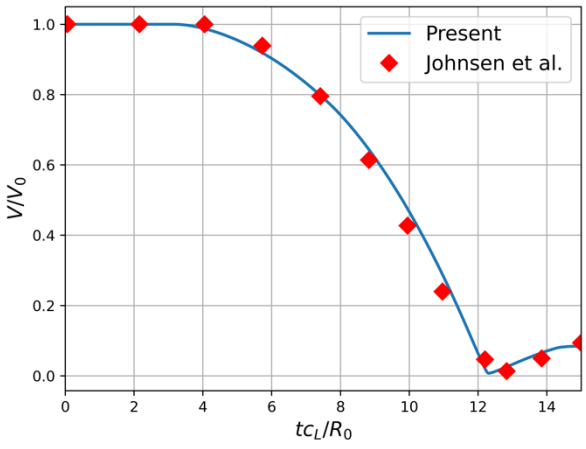

(a) (b)

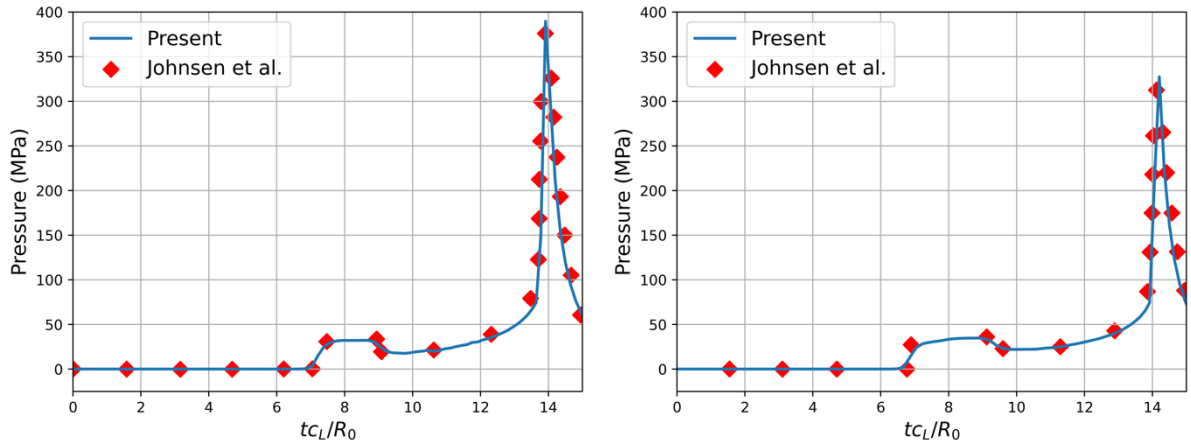

(c) (d)

Figure 2-7. The ultrasound-induced collapse of an air bubble near a rigid wall at a standoff distance $D/R_0 = 2$. Comparison of the present results with the reference [123] (a) Temporal evolution of the pressure at probe location $x/R_0 = 0$ (b) Temporal evolution of the pressure at probe location $x/R_0 = 1$.

The comparison between the present results and the reference is presented in Figure 2-7b-d. The temporal evolution of the dimensionless air volume and the wall pressure at two probe locations are shown. The collapse of the bubble is initiated by the ultrasound impact leading to an adverse pressure gradient forming. The pressure elevation due to the incoming ultrasound is seen in Figure 2-7c-d as the first spike in pressure. The following decrease in pressure is the rarefaction wave coming from the bubble interface. The ultrasound is reflected off the rigid wall and impacts the bubble a second time precipitating the collapse. The emitted spherical shock by the bubble collapse is captured by both probes. The results are found to be in excellent agreement as seen in Figure 2-7a-d.

3 INVESTIGATION OF ULTRASOUND-INDUCED COLLAPSE OF BUBBLES NEAR SOFT MATERIALS

3.1 RESULTS AND DISCUSSION

The objective of this section is to provide a deeper understanding of the complex dynamics of the ultrasound-induced collapse of bubbles near soft materials. More specifically, the case of an ultrasound-induced bubble collapse near tissue-mimicking materials has been simulated; an in-depth explanation of the first case simulated is initially presented, followed by cases revealing the effects of shear modulus, bubble radius, and the standoff distance on the deformation and stresses developed in the deforming soft material. The gas bubble is at mechanical equilibrium with the surrounding medium initially. The schematic of the case is presented in Figure 3-1a:

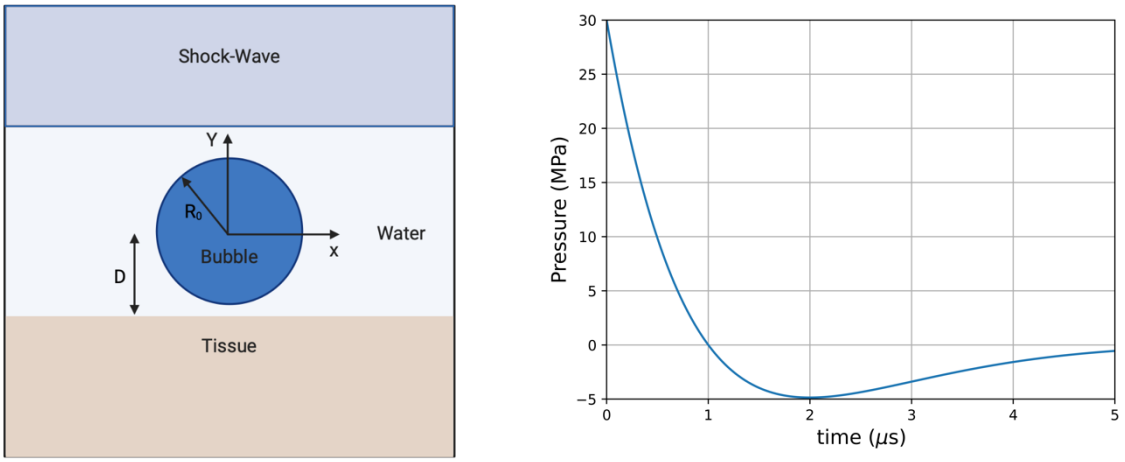

(a) (b)

Figure 3-1. (a) Schematic of the ultrasound-bubble-tissue problem (b) Temporal evolution of the lithotripter pulse.

The ultrasound shockwave is chosen to be similar to that produced by a Dornier HM3 lithotripter where $p_s = 30$ MPa is the pulse amplitude, $\alpha = 9.1 \cdot 10^5$ and $\omega = 2\pi f$ with $f = 83.3 \cdot 10^3$ Hz. The analytical function of the waveform [124] is defined as:

$$p(t) = p_0 + 2p_s e^{-\alpha t} \cos\left(\omega t + \frac{\pi}{3}\right), \quad (40)$$

where $p_0$is the atmospheric pressure. The temporal evolution of the lithotripter pulse is shown in Figure 3-1b. The bubble radii under consideration were chosen to reflect typical bubble sizes in diagnostic and therapeutic applications of bubbles in medicine [2], [125] where $R_0 = 10$ μm, $R_0 = 5$ μm, $R_0 = 2.5$ μm. Three soft materials have been considered; their shear modulus

spans over 3 orders of magnitude, which correspond to three well-characterized tissues [126]: liver, gallbladder, and bile duct tissue [127]. The corresponding parameters of the EoS utilized to characterize them are summarized in Table 3-1.

Table 3-1. Thermodynamics parameters of the three soft materials

Tissue	$\boldsymbol{\rho}$ $\boldsymbol{(kg.m^{-3})}$	$\boldsymbol{\mu}$ $\boldsymbol{(Pa)}$	$\boldsymbol{\gamma}$	$\boldsymbol{p_{\infty}(Pa)}$
Liver	1060	$1{,}8 \cdot 10^{3}$	4.4	599023259
Gallbladder	1060	$8{,}5 \cdot 10^{4}$	4.4	616576970
Bile duct	1060	$1{,}66 \cdot 10^{5}$	4.4	604328642

To save computational time, the simulations were conducted using an axisymmetric formulation with $\beta = 1$. The computational domain spans at $L_x = 0.25$ mm and $L_y = 0.5$ mm. The base mesh of $N_x = 256$ and $N_y = 512$ cells is used, resulting in 131,072 initial cells prior to refinement; the corresponding mesh spacing is $\Delta x = 9.76 \cdot 10^{-4}$ mm. Three levels of refinement have been considered, based on the refinement criterion. The top boundary is used to propagate the lithotripter pulse (40) while an outflow boundary condition is imposed on the right and lower boundaries; the left boundary is the axis of symmetry. To preserve the numerical stability of the explicit scheme, a CFL number of 0.1 was imposed in all subsequent simulations.

With regard to the interaction between the collapsing bubbles and the nearby solid material, many studies have been reported [128], [129], [130], [131], [132]. Cavitation damage in solid materials primarily stems from shock waves and liquid jets produced during the bubble's collapse. The shock waves exert pressure spikes that can lead to fatigue and micro-cracking, while the liquid jet's impact can cause pitting and erosion; repeated occurrences can lead to severe degradation of the surface. For soft materials, it is generally known that the liquid jet is the prevailing mechanism for their damage [133], [134]. Biological tissue can be damaged through various mechanical loads, including compressive, tensile, and shear forces [135]. These forces can lead to different types of damage or injury depending on the nature and duration of the applied force, and the type of tissue [136]. The type of tissue (e.g., bone, muscle, ligament) and the specific mechanical properties of that tissue will determine its susceptibility to different

types of mechanical forces. For example, bones [137] are more resilient to compressive forces but can be more vulnerable to tensile and torsional forces. Soft tissues which are considered in this paper, like muscles and ligaments might be more prone to damage through excessive stretching or tensile forces [138]. The specific damage mechanism of bubble collapse for hard materials such as metals is widely debated [118]. To further elaborate on the details of this mechanism, the maximum, minimum principal stress and maximum shear stress are computed:

$$\sigma_{max,PS} = \frac{\sigma_{xx} + \sigma_{yy}}{2} + \sqrt{\left(\frac{\sigma_{xx} - \sigma_{yy}}{2}\right)^2 + {\sigma_{xy}}^2} \quad (41)$$

$$\sigma_{min,PS} = \frac{\sigma_{xx} + \sigma_{yy}}{2} - \sqrt{\left(\frac{\sigma_{xx} - \sigma_{yy}}{2}\right)^2 + {\sigma_{xy}}^2} \quad (42)$$

$$\sigma_{MSS} = \sqrt{\left(\frac{\sigma_{xx} - \sigma_{yy}}{2}\right)^2 + {\sigma_{xy}}^2} \quad (43)$$

By visualizing these stresses, the directional nature of the stress state in the material and areas of potential material failure can be understood and identified. Particularly, areas, where the maximum principal stress (tensile) exceeds the tensile strength of the material, are likely failure points.

3.1.1 DYNAMICS OF THE ULTRASOUND-BUBBLE TISSUE INTERACTION

In this section we present an in-depth analysis of the ultrasound-induced collapse of an air bubble with a radius $R_0 = 10$ µm placed above a soft material at a standoff distance $S_d = 1.1R_0$ whose properties are representative of the gallbladder. The corresponding parameters of the EoS utilized to characterize it are summarized in Table 3-1. In Figure 3-2, the block-structured adaptive mesh refinement is depicted.

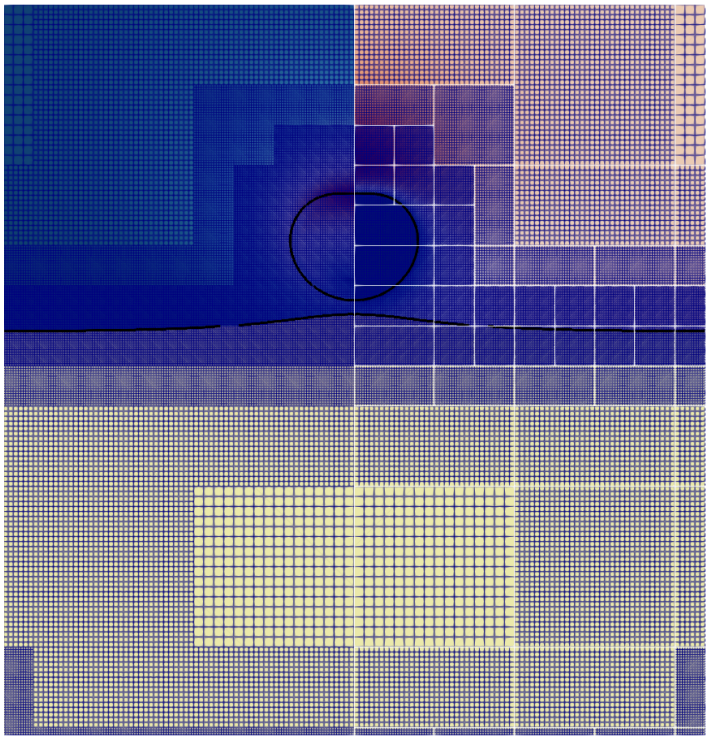

Figure 3-2. Block-structured adaptive mesh refinement visualization of the ultrasound-induced collapse of an air bubble of $R_0 = 10\ \mu m$ with an initial stand-off $d/R_0 = 1.1$ near gallbladder. The white outline delimits the blocks.

The temporal evolution of the air volume normalized by its initial value is presented in Figure 3-3a. The bubble remains at its initial radius until the shockwave impacts it leading to the generation of a pressure gradient. The temporal evolution of the penetration depth into the tissue at the center axis can also be seen in Figure 3-3b. From Figure 3-3b we can identify 3 different stages: the collapse stage up to ~0.2 μs, followed by the penetration stage until ~0.6 μs, and finally the tissue rebound stage where the penetration of the liquid jet slows down due to elastic forces. The collapse process of the bubble starts ~0.15 μs, and it reaches its minimum radius of around ~0.2 μs. The tissue is pulled upwards during the first collapse as evidenced by the negative penetration depth in Figure 3-3b. This is also shown in Figure 3-4b. The temporal evolution of the surface integrals of the maximum, minimum principal stress, and maximum shear stress over a small area of the tissue were computed and shown in Figure 3-3c. We observe a slight increase in principal and shear stress at collapse suggesting the emitted shockwave produced a small deformation. Given the small acoustic impedance mismatch between the water and the tissue, here modeled as gallbladder the stresses produced are rather insignificant. After the first collapse, the liquid jet starts penetrating the tissue where multiple bubble collapses and rebounds are observed Figure 3-3a. It is during the penetration stage that the tissue

experiences the highest stresses as depicted in Figure 3-3c. The maximum principal stress is observed to be approximately double the minimum principal stress around ~0.42 µs showing that the tensile forces are much greater than the compressive forces. This is an important finding as soft materials like biological tissue are more susceptible to tensile damage as explained in section 5. In the last stage of this process, the bubble experiences smaller collapses and rebounds and on average increases in volume Figure 3-3a. However, the penetration of the liquid jet has been slowed as can be seen by the decrease in slope in Figure 3-3b after ~0.6 µs.

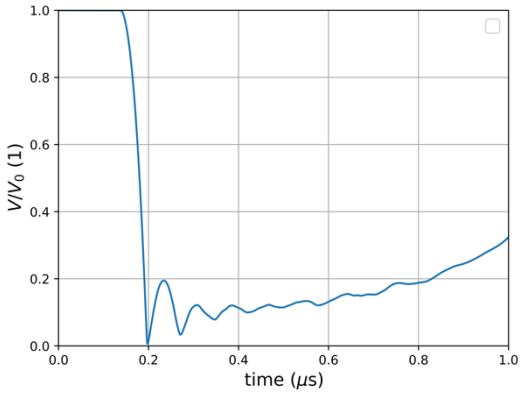

(a)

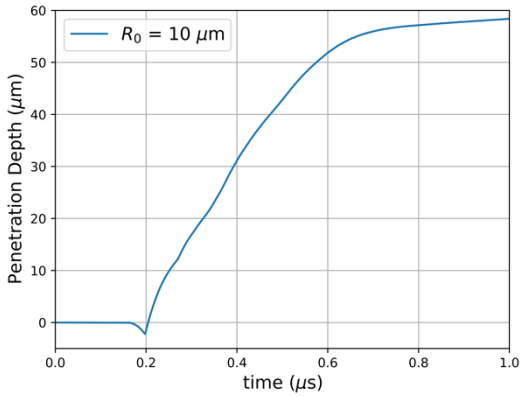

(b)

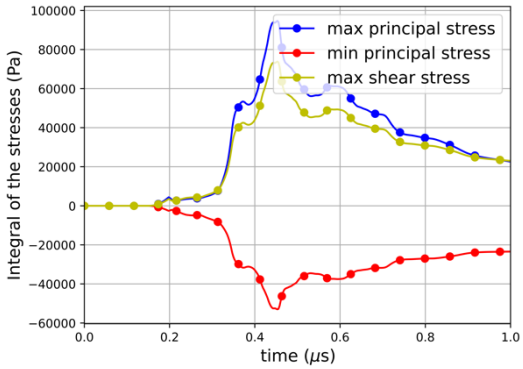

(c)

Figure 3-3. Ultrasound-induced collapse of an air bubble of $R_0 = 10\ \mu m$ with an initial stand-off $d/R_0 = 1.1$ near gallbladder (a) Temporal evolution of the normalized air volume (b) Temporal evolution of the penetration depth of the liquid jet (c) Temporal evolution of the integral of the maximum, minimum principal stress, and maximum shear stress.

In Figure 3-4, the ultrasound-induced collapse near gallbladder is depicted for nine different timesteps with a black isosurface separating the three materials. The maximum principal stress inside the tissue, the velocity magnitude and pressure in the water and air are depicted. In the first instance Figure 3-4a, the lithotripter pulse already impacted the bubble and propagated

inside the tissue. Given the very similar acoustic impedance between water and gallbladder, the pulse is entirely transmitted inside the tissue as observed in Figure 3-6. At the distal side of the bubble a rarefaction wave propagating outward was generated given the impedance mismatch between the water and air phase.

The dynamic of bubbles during extracorporeal shockwave lithotripsy near gelatin was studied in [139] using a 10.2 MPa pulse and millimeter sized bubbles. Both the transmission of the lithotripter pulse into the gelatin and the rarefaction wave have been experimentally observed.

In Figure 3-4a, the adverse pressure gradient is seen where the distal side of the bubble contracted starting the collapse process. The low-pressure region at the proximal side of the bubble creates a sink flow where the tissue is pulled toward the bubble.

Although the elongation of the tissue towards the bubble during the first collapse has not been observed in [139], it has been documented in laser-induced bubbles close to tissue mimicking materials [51], [140], [141]. The limitations in movie resolutions of the experimental setup could be responsible. Moreover, the weaker lithotripter pulse and a bigger bubble size in their experiment contributes to a weaker collapse, and thus resulting in a weaker sink flow.

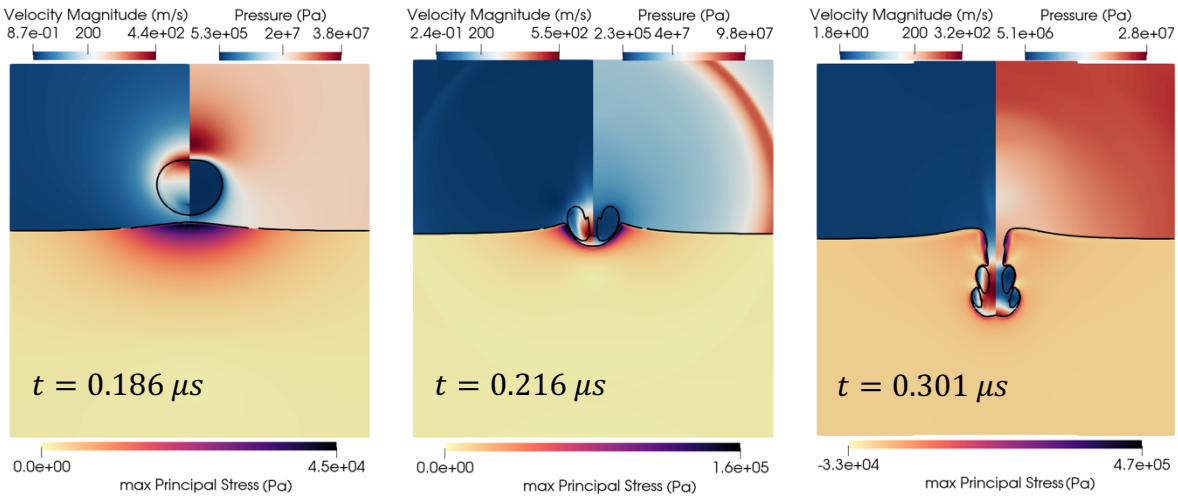

(a) (d) (g)

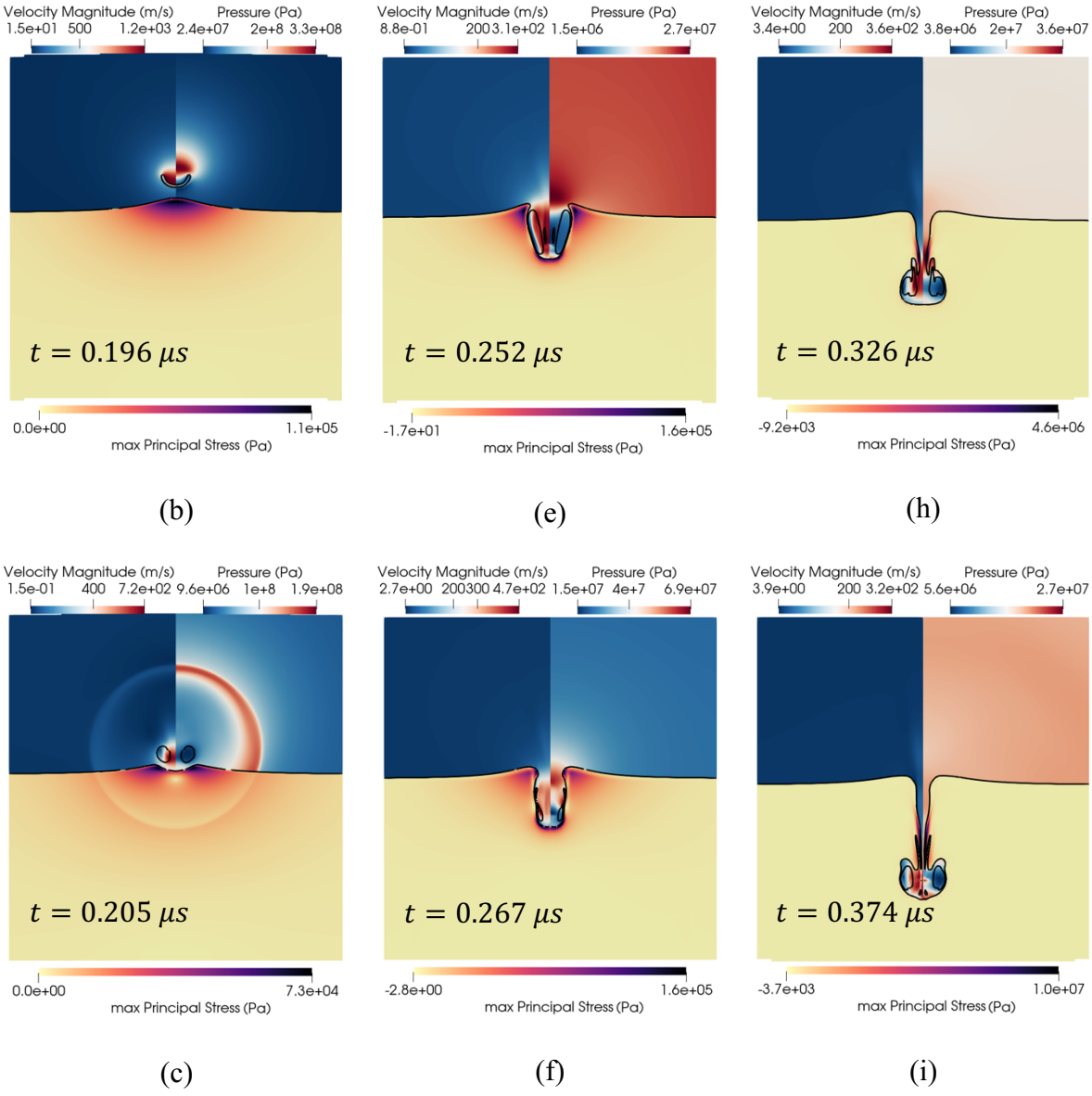

Figure 3-4. Ultrasound-induced collapse of an air bubble of $R_0 = 10\ \mu m$ with an initial stand-off $d/R_0 = 1.1$ near gallbladder at different timesteps. The black isosurface separates the three materials and is defined by $\alpha_k = 0.5$. Upper left hand: contour of velocity magnitude. Upper right hand: contour of pressure. Bottom half: contour of the maximum principal stress.

The deformation induces stresses in a spherical like shape where the stresses are highest right under the bubble and gradually decreases to zero further away. Moments before the collapse, the liquid jet peaks at velocities $\sim 1200\ m/s$ and the tissue is seen to have been further pulled inwards towards the bubble where the maximum principal stress has increased by an order of magnitude. The high velocity liquid jet has been reported in experiments to be able to perforate membranes like aluminum foil [142].

To better visualize the shock waves numerical schlieren were plotted in Figure 3-6 based on the following formula [143]:

$$\phi = \exp\left(-\frac{k|\Delta\rho|}{max|\Delta\rho|}\right). \quad (44)$$

In Figure 3-6a, the water-hammer shock, and the precursor shock right after the collapse are seen. Once the liquid jet penetrates the proximal side of the bubble a toroidal bubble is observed in Figure 3-4c. The subsequent collapse of the bubble generates a spherical shock wave traveling outward both in the water and the tissue where small stresses are observed. This primary shock is also shown in Figure 3-6b. The liquid jet already pushed the tissue inward, compressing it in Figure 3-4c and started to penetrate. The shape of the maximum principal stress has changed compared to the pre-collapse phase. The highest maximum principal stress at this timestep is observed in the periphery of the impact location while compressive forces are seen at the centroid. The liquid jet continues its inward motion inside the tissue as depicted in Figure 3-4d while the bubble rebounds and increases in size. Both the bubble and the liquid jet are then fully surrounded by the tissue in Figure 3-4e where the bubble is seen with an elongated shape. A second smaller toroidal bubble is also observed. The upper part of the tissue forming a tip and the impact location is seen to experience significant tensile forces while the sides are seen to be compressed.

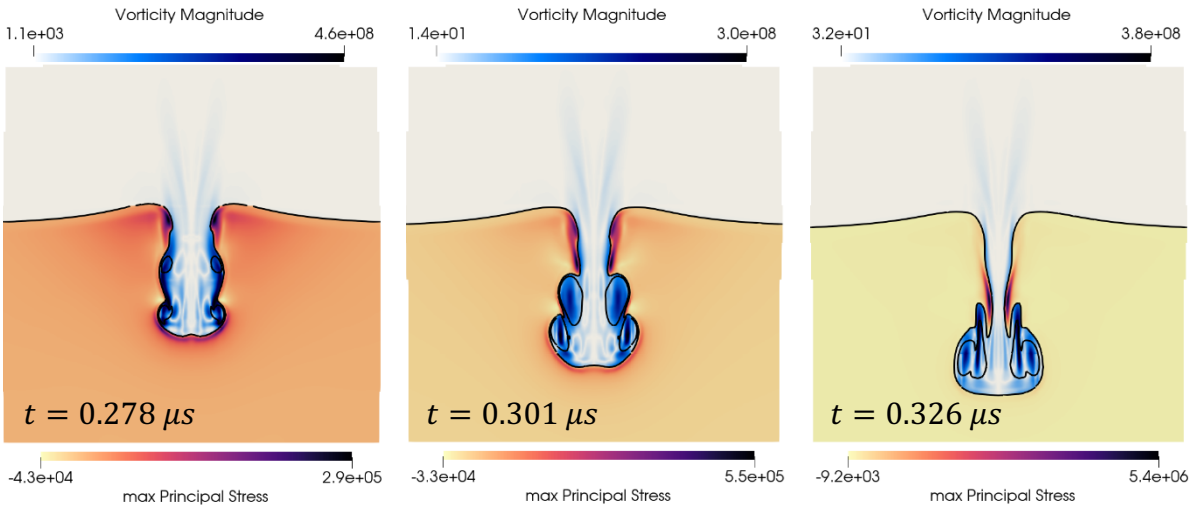

(a) (b) (c)

Figure 3-5. Contours of vorticity and maximum principal stress at different timesteps.

At this point, the toroidal bubble collapses for the second time as seen in Figure 3-4f, and an upward moving shock is emitted.

In [139] the shockwave-induced collapse of a bubble near gelatin is described. The shock due to bubble collapse is first seen, followed by the liquid jet impacting the gelatin and compressing it similarly as in Figure 3-4c. The maximum principal stress in Figure 3-4c shows an inflection point where the tissue is not only compressed at the impact point but also experiences tensile forces when moving away from the center. The bubble is then observed in [100] to both penetrate the gelatin and rebound while the centroid of the bubble is moving downstream which is consistent with Figure 3-4d. Notably, the primary shock depicted in Figure 3-6b and a secondary shock is observed in [100] although in their experiments it is not clear if the bubble splits into two toroidal bubbles since it is not possible to observe inside the gelatin.

The tip of the tissue is also observed to be retracting downwards while the shape of the stresses remains similar to Figure 3-4e. In Figure 3-5, the vorticity magnitude in the two fluid phases and the maximum principal stress in the tissue are shown. High vorticity regions are observed along the outward tissue walls moments after the secondary collapse as seen in Figure 3-5a. This vorticity is responsible for deforming the tissue interface that was previously planar into a curved shape Figure 3-5b. The subsequent secondary collapse created 2 toroidal bubbles that rebounded as seen in Figure 3-4g where the tissue is pinched between the two bubbles. The upper part is getting stretched downward and hence experiences tensile forces close to the water-tissue interface. The secondary collapse shocks are both shown in Figure 3-6c. As the liquid jet continues its downward motion, the two toroidal bubbles experience a third collapse; significant vorticity is present, as shown in Figure 3-5c. Finally, the two bubbles merged into one once again, as shown in Figure 3-4h. The part of the tissue above the upstream torus is pulled downward forming a spike, where most of the tensile forces are present. As the penetration process inside the tissue continues, the spike is further pulled downstream, as evidenced in Figure 3-4i. The maximum principal stress is notably highest very close to the interface where the tissue was penetrated and particularly in the spikes.

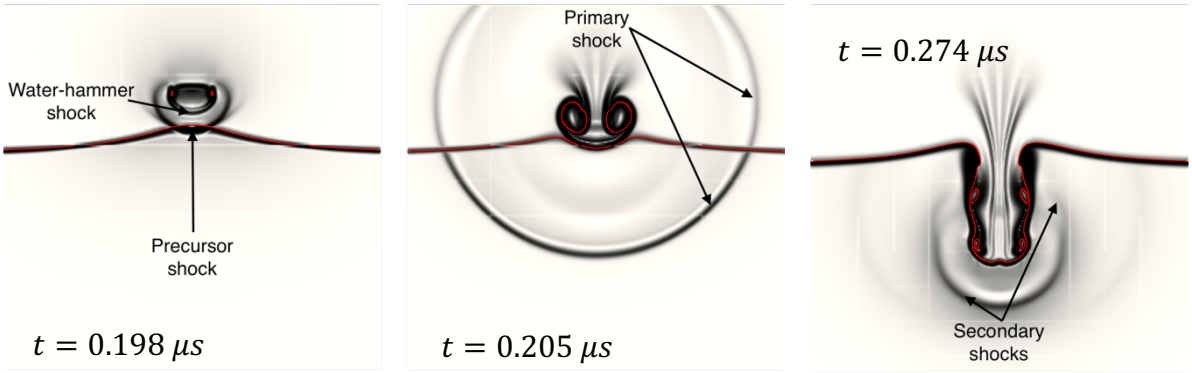

(a) (b) (c)

Figure 3-6. Numerical schlieren at different timesteps where the red isosurface represents the interface between the three materials.

In various experimental studies, the aftermath of bubble collapse is characterized by the formation of a pit within the soft material, serving as evidence of material damage [51], [139], [140], [144], [145]. The primary mechanism responsible for such damage is seemingly attributed to the liquid jet. The present results corroborate these findings and elucidate the dynamic processes that lead to tissue damage. Moreover, the probable sites of such damage are identified, enhancing our understanding of the damage locations within the tissue.

3.1.2 EFFECT OF THE SHEAR MODULUS

In this section, the effect of the shear modulus on both the bubble and solid dynamics was studied by selecting two additional tissues: liver and bile duct. The corresponding parameters of the EoS utilized to characterize them are summarized in Table 3-1. In Figure 3-7, the temporal evolution of the normalized air volume, penetration depth and surface integrals of the stresses are presented. The change in shear modulus is seen in Figure 3-7a to have a small impact on the bubble dynamics. The early stage of the bubble dynamics is observed to be identical up to the third collapse where the normalized air volume starts to vary for the different tissues. This finding is consistent with the hypothesis that the early stage of the simulation is ultrasound-driven due to the small acoustic impedance mismatch. In Figure 3-7b, the penetration depth into the tissues is observed to be similar up to the end of the penetration stage. Later the speed of the penetration slows down and the tissue with the lowest shear modulus, the liver is clearly seen to be penetrated more than the strongest soft tissue selected: the bile duct.

The surface integrals of the maximum, minimum principal stress and maximum shear stress are plotted in Figure 3-7c-e. The increase in shear modulus is observed to induce higher stresses across the 3 metrics measured. It is consistent with the fact that the strongest soft tissue deforms less than the softest and can also be seen in Figure 3-7b with the penetration depth. The effect of the shear modulus on the penetration depth and deformation has also been assessed in experiments [144]. It was observed that both the penetration depth and the deformation of the tissue-mimicking material decreased with increasing shear modulus. The same observations are made in this work whereby the increase of the shear modulus is demonstrated to decrease the penetration depth in late stages as depicted in Figure 3-7b, and the deformation seen by the reduction in elongation in Figure 3-8. Across the 3 metrics of stress measured and for the selected tissues, the maximum principal stress is seen to be the highest.

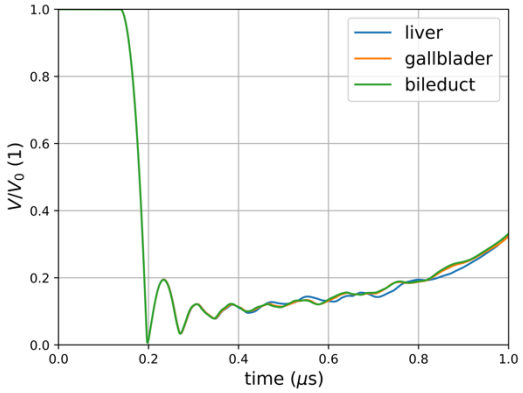

(a)

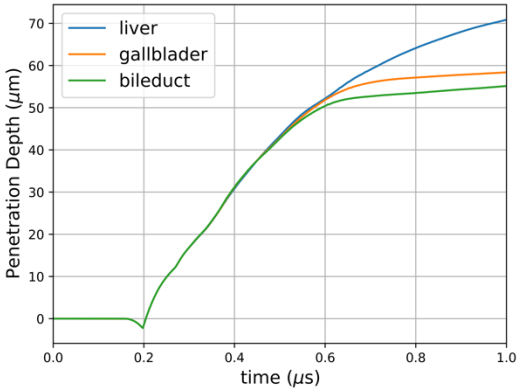

(b)

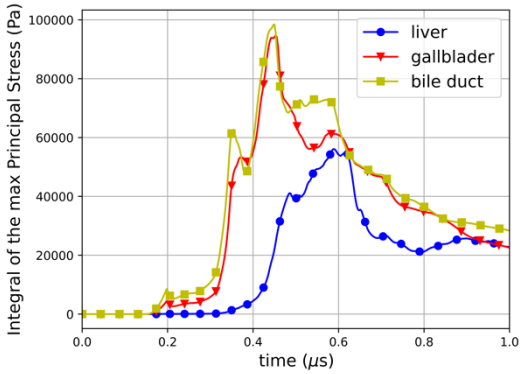

(c)

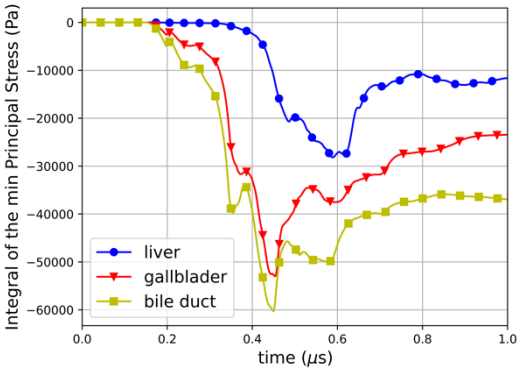

(d)

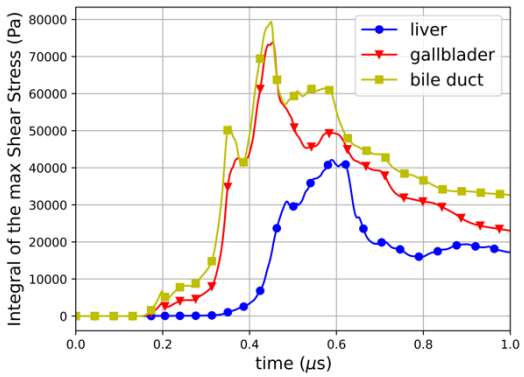

(e)

Figure 3-7. Effect of the shear modulus (a) Temporal evolution of the normalized air volume (b) Temporal evolution of the penetration depth of the liquid jet for 3 different tissues (c) Integral of the maximum principal stress for 3 different tissues (d) Integral of the minimum principal stress for 3 different tissues (e) Integral of the maximum shear stress for 3 different tissues.

In Figure 3-8, the tri-contours for the liver, gallbladder, and bile duct respectively at $t = 0.373\mu s$ are presented. While the shape of the deformation overall is similar, there are two noticeable differences. At this stage of the process, the upstream entry point for the three different tissues is seen to have different shapes. Indeed, the bile duct which is the strongest soft tissue is observed to have retracted faster than the gallbladder and the liver respectively. Additionally, the entrainment of the tissue due to the vorticity is less prominent with the increase in shear modulus. It can be seen in the three figures where the elongated tissue for the liver reaches downstream close to the liquid jet pit. Whereas in the case of the gallbladder the elongated tissue is above the toroidal bubble at the same timestep. Similarly, in the case of the bile duct the elongation of the tissue is greatly reduced compared to the two other tissues at that time. Lastly, the bubble shape, velocity and pressure are observed to be the same in the three cases presented demonstrating again that the increase in shear modulus does not impact the bubble dynamics at this stage of the process.

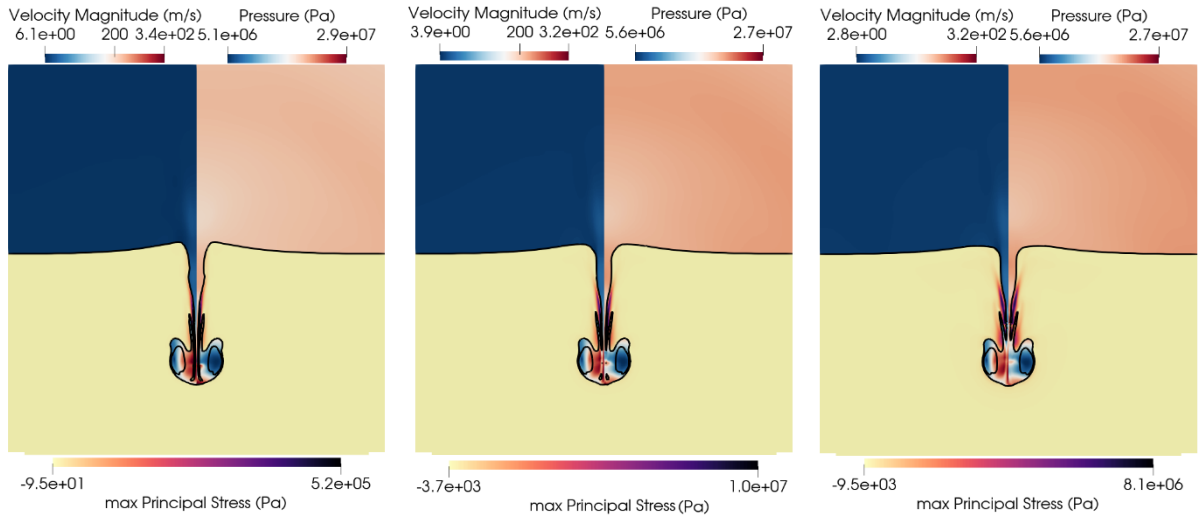

(a) (b) (c)

Figure 3-8. Effect of the shear modulus on the shape of the deformation at $t = 0.373$ μs (a) Tri-contours of the liver (b) Tri-contours of the gallbladder (c) Tri-contours of the bile duct.

3.1.3 EFFECT OF THE BUBBLE RADIUS

In this section, the effect of the bubble radius is investigated by selecting bubble radii found in therapeutic applications [125]. The initial bubble radii R_0 are chosen to be 10 μm, 5 μm, and 2.5 μm and gallbladder is selected for the three cases presented while the standoff distance is kept at $S_d = 1.1R_0$. In Figure 3-9, the temporal evolution of the normalized air volume, penetration depth and surface integrals of the stresses are presented for the different bubble radii. First, the bubble dynamics are naturally seen to be significantly different in Figure 3-9a where the collapse times, minimum radii, and rebound radii change. Second, the bubble radius is seen to have a major effect on the penetration depth in Figure 3-9b. Indeed, all three identified stages are affected. In the collapse stage, the pulling effect of the tissue is less prominent for the smaller bubbles. This result is consistent with our hypothesis that the main mechanism behind the pulling effect is the sink flow below the bubble. The penetration stage is observed to be shortened for the smaller bubbles. It can be attributed to the fact that the collapse is milder as the bubble is smaller and the subsequent liquid jet reaches smaller velocities. The rebound stage although happening earlier exhibits the same behavior for all radii where the penetration of the velocity liquid jet is greatly reduced. Lastly, another major finding is the importance of the bubble size on the stresses experienced by the tissue. In Figure 3-9c-e,

the maximum, minimum principal stresses, and maximum shear stress are plotted. The trend of the bigger bubble to produce higher stresses is clearly observed.

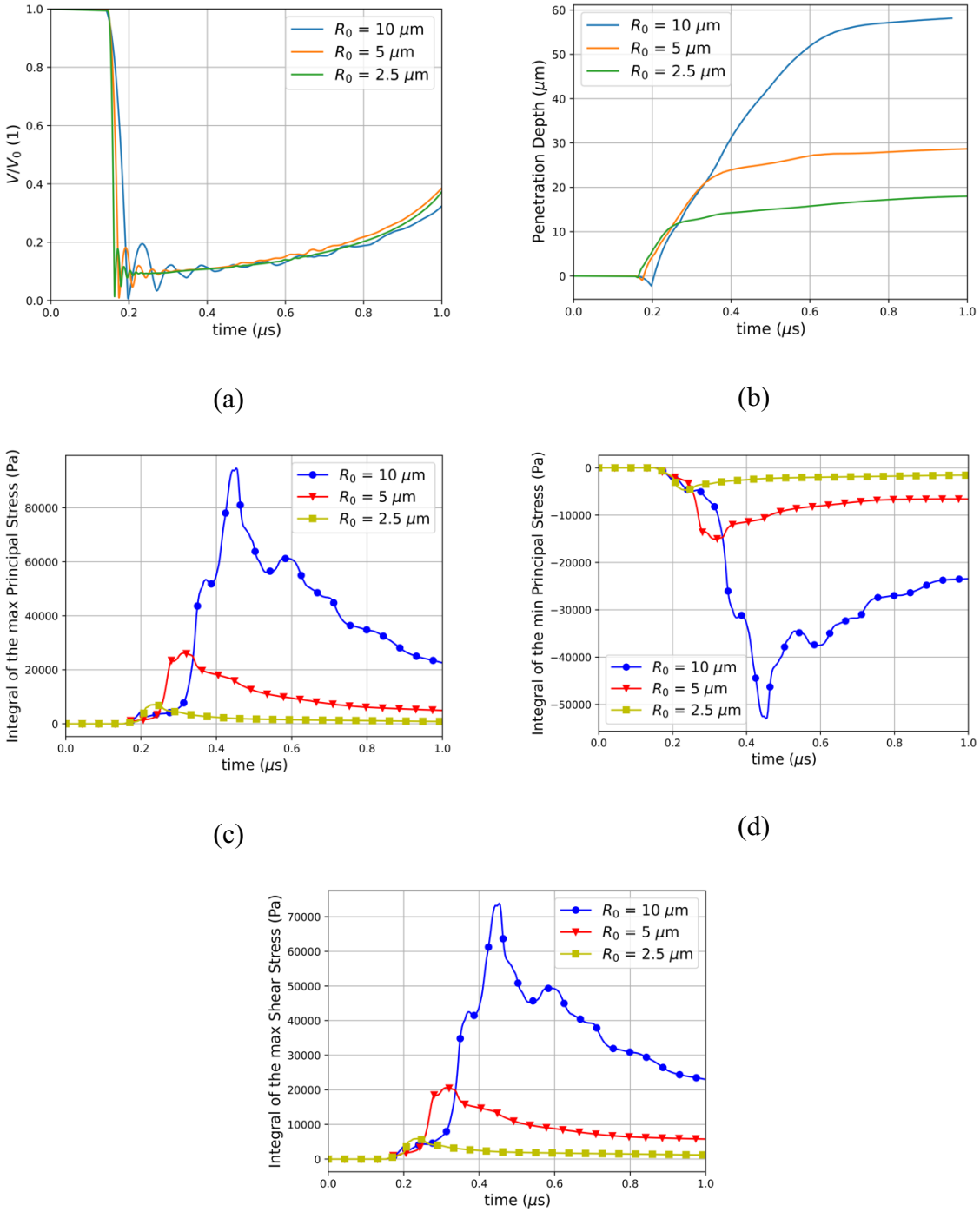

Figure 3-9. Effect of the initial bubble radius (a) Temporal evolution of the normalized air volume (b) Temporal evolution of the penetration depth of the liquid jet for 3 different bubble radii (c) Integral of

the maximum principal stress for 3 different bubble radii (d) Integral of the minimum principal stress for 3 different bubble radii (e) Integral of the maximum shear stress for 3 different bubble radii.

The effect of the initial bubble radius on the deformation and the penetration depth was examined in [139], [144]. It was found that larger bubble resulted in an increased penetration depth as well as an increase in the damage pit radius. In Figure 3-9b, the same correlation of the penetration depth on the initial bubble radius is found. This finding has significant importance for mitigating cavitation-related injuries where bubble sizes can be carefully chosen for specific treatments.

3.1.4 EFFECT OF THE STANDOFF DISTANCE

In this section, the effect of the standoff distance on the bubble dynamics and the deformation is presented herein. Three standoff distances are examined: $S_d = 1.1R_0$, $S_d = 2.0R_0$, $S_d = 3.0R_0$ where $R_0 = 10\ \mu m$. The temporal evolution of the air volume normalized by its initial value is depicted in Figure 3-10a for the three standoff distances. The bubble's collapse time is observed to be the same for all three cases. Differences in bubble dynamics become more pronounced after the third collapse, with the greatest standoff distance showing the most significant variations. For two smallest standoff distances the second and third collapse occur while the bubble is engulfed by the tissue which is not the case for $S_d = 3.0R_0$. We observed that this difference could be due to the elastic forces the bubble must overcome to grow while engulfed in the tissue. The temporal evolution of the penetration depth into the tissue at the center axis can also be seen in Figure 3-10b for the three standoff distances. The suction effect during which the tissue is pulled upstream towards the bubble for $S_d = 1.1R_0$ is not observed for $S_d = 2.0R_0$ and $S_d = 3.0R_0$. The velocity of the penetration depth as depicted by the slope in Figure 3-10b is seen to be similar during the penetration process for all standoff distances. The later dynamics exhibit a notable difference where the two smallest standoff distances reach the tissue rebound stage sooner than the largest standoff distance. The temporal evolution of the surface integrals of the maximum, minimum principal stress and maximum shear stress are presented in Figure 3-10c-e. A clear correlation between the standoff distance and the stresses is observed. The smallest standoff distances are depicted to induce higher stresses. These insights are pivotal for the development of strategies aimed at mitigating cavitation-induced tissue damage in therapeutic applications.

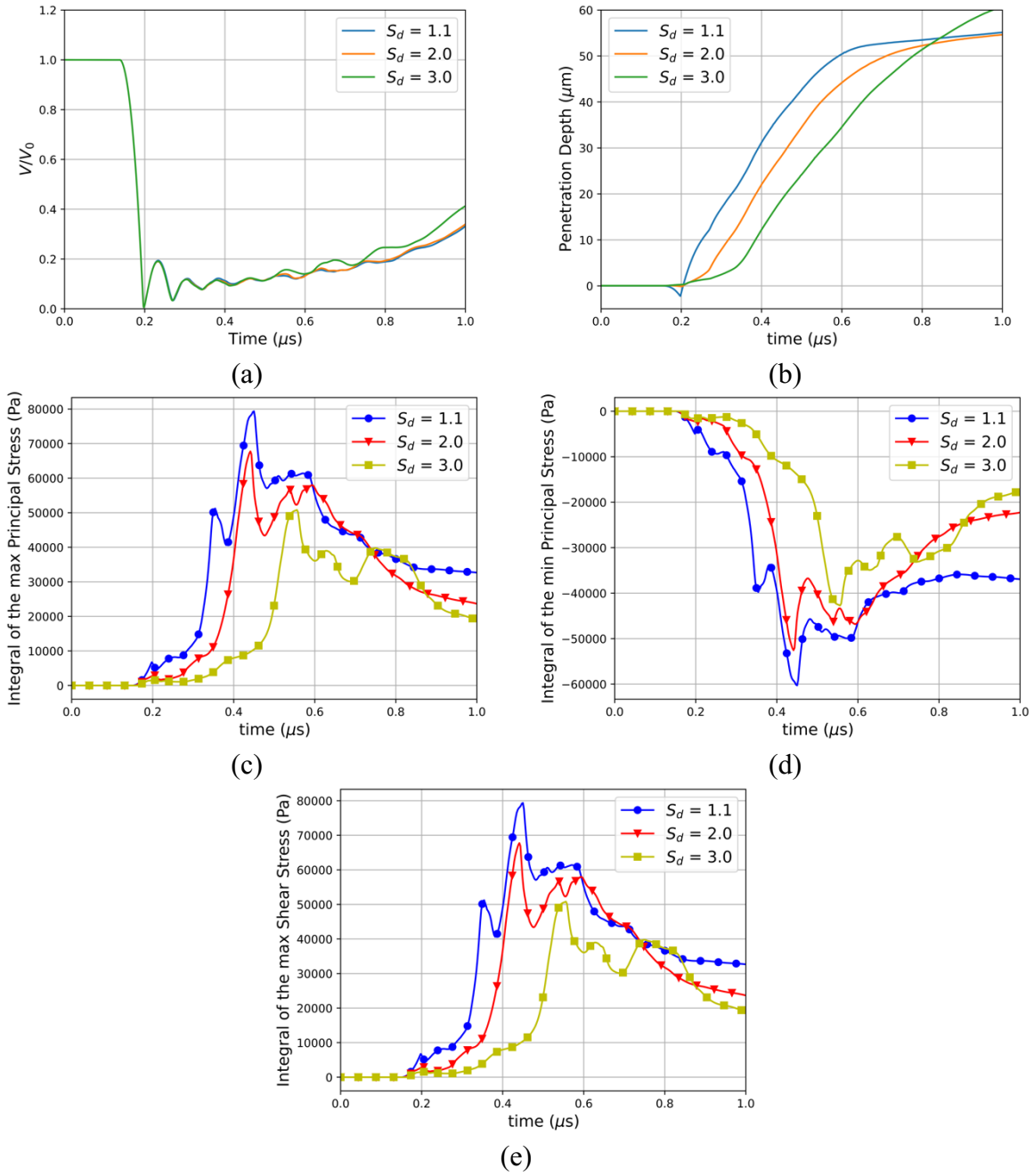

Figure 3-10. Effect of the standoff distance (a) Temporal evolution of the normalized air volume (b) Temporal evolution of the penetration depth of the liquid jet for 3 different standoff distances (c) Integral of the maximum principal stress for 3 different standoff distances (d) Integral of the minimum principal stress for 3 different standoff distances (e) Integral of the maximum shear stress for 3 different standoff distances.

In Figure 3-11, the effect of the standoff distance on the ultrasound-induced collapse of an air bubble of $R_0 = 10\ \mu m$ near bileduct for $S_d = 1.1R_0$, $S_d = 2.0R_0$ and $S_d = 3.0R_0$ is depicted for three timestep at $t = 0.19\ \mu s$, $t = 0.31\ \mu s$, and $t = 0.44\ \mu s$. The first presented timestep at $t = 0.19\ \mu s$ in Figure 3-11a demonstrates the effect of the standoff distance on the suction effect. As the standoff distance increases the protrusion of the tissue upstream toward

the bubble decreases. This trend corroborates the proposed hypothesis, implicating the sink flow beneath the bubble as the primary mechanism driving this protrusion. The second presented timestep at $t = 0.31\ \mu s$ in Figure 3-11b corresponds to the third collapse as seen in Figure 3-10a. The early bubble dynamics are shown not to be affected by the standoff distance as the shape of the bubble remains the same across the three standoff distances. Nevertheless, the bubble exhibits distinct phases within the penetration process, as evidenced by the observed variations in penetration depth in Figure 3-11b. In fact, the lowest standoff distance $S_d = 1.1R_0$ is seen to experience the highest stresses at this timestep as evidenced in Figure 3-10c-e. The observations at the final presented timestep at $t = 0.44\ \mu s$ in Figure 3-11c are consistent with earlier findings, showing that the bubble maintains its shape across the various standoff, yet is situated at different penetration depths and experiences higher stresses as the standoff distance decreases.

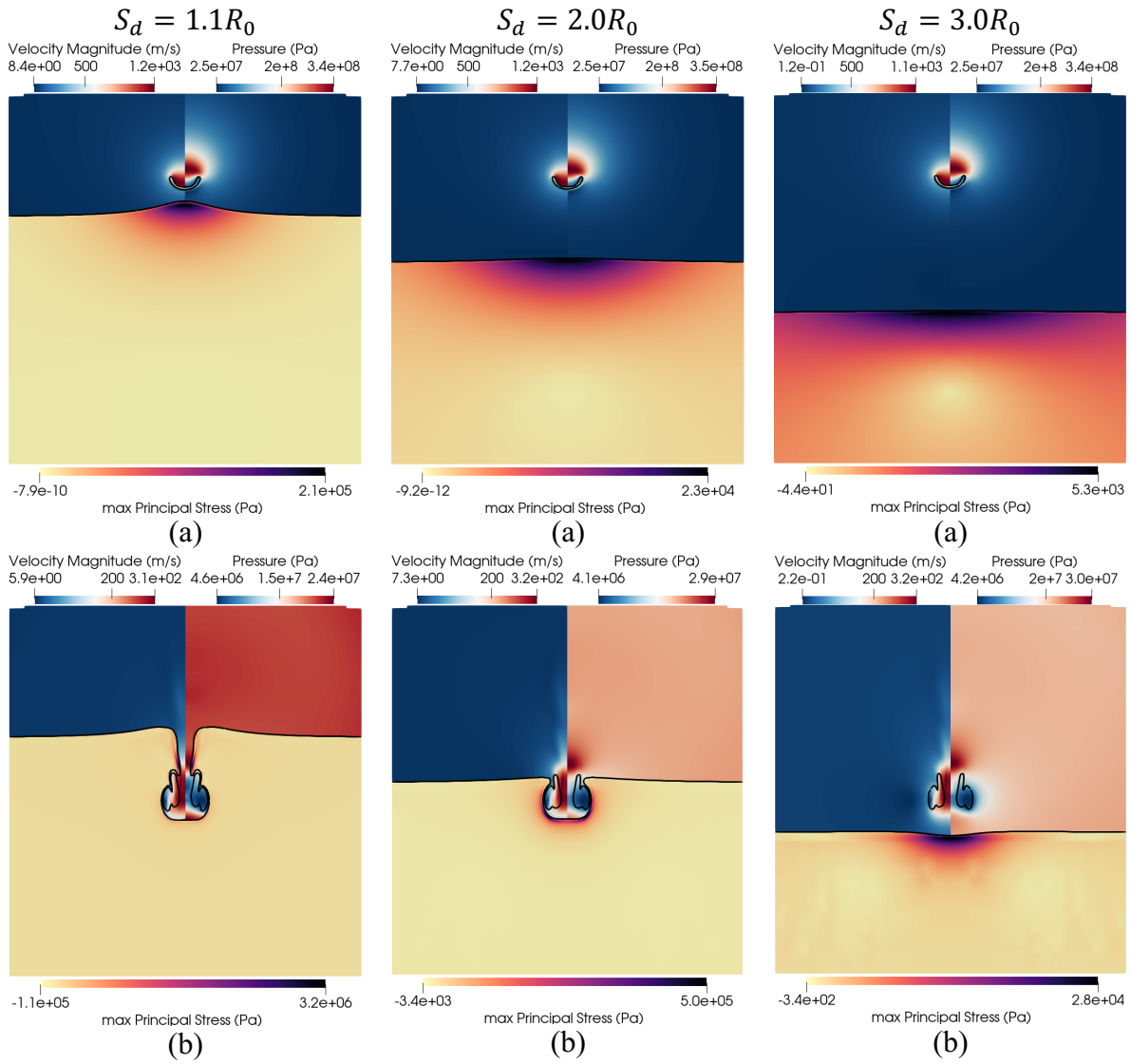

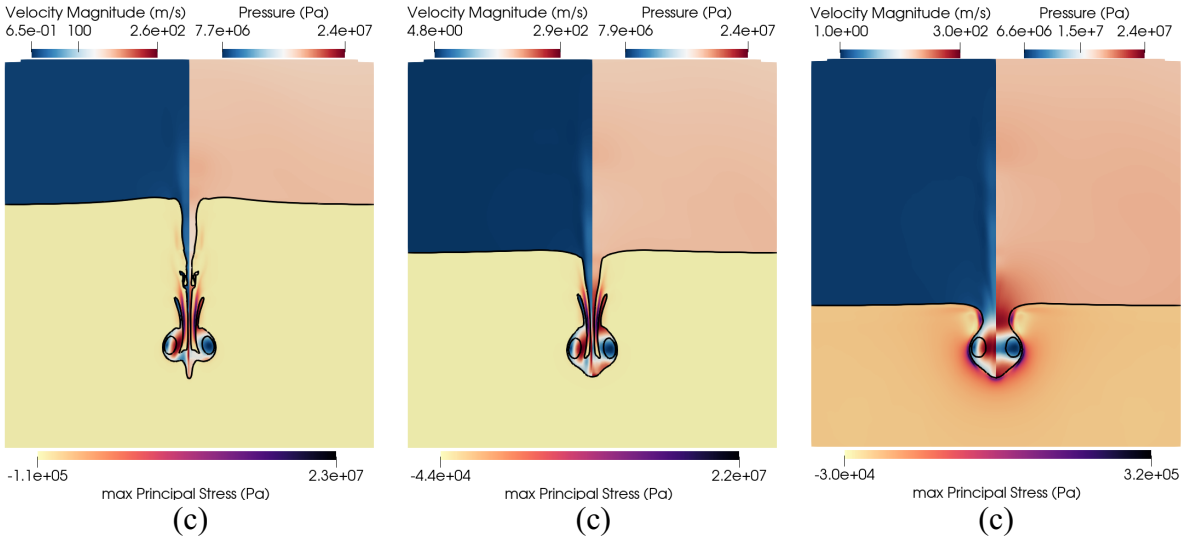

Figure 3-11. Effect of the standoff distance. Ultrasound-induced collapse of an air bubble of $R_0 = 10\ \mu m$ near bileduct at $t = 0.19\ \mu s$, $t = 0.31\ \mu s$, and $t = 0.44\ \mu s$ for standoff distances $S_d = 1.1R_0$, $S_d = 2.0R_0$ and $S_d = 3.0R_0$. The black isosurface separates the three materials and is defined by $\alpha_k = 0.5$. Upper left hand: contour of velocity magnitude. Upper right hand: contour of pressure. Bottom half: contour of the maximum principal stress.

3.2 SUMMARY

A numerical investigation of ultrasound-induced collapse of air bubbles near soft materials was presented using a novel multi-material DIM model with AMR. To have a better understanding of the complex interactions of the ultrasound-bubble-tissue flow, the effect of the shear modulus and of the bubble radius was investigated. The shear moduli were chosen for well-characterized tissues spanning over three orders of magnitude. The bubble radii considered are found in biological flows. Insights into the nature of the mechanical loads experienced by the soft material through the visualization of the maximum and minimum principal stress and maximum shear stress were presented.

Our findings reveal that the tissue predominantly experiences tensile forces compared to compressive or shear forces, suggesting that injuries are mainly tensile-driven. Concurrently, areas of maximum tensile forces align closely with regions where the tissue undergoes elongation. Furthermore, we identify that the bubble radius plays a pivotal role in the stresses experienced by the soft material, emphasizing its importance in medical applications. Meanwhile, variations in shear modulus, while having a minimal impact on early bubble dynamics, noticeably influence the penetration process in later stages as well as the shape of

the deformations. Finally, it is found that smaller standoff distances lead to greater bubble-tissue interaction resulting in higher stresses in the tissue while the bubble dynamics are not notably affected.

This work contributes valuable insights into the complex interplay between bubble collapse, acoustic fields, and tissues, paving the way for improvements in related medical applications.

4 PREDICTION OF SHOCK HEATING DURING ULTRASOUND-INDUCED BUBBLE COLLAPSE USING REAL-FLUID EQUATIONS OF STATE

4.1 RESULTS AND DISCUSSION

In this section, we initially investigate the role of the EoS for a pure water shock tube test case. Following that, a spherical bubble collapse is simulated, and the results are compared with our previous work [90] employing the relaxation model. Both bubble hydrodynamics and thermodynamics are found in excellent agreement, demonstrating the validity of the implementation of the developed tabulated EoS. Subsequently, the effect of the liquid EoS on the spherical bubble collapse is demonstrated for different pressure ratios. Lastly, a 2D non-spherical collapse is simulated for which the liquid temperature along the wall varying with the initial stand-off distance is reported.

In all simulations, three levels of grid refinement are considered, which lead to the grid-independent results. Moreover, there is a minimum volume fraction α_{min} of each phase in the entire domain in the initial setups to ensure the hyperbolicity of the system. Moreover, the monotonized central slop limiter is used for the MUSCL reconstruction scheme, as explained in [146]. The time step is varying based on the CFL number which is set to 0.5. Moreover, it is assumed that the bubble contains only air; the initial interior pressure p_{air} is uniform, whereas in the pressure of the water surrounding the bubble follows the distribution described in [147]:

$$p_{water}(r) = p_f + \frac{R_0}{r}\left(p_{air} - p_f\right), \tag{45}$$

where p_f denotes the far-field pressure.

4.1.1 1D SHOCK TUBE

Shock tube problems serve as benchmark tests for the predictive capability of EoSs. Herein, a 3m pure water shock tube case has been considered as described in [82] . The diaphragm is placed at $x = 2$ m. Initially, the temperature is 300 K everywhere while $p = 10^9$ Pa in $x < 2$ m and $p = 10^5$ Pa in $x \geq 2$ m. The initial velocity is zero everywhere in the domain. The numerical discretization considers 1,000 cells, which has been found in prior studies to be

sufficient [146]. As it can be observed in Figure 4-1, the SG EoS results in a numerical temperature jump near the density discontinuity. It is also observed that the results obtained when using the MNASG EoS agree with those reported in [82]. The SG and the modified Tait EoSs result in the highest 16% and lowest 1% temperature overpredictions, respectively, compared to the most accurate IAPWS EoS. This is consistent with the findings as outlined in Chapter 2.2. It is further noticed that the developed modified Tait EoS has a limited valid range compared to the MNASG for the bubble collapse cases (initial pressure ratio of 180). This might be enhanced in the future by making more astute choices of functions in (18).

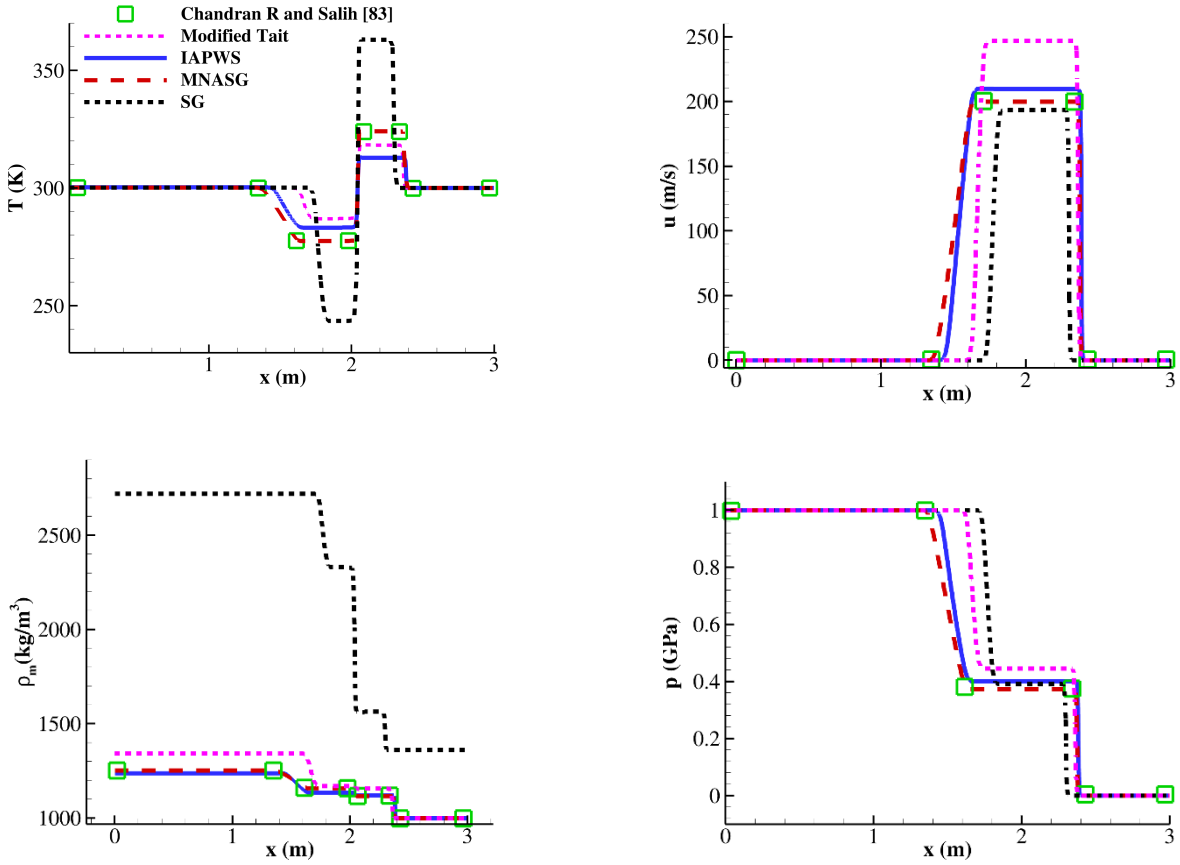

Figure 4-1. Water shock tube profile after 200 μs with various liquid EoSs for water compared with reference [82].

4.1.2 1D SPHERICAL BUBBLE COLLAPSE

The purpose of this test case is two-fold; firstly, to validate the solver against widely used bubble collapse cases and secondly, to compare the results against those reported in [90]. More specifically, an 1D spherical bubble with $R_0 = 1$ mm is forced to collapse under the influence of a pressure gradient. The case set up is as follows: $p_{air} = 1.01325 \times 10^5$ Pa, $\rho_{air} = 1.225\ \frac{Kg}{m^3}$, $p_f = 3.57589 \times 10^7$Pa, $\rho_{water} = 998.2\ \frac{Kg}{m^3}$ is set up. The domain length is $L_0 = 20$ mm and it has been discretised using 2,000 uniformly distributed cells. The plotted radius and time are presented dimensionlessly with R_0 and the Rayleigh collapse time, respectively:

$$R^* = \frac{r}{R_0}, \tag{46}$$

$$t^* = \frac{t}{0.915 R_0 \sqrt{\frac{\rho_{water}}{p_f}}}. \tag{47}$$

For comparison purposes, the RKPR and SG EoSs have been selected for the gas and liquid phases, respectively, similarly to our former study [90]. Figure 4-2a shows that excellent agreement between the present simulation against the corresponding results obtained with the Keller-Miksis model; in the latter, the IG EoS is used for the gas phase. This agreement is expected since it is known that the gas EoS has a minimal influence on the change of bubble radius during the collapse [90]. Moreover, the collapse dynamics and the space-averaged bubble temperature are identical to those reported in [90]; it is noted that this in study, a different diffused interface model known as the 'six-equation model' is used with the same equations of state, i.e., the pair of the RKPR and SG EoSs.

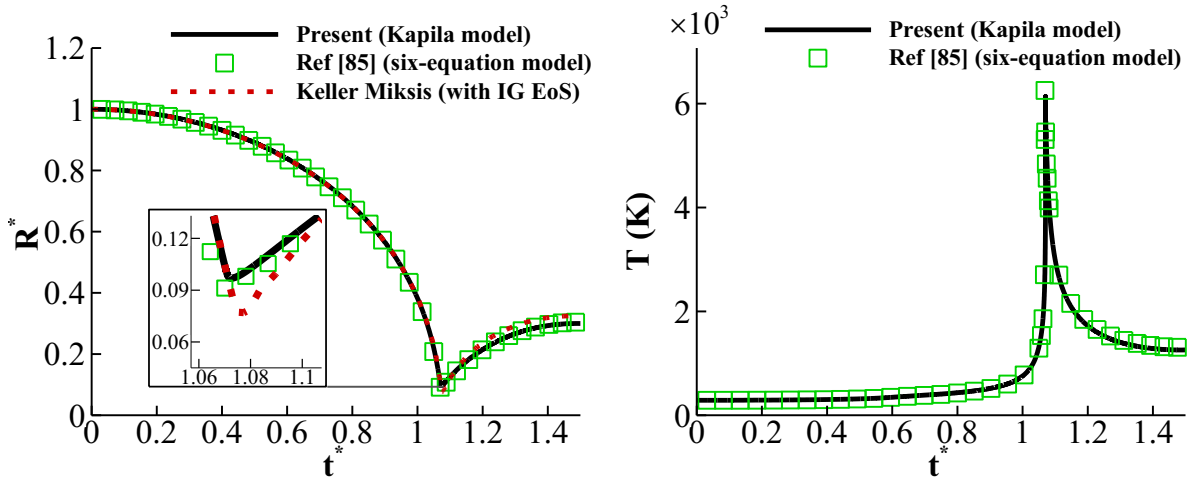

(a) (b)

Figure 4-2. Comparison of the bubble dynamics (a) and temperature (b) obtained with Kapila model in the present study to the ones with the six-equation model in [90].

Following presentation of the above benchmark cases, demonstration of the relative errors that can result from the SG EoS will be reported. In this regard, the initialization of the previous case is slightly modified by replacing the liquid density with its temperature and lowering the initial pressure ratio as shown in Table 4-1. This simulation is performed with RKPR EoS for the gas and with the SG, IAPWS, and MNASG EoSs for the liquid phase. Predictions for the temperature in the vicinity of the bubble interface are illustrated in Figure 4-3b. It is observed that the SG EoS results in up to 30% temperature overprediction compared to the IAPWS EoS, while the maximum overprediction from the MNASG EoS is below 6%. It is noteworthy to mention that the original version of the NASG EoS could not accurately depict the dynamics of the collapse.

Table 4-1. Initial conditions for the collapse case with real thermodynamics

p_{air} (Pa)	p_f (Pa)	$\rho_{air}\left(\frac{kg}{m^3}\right)$	T_{water} (K)
10^5	8.7×10^6	1.225	288

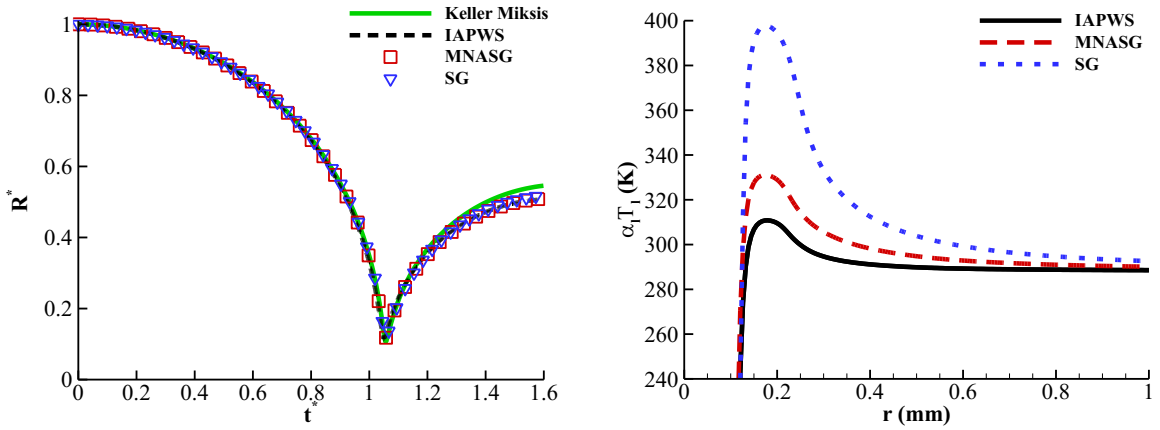

Figure 4-3. (a) Bubble dynamics and (b) water temperature predicted by the IAPWS and MNASG EoSs.

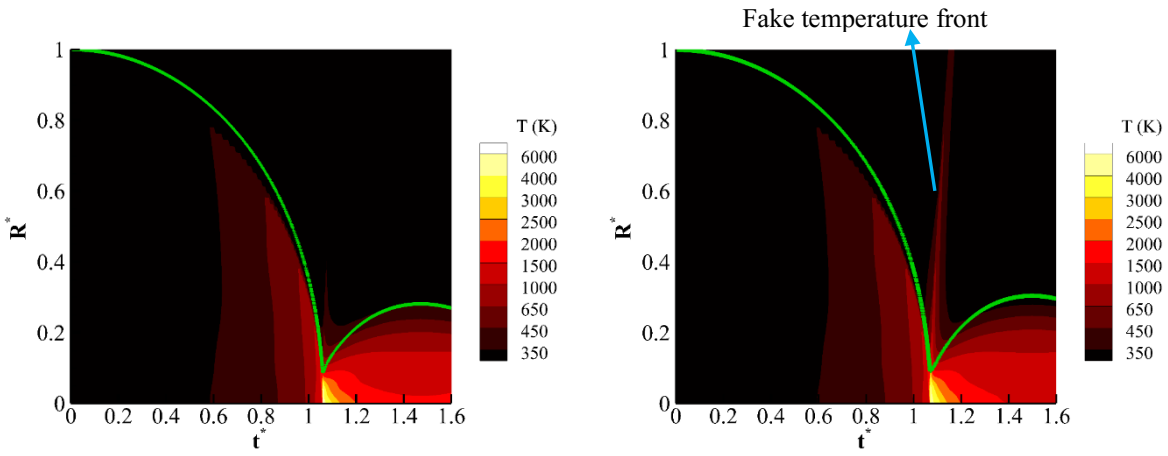

(a) (b)

Figure 4-4. Spatio-temporal change of the mixture temperature with RKPR EoS for air; and a) MNASG and b) SG EoS for water.

Since the IAPWS and the modified Tait fail at higher compressions, a stronger collapse with the initial $p_f = 3.57589 \times 10^7$Pa is simulated here using the MNASG and SG EoSs. The rest of initialization parameters are the same as in Table 4-1. It is noted again that the gas EoS is RKPR. The spatiotemporal change of the gas-liquid mixture temperature approximated by $T = Y_g T_g + Y_l T_l$ EoSs is plotted when using MNASG EoS in Figure 4-4a and SG EoS in Figure 4-4b. The occurrence of a fake temperature front is much more evident when the SG EoS with the maximum of ≈ 700 K while this is much less ≈ 450 K when using MNASG EoS. This indicates that the SG EoS overpredicts a travelling heat wave. It can be also observed that this temperature decreases over time after the collapse point and moves toward the far-field.

4.1.3 2D AXISYMMETRIC COLLAPSE

One of the diverse applications of ultrasound cavitation in biomedicine is shock wave lithotripsy (SWL). The mechanism of lithotripsy involves producing short, focused microsecond pulses that cause shockwave penetrating the body at a target site. During a treatment session, numerous pulses are administered, typically at frequencies ranging between 1 and 2 Hz. Cavitation is known to affect both the intended fragmentation of stones and the unintended harm to surrounding tissues [148]. While increasing the pulse rates could expedite the treatment process, it could also lead to tissue damage [148], [149].

A simplified representation for SWL can be examined as follows. A compressive shock front from the upper boundary demonstrated in Figure 4-5a represents the lithotripter pulse without the tensile part propagating in time; this is based on an analytical function described in [150] resembling that of an electrohydraulic lithotripter system Dornier HM3, which is a commonly used lithotripter. This test case was first introduced in the work of [150], where they studied the wall pressure subjected to the bubble collapse. In this setup, infinite impedance for the kidney stone is assumed to avoid any wave absorption in the boundary.

Initially, the pressure is atmospheric in the whole computational domain; the water and air densities are $\rho_{water} = 998.2\ kg/m^3$ and $\rho_{air} = 1.125\ kg/m^3$, respectively. To reduce the computational cost, the case is simulated in 2D axisymmetric coordinates instead of the full 3D configuration. The schematic of the geometry is presented in Figure 4-5b where the domain is divided into separate blocks while the grid is refined in the proximity of the liquid-air interface. Reflective boundary condition is used on the axis of symmetry whereas for the right side and the bottom wall, the non-reflective and no-slip boundary conditions have been used, respectively. The bubble has an initial radius of $R_0 = 0.05$ mm while the initial stand-off distance, defined as the minimum distance between the bubble center and the wall, is $H_0 = 2R_0$.

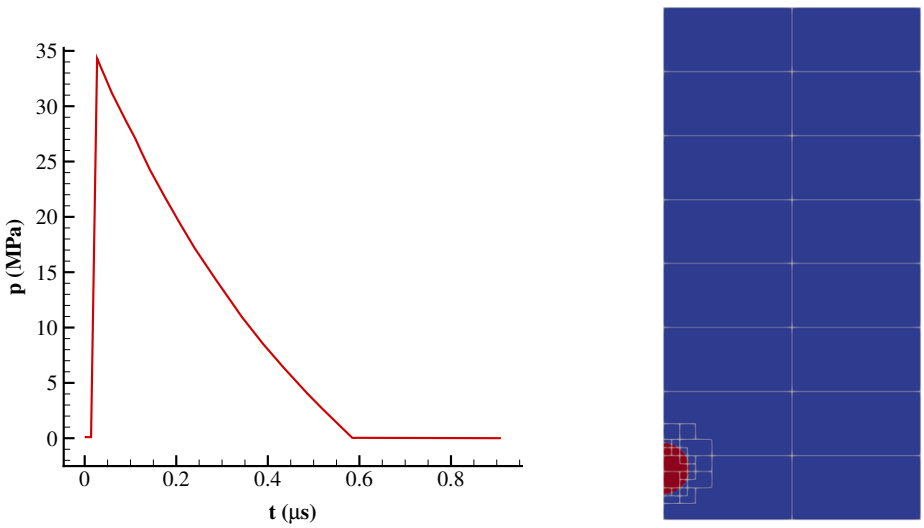

(a) (b)

Figure 4-5. (a) Pressure pulse of the lithotripter and (b) Schematic of the initial setup for the non-spherical collapse case with block structured grid in AMReX.

The temporal variation of the bubble volume is initially presented in Figure 4-6. To be consistent with the results reported in [150], the bubble volume is normalized with its initial value $V^* = V/V_0$ and the time is non-dimensional using $t^* = tc_L/R_0$. In this case, $c_L = 1{,}647\ m/s$ is the reference speed of sound. The results obtained with the ideal and real gas EoSs are compared with the study of [150]; overall, good agreement is achieved, as expected.

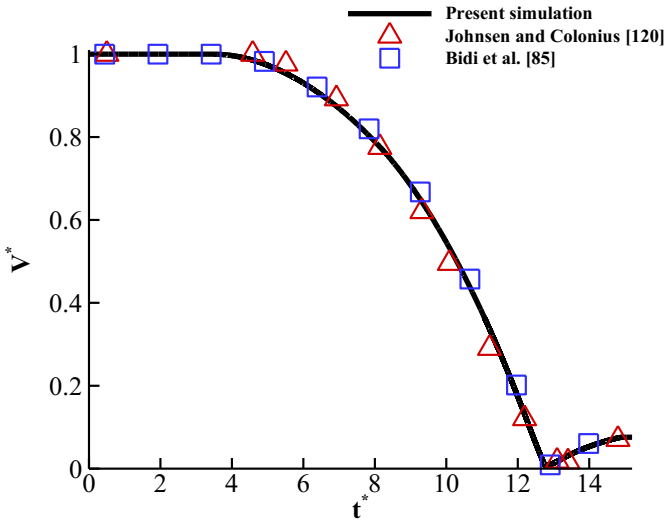

Figure 4-6. Bubble dynamics of shock-induced collapsing bubble using RKPR and MNASG EoSs compared with [90], [150].

Further details of the collapse process are illustrated in the following plots. More specifically, the relevant pressure and numerical Schlieren contours are demonstrated in Figure 4-7 at different times during the collapse. For these simulations, the MNASG has been utilized as it was found in the previous section to predict the liquid temperature more accurately. In this context, the liquid temperature distribution along the wall is illustrated in Figure 4-8a. It can be seen that temperature remains relatively stable and does not experience substantial change before the final stage of the collapse. At this point, an increase of 25 K of the liquid is predicted at the time when the shock wave hits the wall. A similar pattern can be observed for pressure in Figure 4-8b where the wall pressure exceeds 0.4 GPa.

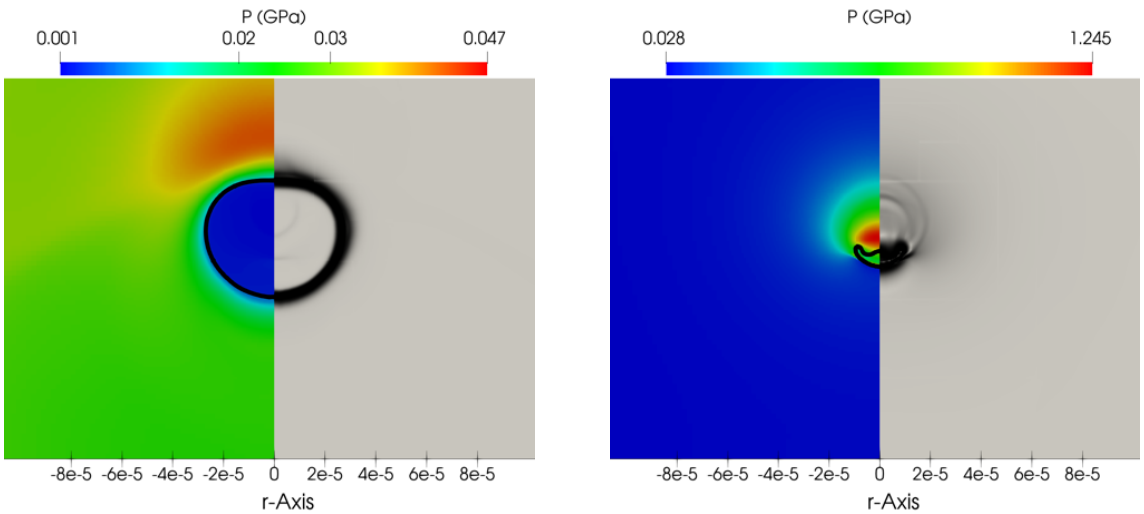

(a) (b)

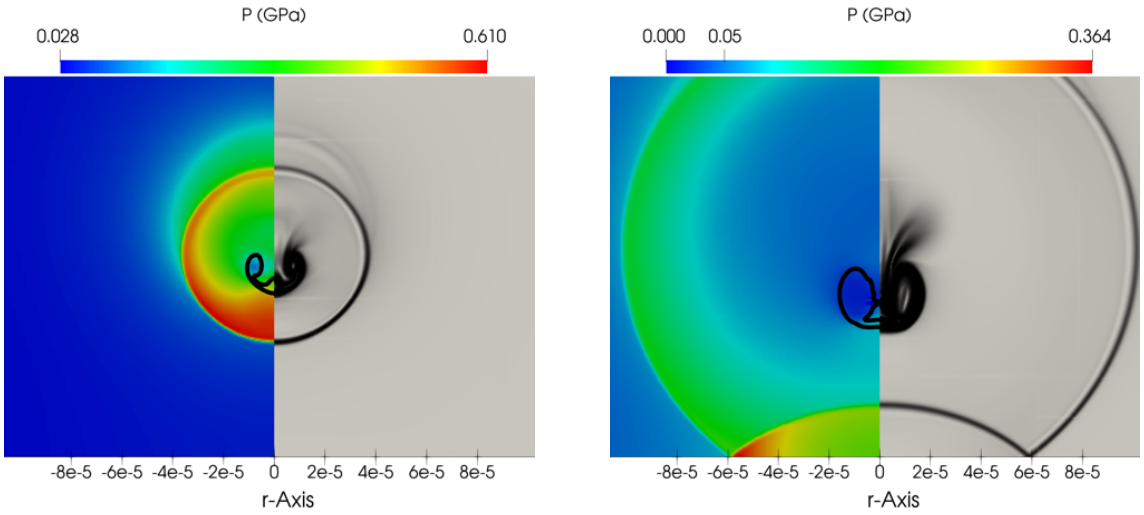

(c) (d)

Figure 4-7. Pressure field (left half), numerical Schlieren (right half) at different collapse stages: a) $t^* = 11.50$, b) $t^* = 12.65$, c) $t^* = 13.07$, and d) $t^* = 14.41$.

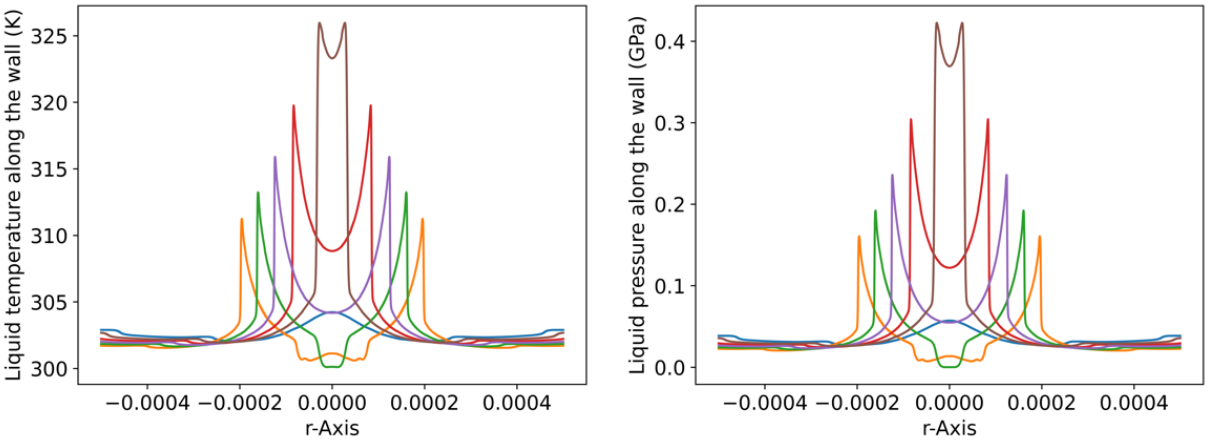

(a) (b)

Figure 4-8. Liquid temperature (a) and pressure (b) along the wall at different times after the shock hits the wall.

In order to gain a deeper insight into the dynamic evolution of liquid temperature, temperature contours are presented in Figure 4-9; the plotted temperature values are masked to values up to the maximum value in the liquid phase (thus, the much higher temperatures inside

the bubble appear as empty). On the right-hand side of the same plots, the contours depicting the magnitude of the velocity field are plotted.

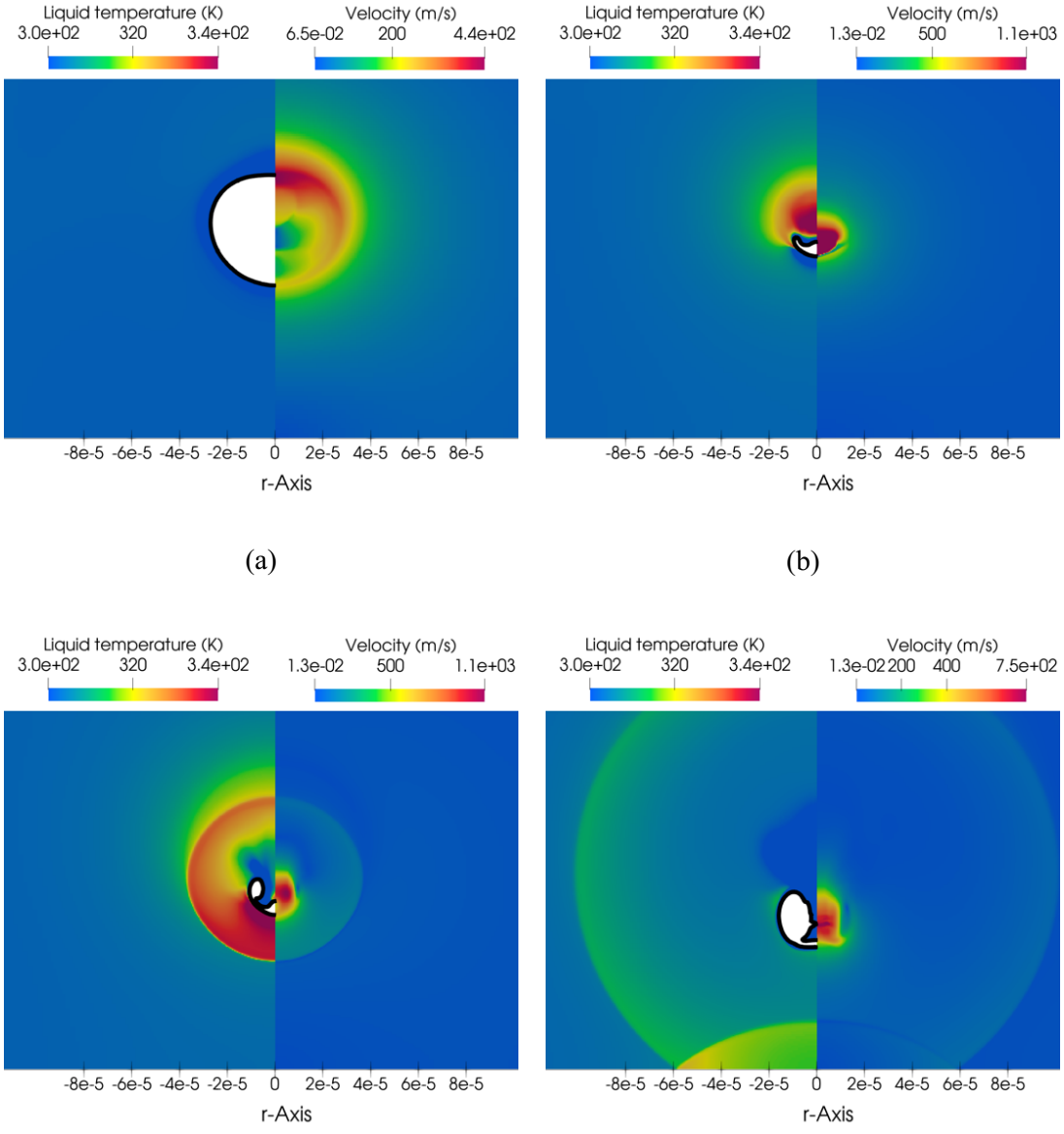

Figure 4-9. Liquid temperature (left side) and velocity magnitude (right side) at different collapse stages.

According to Figure 4-9b it becomes apparent that the liquid temperature can rise significantly to 340 K in the region above the bubble before the collapse. During the rebound, this region cools down while the liquid temperature in the proximity of the bubble is still high, as shown in Figure 4-9c. Subsequently, the shock propagates towards the wall where the liquid

temperature along the wall increases to 340 K, as demonstrated in Figure 4-9d. Evidently, the shock wave causes this heating rather than the propagation of the pressure pulse of the lithotripter. To further elaborate on this observation, the impact of the initial bubble stand-off distance from the wall on the subsequent rise of liquid temperature have been studied, using various initial stand-off distances. Figure 4-10 demonstrates the temporal evolution of the space-averaged liquid temperature and pressure within the region $r < R_0$. As depicted in this figure, a decrease in the initial stand-off distance results in an increase in both the liquid temperature along the wall and the pressure, consistent with the observations reported in [83].

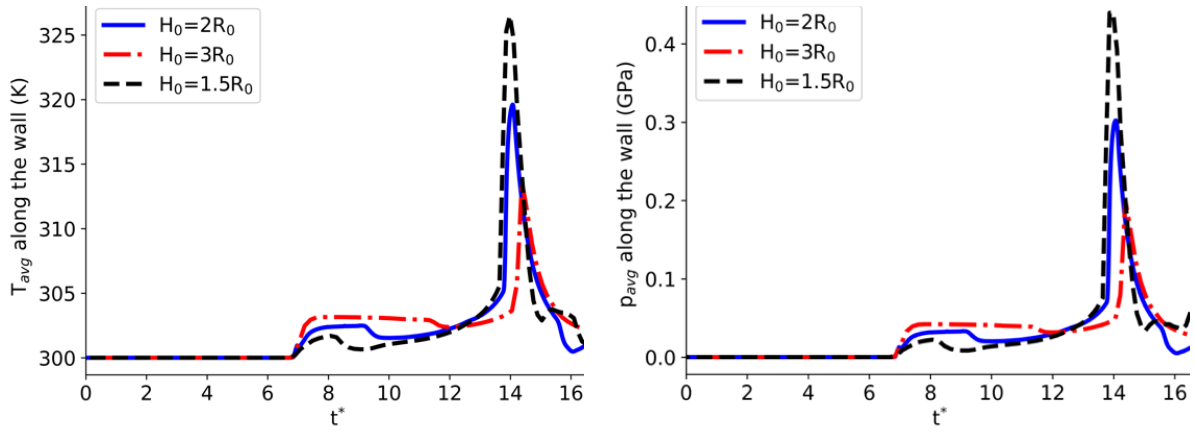

(a) (b)

Figure 4-10. Spaced-averaged (in $r < R_0$) liquid temperature (a) and pressure (b) along the wall over time.

Lastly, the heatmap of the temporal change of the liquid temperature along the rigid wall is depicted in Figure 4-11 where the horizontal axis shows the time while the vertical axis represents the rigid wall axis. Accordingly, it is observed that the temperature increase due to the pressure pulse is not significant. However, as the bubble collapses, the maximum temperature raise to $T = 325$ K below the bubble in $r \approx (0,0.02)$ mm while tissue damage occurs usually above 325 K [151]. Over the course of time, the region exhibiting the highest temperature gradually migrates towards the right boundary, with a reduction in its magnitude.

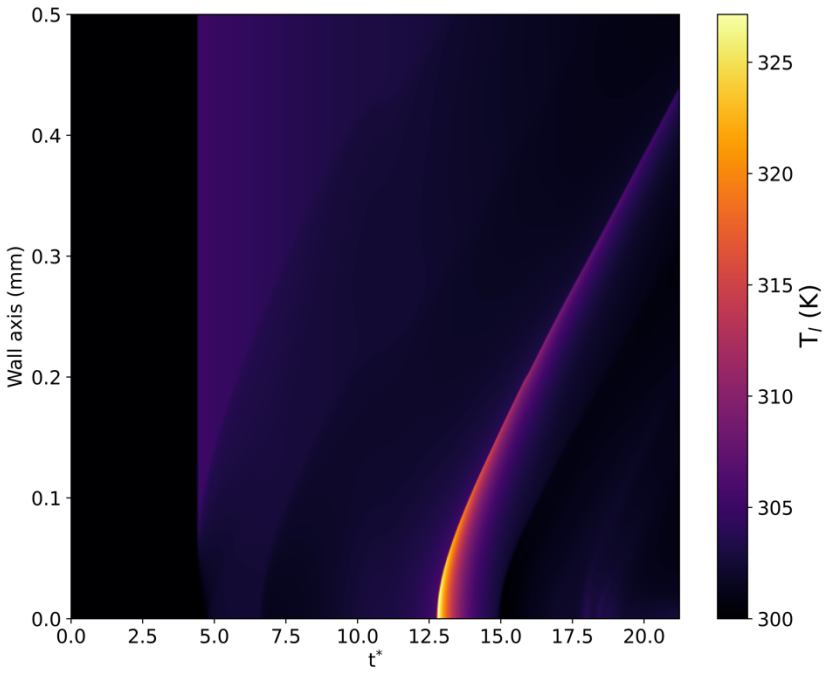

Figure 4-11. Spatio-temporal change of the liquid temperature along the wall axis.

4.2 SUMMARY

In the current study, we expand the Kapila model to incorporate complex EoSs for both the liquid and gas phases. Since real gas effects during bubble collapses were extensively discussed in our former work, the present work has focused on the thermal effects induced in the liquid phase. Particularly, the deficiencies of EoS for the liquid state ought to both the unphysical specific heat ratio and the absence of terms considering repulsive molecular effects was showcased. It was observed that the SG EoS leads to above 800% error in temperature rise compared to the prediction obtained with the IAPWS one, at the highest compression of 10 GPa investigated. Moreover, the more complex and accurate modified Tait and IAPWS EoS were able to resolve and eliminate the spurious liquid temperature front that is predicted when the SG EoS was used, and which can be as high as 400 K. Having demonstrated the ability of the proposed liquid EoS to predict the temperature variation for the benchmark bubble collapse cases, the liquid temperature developing along a solid wall exposed to the violent bubble collapse induced by an ultrasonic pressure pulse simulating that of a commercial lithotripter

was studied. Model predictions indicated that the temperature increase during a single collapse event is a function of the bubble initial stand-off distance; shorter initial stand-off distance led to higher liquid temperatures along the wall.

5 INVESTIGATION OF TEMPERATURES PRODUCED DURING ULTRASOUND-DRIVEN COLLAPSE OF AIR BUBBLES NEAR SOFT MATERIALS

5.1 RESULTS AND DISCUSSION

In this section, the temperatures produced during the ultrasound-driven collapse of an air bubble are presented. Moreover, the effect of the initial bubble radius and standoff distance on soft-material heating is also presented.

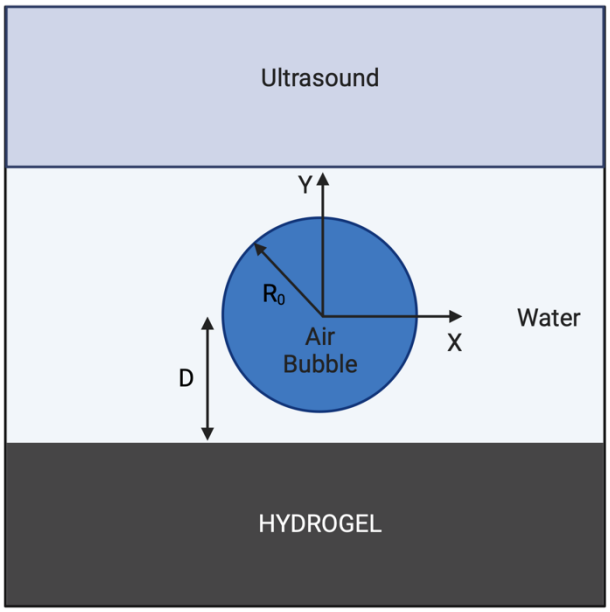

Figure 5-1. Problem set-up of an ultrasound-induced collapse of an air bubble near a soft material.

The schematic of the case is presented in Figure 5-1 where a lithotripter pulse impacts an air bubble of initial radius R_0 standing at a distance D from a soft material. The computational domain spans $L_x = 10R_0$ and $L_y = 20R_0$ where $R_0 = 50$ μm. To save computational time, the simulations were conducted using an axisymmetric formulation with $\beta = 1$. The base mesh of $N_x = 256$ and $N_y = 512$ cells is used, resulting in 131,072 initial cells prior to refinement; the corresponding mesh spacing is $\Delta x = 1.953125 \cdot 10^{-3}$ mm. Two levels of maximum refinement have been used. The top boundary is used to propagate the lithotripter pulse while an outflow boundary condition is imposed on the right and lower boundaries; the left boundary is the axis of symmetry. A CFL number of 0.1 was imposed to preserve the explicit scheme's numerical stability. Initially, the bubble is at mechanical equilibrium with its surrounding at atmospheric pressure and at a temperature of $T_0 = 300K$. The air phase is modeled by using the RKPRe table with an initial density $\rho_{air} = 1.177\ kg \cdot m^{-3}$. A description of the RKPRe

EoS can be found in [152]. The water phase is modeled by using the MNASG EoS with the coefficients listed in Table 5-1 and an initial density $\rho_{water} = 998.2\ kg \cdot m^{-3}$. Similarly, a description of the MNASG EoS can be found in [82].The soft material is representative of agarose tissue phantoms [153] with an initial density of $\rho_{sm} = 1010\ kg \cdot m^{-3}$ and a shear modulus $\mu = 7.23 \cdot 10^3$ Pa. The 1% agarose tissue phantom chosen has 98.1% water content [153]. Since the water content is so high it is assumed that the tissue phantom thermodynamic coefficients are that of water.

Table 5-1. MNASG [82] coefficients for liquid water

$c_v(J.(kg.K)^{-1})$	γ	$p_\infty(Pa)$	$b(m^3.kg^{-1})$	$q(J.kg^{-1})$
3610	1.19	$6217.8 \cdot 10^5$	$6.7212 \cdot 10^{-4}$	-1177788

In Figure 5-2, the ultrasound-induced collapse of an air bubble of $R_0 = 50\ \mu m$ with an initial stand-off $D/R_0 = 1.1$ near a soft material at different timesteps is presented. The contours of temperature, pressure, and maximum principal stress are shown. In the first frame Figure 5-2a, the ultrasound pulse is traveling downstream towards the bubble. After the ultrasound pulse has impacted the bubble, a rarefaction wave is emitted from the bubble interface. In Figure 5-2b, the bubble has started to collapse; the adverse pressure gradient is clearly visible. The sink flow under the bubble has stretched the tissue, applying tensile stresses in the process. The temperature is seen to increase in a small region at the distal side of the bubble. The collapse process continues as seen in Figure 5-2c-d where the distal side of the bubble has left an elevated temperature in its wake. The tissue continues to be pulled towards the bubble. Later, in Figure 5-2e the liquid jet penetrated the bubble leading to toroidal bubble formation, and the water hammer shock emitted. To better visualize the shock waves numerical schlieren were plotted in Figure 5-3 based on the following formula [143]:

$$\phi = \exp\left(-\frac{k|\Delta\rho|}{max|\Delta\rho|}\right), \quad (48)$$

where k is a scaling parameter to improve the visibility of the waves, here equal to 200. The precursor and water hammer shocks can be seen in Figure 5-3d. The temperature is noticeably higher downstream of the toroidal bubble. The gas content of the bubble is heated by compression during collapse. The temperature inside the bubble is shown in Figure 5-4c. The

high-temperature filament seen in Figure 5-2e is an air-water mixture region with heated air. The bubble starts the rebound process in Figure 5-2f and the liquid jet penetrates the tissue. The temperature increases along the spherically propagating shock. The bubble continues its downward moving motion in Figure 5-2g. The liquid jet is now compressing the tissue at the impact point. The temperature also increases on the distal side of the toroidal bubble where an air-water mixture is present. The same observations were made in [154]. In Figure 5-2h, the heated filament impacts the surface of the soft material although its maximum temperature has significantly cooled down between Figure 5-2e-h.

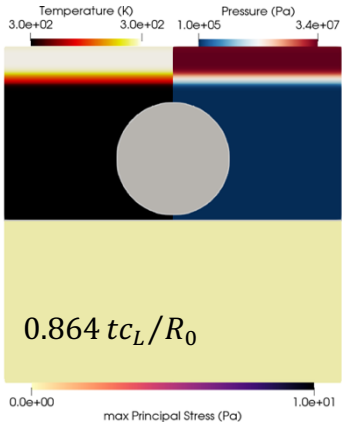

(a)

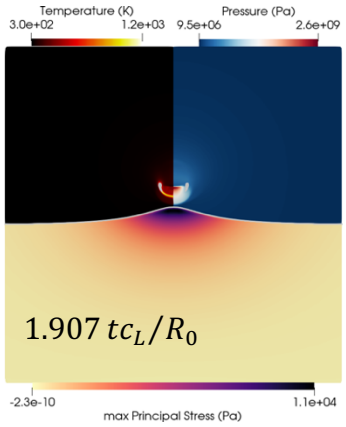

(e)

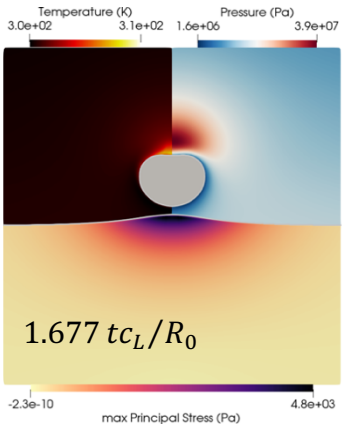

(b)

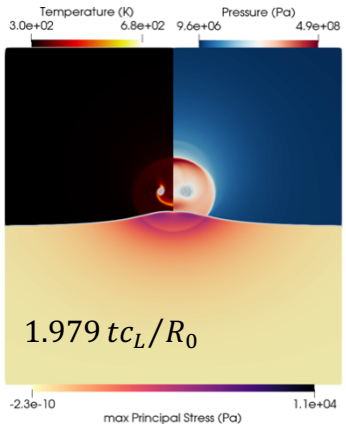

(f)

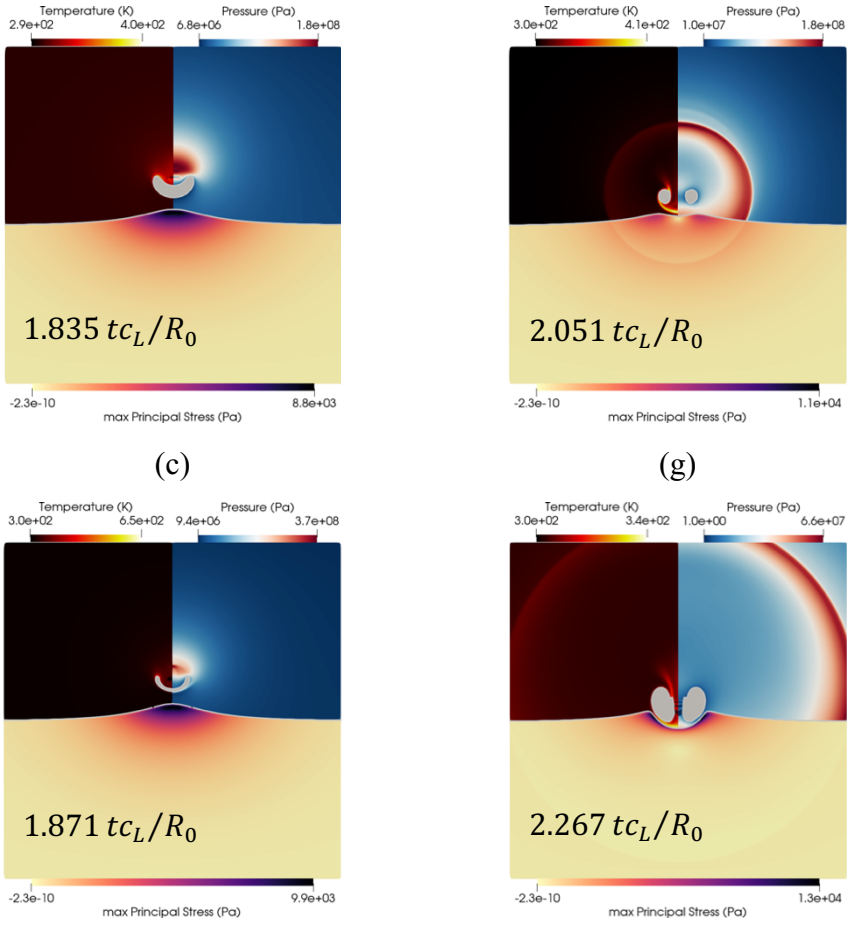

Figure 5-2. The ultrasound-induced collapse of an air bubble of $R_0 = 50\ \mu m$ with an initial stand-off $D/R_0 = 1.1$ near a soft material at different timesteps. The grey isosurface separates the different materials and is defined by $\alpha_k = 0.5$. The bubble interior has also been greyed out. Upper left hand: contour of temperature. Upper right hand: contour of pressure. Bottom half: contour of the maximum principal stress.

The temporal evolution of the normalized air volume, space-averaged surface and bubble temperature are shown in Figure 5-4. The space-averaged surface temperature is computed by the arithmetic average of the cells whose coordinates are $x < R_0$ on the volume fraction isosurface. This surface temperature is seen to increase three times as illustrated in Figure 5-4b. First, the lithotripter pulse is responsible for sightly heating the soft material to about $\sim 300.7K$; also visible in Figure 5-5a where the pulse has already propagated, and in Figure 5-4b (b1). Second, the largest heating is caused by the bubble's collapse as depicted in Figure 5-5a-b and in Figure 5-4b (b2). The heating of about $\sim 15K$ experienced by the soft material is due to the shock emitted by the collapsing bubble as shown in Figure 5-5b. Third, the heated filament deposits heat onto the soft material albeit less than a kelvin as illustrated in

Figure 5-5d and Figure 5-4b (b3). The space-averaged surface temperature then cools down slowly.

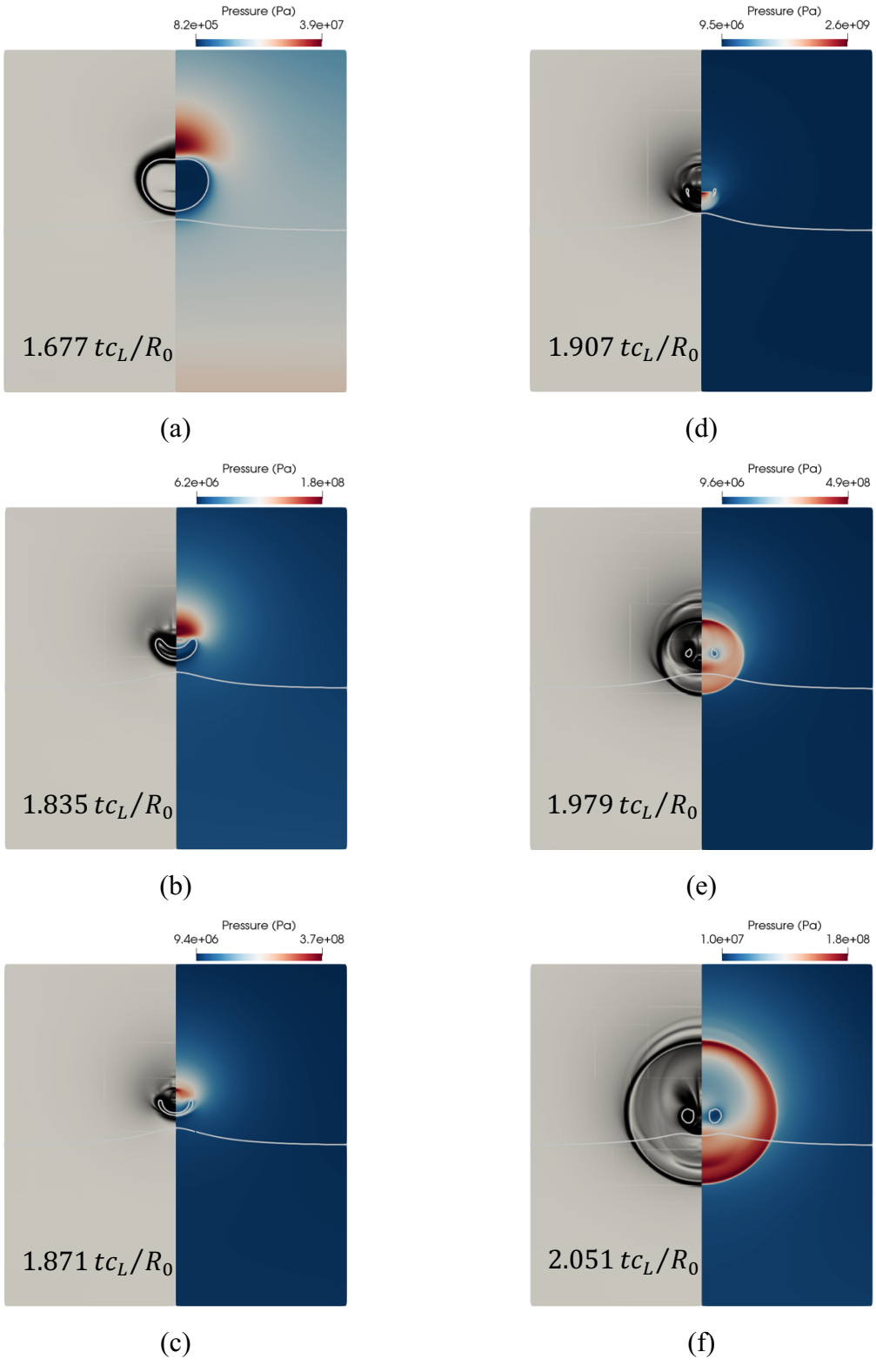

Figure 5-3. The ultrasound-induced collapse of an air bubble of $R_0 = 50\ \mu m$ with an initial stand-off $D/R_0 = 1.1$ near a soft material at different timesteps. The grey isosurface separates the different materials and is defined by $\alpha_k = 0.5$. Left: numerical schlieren. Right: contour of pressure.

For a clearer view of the evolution of the temperature along the soft material isosurface, its spatiotemporal map is plotted in Figure 5-6. The highest temperature is reached under the bubble for $x < 2R_0$ right after collapse where $T > 340K$. The shock wave emitted by the bubble's collapse is then seen to rapidly propagate outward while cooling down. The soft material's surface cools down far from the bubble while it heats up again close to the bubble due to the heat deposition of the air-water mixture. As seen in Figure 5-4b after (b3) the temperature slowly cools down but stays above $300K$.

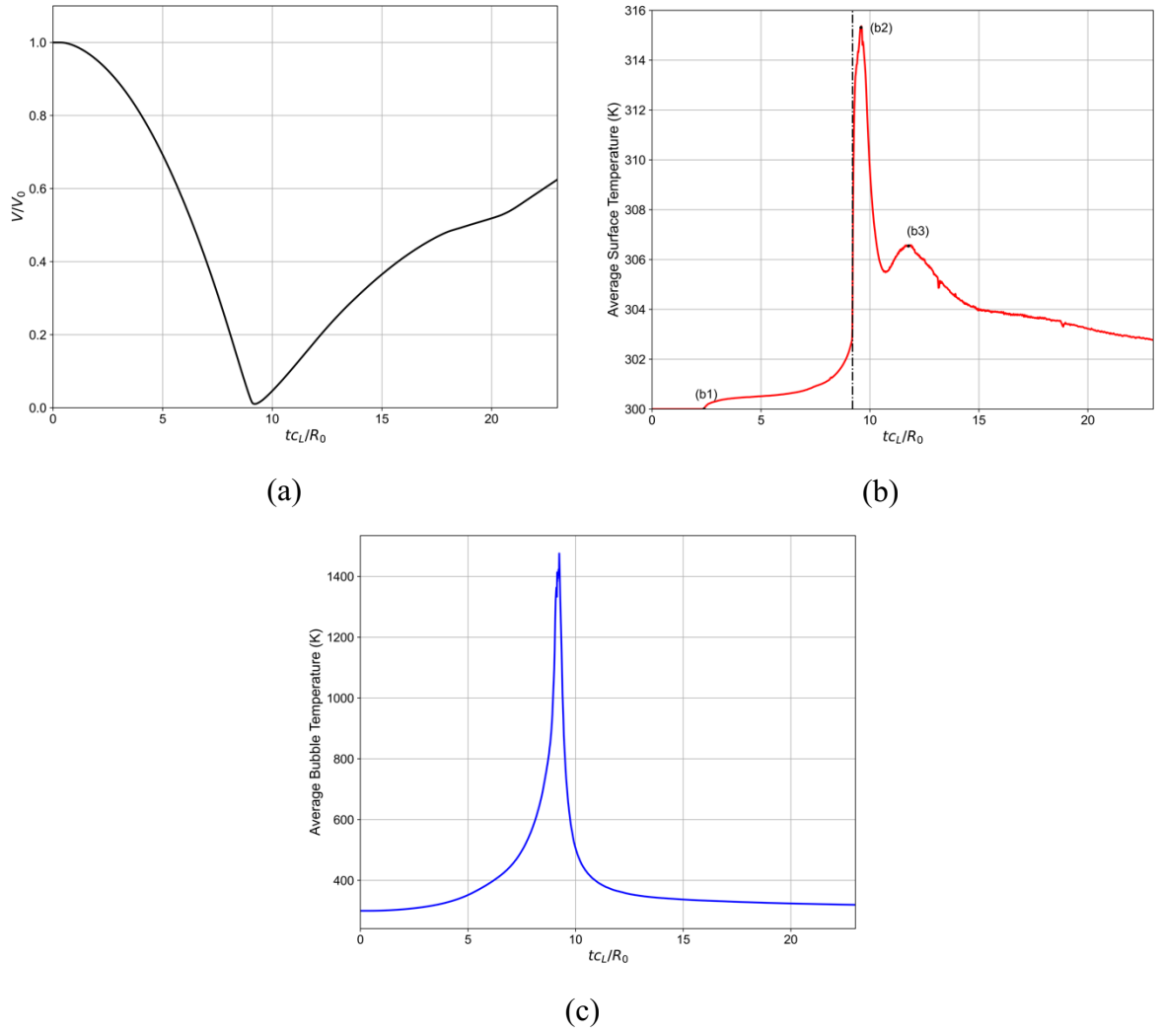

Figure 5-4. The ultrasound-induced collapse of an air bubble of $R_0 = 50\ \mu m$ with an initial stand-off $D/R_0 = 1.1$ near a soft material. The dash-dotted line represents the collapse time. (a) Temporal

evolution of the normalized air volume. (b) Temporal evolution of the space-averaged surface temperature. (c) Temporal evolution of the space-averaged bubble temperature.

To sum up, three heating mechanisms are identified. The propagation of the ultrasound pulse is responsible for the first heating observed. The shock emitted by the bubble's collapse induces the highest temperature in the soft material albeit it cools down rapidly. Lastly, the contact with the air-water mixture filament referred to here as bubble-material contact is responsible for a slight increase in temperature over a prolonged duration.

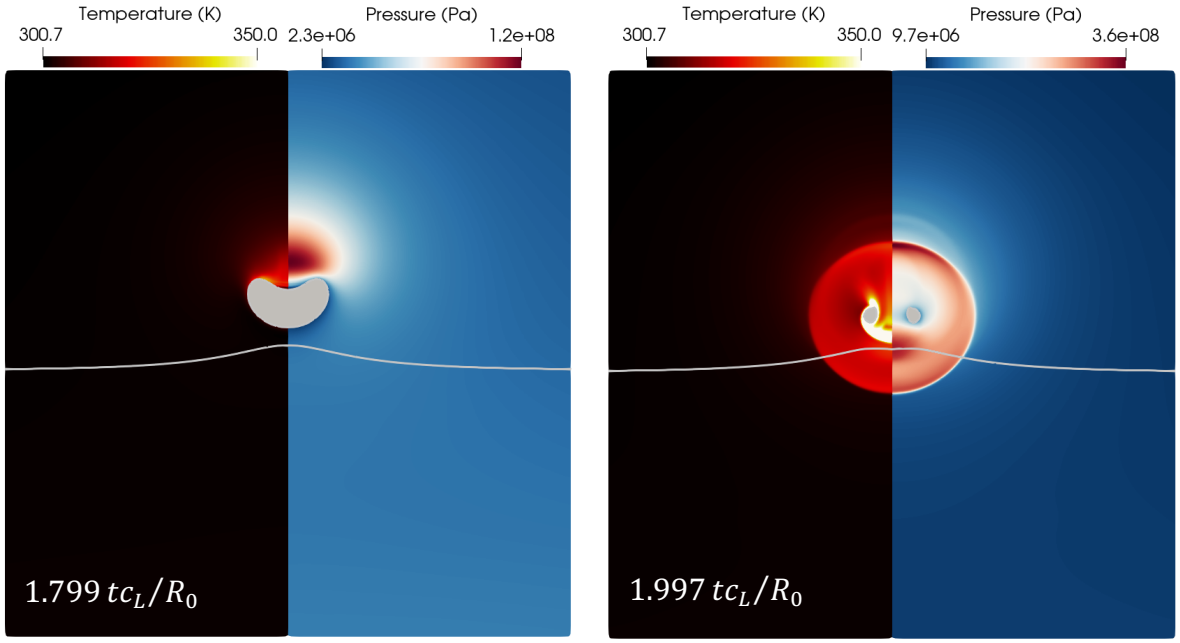

(a) (c)

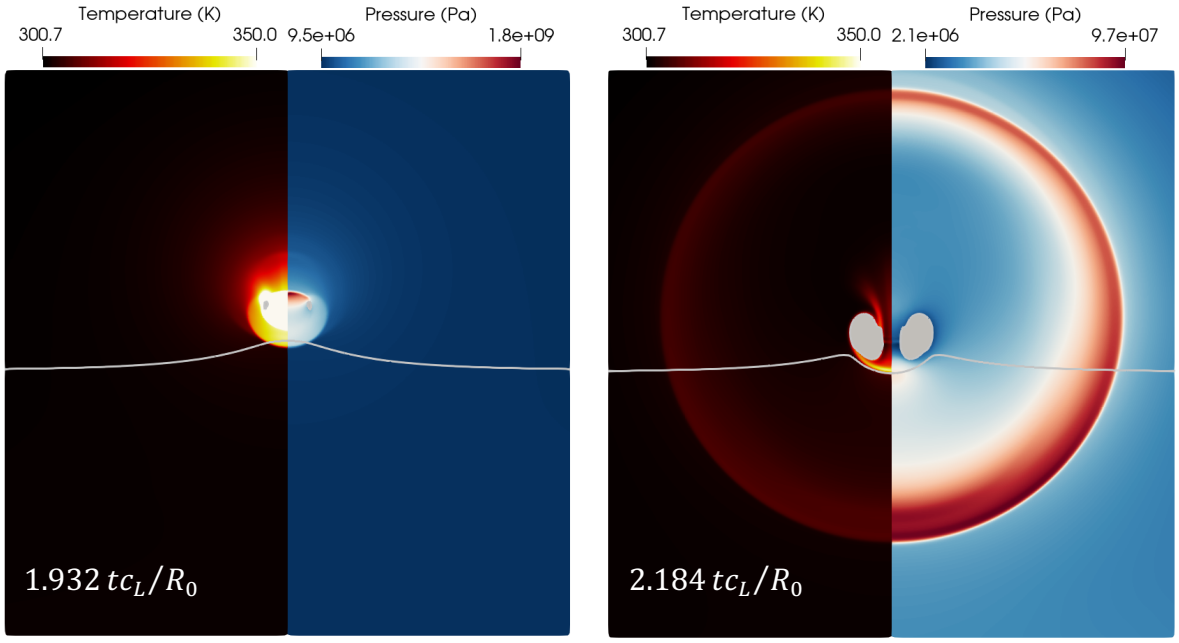

(b) (d)

Figure 5-5. The ultrasound-induced collapse of an air bubble of $R_0 = 50\ \mu m$ with an initial stand-off $D/R_0 = 1.1$ near a soft material at different timesteps. The grey isosurface separates the different materials and is defined by $\alpha_k = 0.5$. The bubble interior has also been greyed out. Left: contour of temperature. Right: contour of pressure.

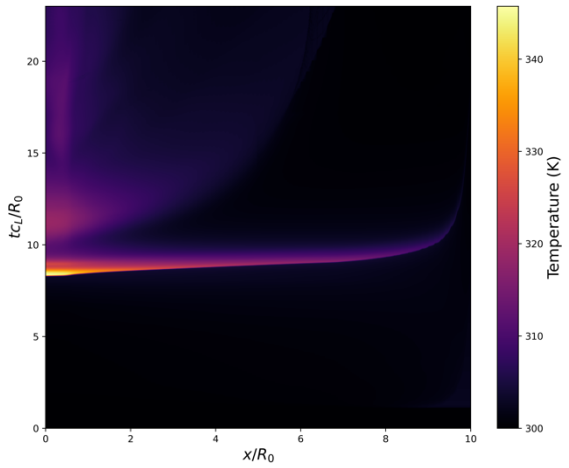

Figure 5-6. Spatiotemporal map of the temperature on the isosurface of the volume fraction defined by $\alpha_k = 0.5$.

5.1.1 EFFECT OF THE BUBBLE RADIUS

In this section, the effect of the initial bubble radius on the soft material's heating is investigated. In Figure 5-7, the effect of the initial bubble radius for a standoff distance $S_d = 1.1$ and three bubble radii $R_0 = 25, 50, 100\mu m$ is presented.

Figure 5-7a shows the spatiotemporal map of the temperature on the isosurface of the volume fraction defined by $\alpha_k = 0.5$ for the three bubble radii. Clearly, the maximum temperature near the center reached post-collapse is higher for the smaller bubbles, i.e.: $T^{max}_{R_0=25} > T^{max}_{R_0=50} > T^{max}_{R_0=100}$. Similarly, since the shock is stronger for the smaller bubbles the temperature cools down less as it propagates outward. Moreover, the heating induced by the bubble's contact with the soft material is distinctly more significant as the bubble radius decreases. The weaker compression experienced by the bigger bubbles translates to a lower gas temperature during the collapse, and thus clearly lower temperatures during bubble-material contact.

Figure 5-7b shows the temporal evolution of the space-averaged surface temperature for the three bubble radii. The previously discussed heating mechanisms are again visible, namely: the ultrasound, the shock emitted by the bubble collapse, and the bubble contact. The higher temperature produced by the smaller bubbles is also distinctly observed.

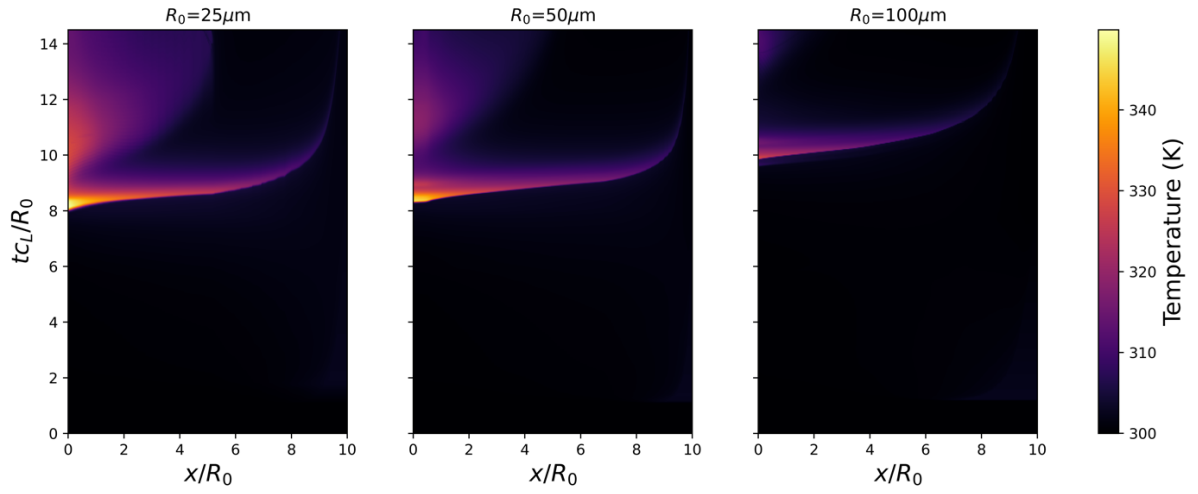

(a)

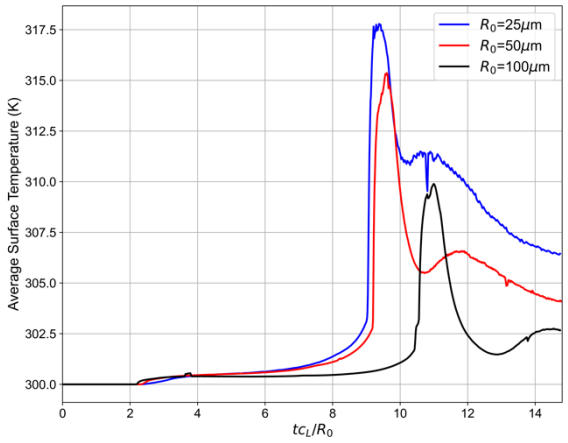

(b)

Figure 5-7. Effect of the initial bubble radius for a standoff distance $S_d = 1.1$ and three bubble radii $R_0 = 25, 50, 100\mu m$. (a) Spatiotemporal map of the temperature on the isosurface of the volume fraction defined by $\alpha_k = 0.5$ for the three bubble radii (b) Temporal evolution of the space-averaged surface temperature for the three bubble radii.

5.1.2 EFFECT OF THE STAND-OFF DISTANCE

In this section, the effect of the standoff distance on the soft material's heating is investigated. In Figure 5-8, the effect of the standoff distance for an initial bubble radius $R_0 = 25\mu m$ and three standoff distances $S_d = 1.1, 2.0, 3.0$ is presented.

Figure 5-8a shows the spatiotemporal map of the temperature on the isosurface of the volume fraction defined by $\alpha_k = 0.5$ for the three standoff distances. First, as the standoff distance increases the maximum temperature along the soft material surface decreases significantly. Second, since the bubble is further away for higher standoff distances the heating due to the bubble's contact is not observed. Indeed, by the time the bubble's centroid moves downstream toward the soft material, the bubble has already cooled down.

Figure 5-8b shows the temporal evolution of the space-averaged surface temperature for the three standoff distances. The first notable observation is the difference in temperature due to the ultrasound heating. For lower standoff distances the bubble is closer to the soft material and provides a shielding effect. Moreover, the peak temperatures observed are to decrease as the standoff distance increases. Indeed, since the bubble is further away; the shock emitted by the bubble's collapse loses amplitude inversely proportional to the distance traveled. Lastly, the same observation as in Figure 5-8a is made where no heating due to bubble contact is observed for higher standoff distances.

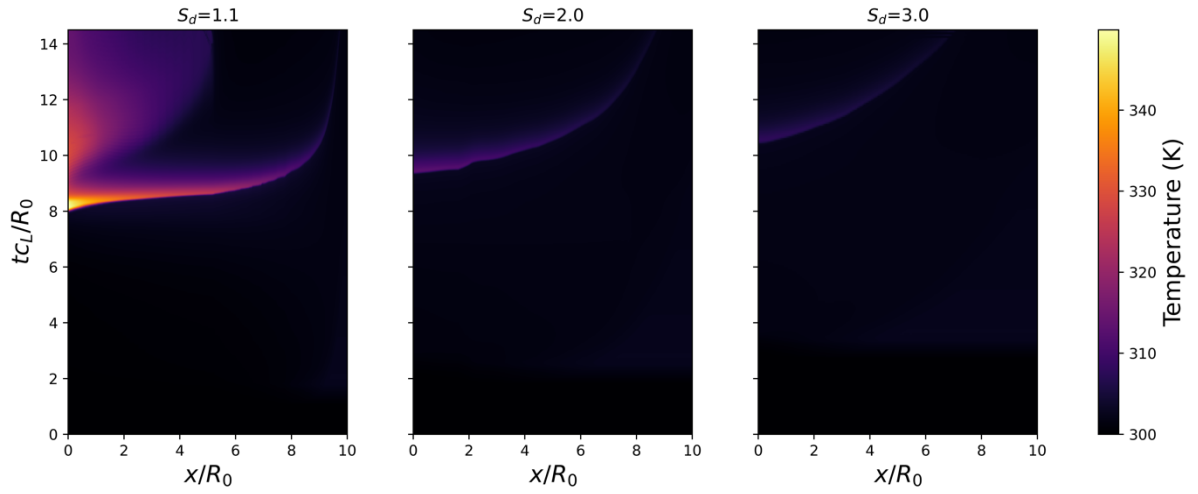

(a)

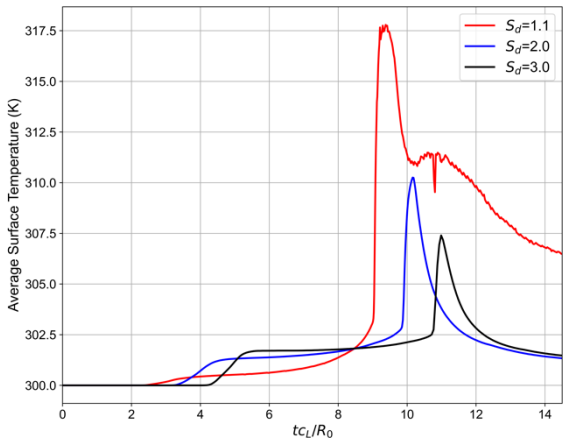

(b)

Figure 5-8. Effect of the standoff distance for an initial bubble radius $R_0 = 25\mu m$ and three standoff distances $S_d = 1.1, 2.0, 3.0$. (a) Spatiotemporal map of the temperature on the isosurface of the volume fraction defined by $\alpha_k = 0.5$ for the three standoff distances (b) Temporal evolution of the space-averaged surface temperature for the three standoff distances.

5.2 SUMMARY

A numerical investigation of the temperature effects in ultrasound-induced collapse of air bubbles near soft materials was presented using a multi-material DIM model with AMR extended to include complex thermodynamics. The RKPR EoS is used in tabulated format for the gas while the MNASG EoS is used in parametric form for liquid water. To have a better understanding of the soft material's heating, the effect of the initial bubble radius and the standoff distance were investigated. Insights into the thermal damage mechanisms were presented through the visualization of the temperature contours and the spatiotemporal temperature maps on the soft material's surface.

Our findings reveal that three heating mechanisms are present. Firstly, the ultrasound propagating inside the soft material. Secondly, the shock emitted by the bubble's collapse which is the mechanism that produces the highest temperature although momentary. Thirdly, after the bubble collapses, it migrates toward the soft material and makes contact heating it up in the process. However, the bubble contact mechanism becomes less important as the standoff distance increases since the gas has time to cool down while moving downstream. Meanwhile, the heating experienced by the shock emitted at the bubble's collapse is observable at all

standoff distances although greatly diminished. Furthermore, our analysis showed that smaller bubbles produce higher temperatures, especially upon collapse, and significantly enhance heating when in contact with the soft material.

This investigation underscores the intricate dynamics involved in the ultrasound-induced collapse of air bubbles and their implications for soft material heating, paving the way for improvements in related medical applications.

6 CONCLUSIONS AND RECOMMENDATIONS FOR FUTURE WORK

In this thesis, a novel compressible multi-material DIM with block-structured AMR is presented. The novel multi-material DIM can be used to model any arbitrary number of materials: fluids and solids. A local time-stepping is used along with the block-structured AMR to advance the hierarchical levels, making its implementation extremely efficient computationally despite the number of equations to solve. The waves and interfaces remain sharp thanks to the use of the tagging criterion based on the density gradient. Later, it is expanded to real-fluid EoSs where each material can be modelled with its own tabulated or parametric EoS using a newton-based algorithm to compute the mixture pressure. A series of stringent benchmark cases are used to validate the proposed model and are found to be in excellent agreement.

Firstly, the presented multi-material DIM was utilized to investigate the ultrasound-induced collapse of air bubbles near soft materials. The analysis shows that tissues are predominately experiences tensile forces as opposed to compressive or shear forces, suggesting a mechanism of tension-induced injuries. Additionally, the bubble radius is a key factor of the stresses developed in the soft material, highlighting its significance in medical procedures. Although changes in shear modulus have a minimal affect the bubble's early dynamics, it significantly changes the penetration dynamics and deformations in the later stages. The areas where the maximum principal stress is highest are identified suggesting potential locations of tension-driven mechanical damage.

Secondly, the importance of real-fluid EoSs in predicting accurate temperatures is demonstrated. Indeed, the lack of accuracy of common EoSs like the SG EoS in predicting temperature is clearly shown when compared to the IAPWS, the Modified Tait or the MNASG EoSs. The proposed methodology to include real-fluid EoS into the Kapila DIM is then used to examine a lithotripter pulse induced collapse of an air bubble near a rigid wall. The results show significant temperature elevation on the rigid wall after bubble collapse. More specifically, an increase of 25K was recorded along the wall. The standoff distance also played a significant role in the maximum temperature observed on the rigid wall. In fact, smaller standoff distances between the bubble and the rigid wall produced higher temperatures.

Thirdly, real-fluid EoSs are incorporated into the multi-material DIM by using a newton-based method to compute the mixture pressure. Each material is described by its own real-fluids EoS in tabulated or parametric form. The RKPR and the MNASG EoSs are used to investigate the temperatures observed in ultrasound-driven bubble collapse near a soft material. The results reveal three heating mechanism: the ultrasound propagating, the emitted shock from the bubble's collapse and bubble contact on the soft material. The significance of bubble contact diminishes with greater standoff distances due to gas cooling, while the initial shock-induced heating is less affected by distance because of the spherical nature of the shock emitted. Additionally, smaller bubbles with the same ultrasound amplitude are found to cause higher temperatures on collapse and greater heating upon contact with the material due to a more violent collapse.

These investigations underscore the intricate dynamics involved in the ultrasound-induced collapse of air bubbles near soft materials and their implications for soft material damage and heating, paving the way for improvements both in numerical modelling and in related medical applications.

6.1 RECOMMENDATIONS FOR FUTURE WORK

The multi-material DIM introduced in this work opens the door to a rich landscape of research opportunities, offering a versatile simulation framework suitable for a diverse array of biomedical applications. The study of ultrasound-driven bubbles in blood vessels or bubble collapse is of importance to sonoporation where the mechanical stresses are assumed to contribute to membrane permeation. The case could be improved by considering an UCA. Bubbles can also be used to break down blood clots in thrombolysis. The bubble collapse in a blood vessel near a thrombus can be investigated to elucidate the damage mechanisms and the safety of such procedures. The collapse of a cloud of air cavities in tissues are used to mechanical ablate tissue in Histotripsy. The mechanical loading of the tissue during cloud expansion and collapse remains to be elucidated. Similarly, with the real-fluid EoS presented in this work, boiling histotripsy procedures could also be simulated to explain the thermal ablation process. Bubble clouds are also used in ESWL to fragment kidney stones. A bubble cloud simulation could explain the mechanical damage mechanism behind this procedure. Lastly, simulating needleless injection systems that are a new drug delivery system could improve their efficacy and their safety while minimizing discomfort. The penetration of a liquid jet into multiple layers of skin can be simulated with the presented methodology.

Several of numerical improvements can be made to include more physics, expand the scope of studies possible or port the model to other numerical methods. The current model could be improved by adding viscosity, surface tension, heat conduction, phase transition and plasticity. The presented methodology is density-based method suitable for high-Mach number flows typical to bubble collapses. The use of an AUSM+-up approximate Riemann solver could expand the scope of studies possible to low-Mach number flows if coupled with a high-order reconstruction method like WENO and a high-order temporal integration. Alternatively, the model equations could also be solved by a pressure-based approach to study incompressible flows with FSI or even the newer all-Mach approaches.

7 REFERENCES

[1] S. W. Ohl, E. Klaseboer, and B. C. Khoo, "Bubbles with shock waves and ultrasound: A review," *Interface Focus*, vol. 5, no. 5. Royal Society of London, pp. 1–15, Oct. 06, 2015. doi: 10.1098/rsfs.2015.0019.

[2] C. E. Brennen, "Cavitation in medicine.," *Interface Focus*, vol. 5, no. 5, p. 20150022, Oct. 2015, doi: 10.1098/rsfs.2015.0022.

[3] E. P. Stride and C. C. Coussios, "Cavitation and contrast: The use of bubbles in ultrasound imaging and therapy," *Proc Inst Mech Eng H*, vol. 224, no. 2, pp. 171–191, Feb. 2010, doi: 10.1243/09544119JEIM622.

[4] T. Faez *et al.*, "20 Years of Ultrasound Contrast Agent Modeling," *IEEE Trans Ultrason Ferroelectr Freq Control*, vol. 60, no. 1, Jan. 2013, doi: 10.1109/TUFFC.2013.2533.

[5] J. E. Kennedy, "High-intensity focused ultrasound in the treatment of solid tumours," *Nat Rev Cancer*, vol. 5, no. 4, pp. 321–327, Apr. 2005, doi: 10.1038/nrc1591.

[6] R. O. Illing *et al.*, "The safety and feasibility of extracorporeal high-intensity focused ultrasound (HIFU) for the treatment of liver and kidney tumours in a Western population," *Br J Cancer*, vol. 93, no. 8, pp. 890–895, Oct. 2005, doi: 10.1038/sj.bjc.6602803.

[7] V. A. Khokhlova *et al.*, "Histotripsy methods in mechanical disintegration of tissue: Towards clinical applications," *https://doi.org/10.3109/02656736.2015.1007538*, vol. 31, no. 2, pp. 145–162, Mar. 2015, doi: 10.3109/02656736.2015.1007538.

[8] Y. N. Wang, T. Khokhlova, M. Bailey, J. H. Hwang, and V. Khokhlova, "Histological and Biochemical Analysis of Mechanical and Thermal Bioeffects in Boiling Histotripsy Lesions Induced by High Intensity Focused Ultrasound," *Ultrasound Med Biol*, vol. 39, no. 3, pp. 424–438, Mar. 2013, doi: 10.1016/J.ULTRASMEDBIO.2012.10.012.

[9] A. Skolarikos, G. Alivizatos, and J. de la Rosette, "Extracorporeal Shock Wave Lithotripsy 25 Years Later: Complications and Their Prevention," *Eur Urol*, vol. 50, no. 5, pp. 981–990, Nov. 2006, doi: 10.1016/J.EURURO.2006.01.045.

[10] F. K. Benra, H. J. Dohmen, J. Pei, S. Schuster, and B. Wan, "A comparison of one-way and two-way coupling methods for numerical analysis of fluid-structure interactions," *J Appl Math*, vol. 2011, 2011, doi: 10.1155/2011/853560.

[11] A. J. Barlow, P. H. Maire, W. J. Rider, R. N. Rieben, and M. J. Shashkov, "Arbitrary Lagrangian–Eulerian methods for modeling high-speed compressible multimaterial flows," *J Comput Phys*, vol. 322, pp. 603–665, Oct. 2016, doi: 10.1016/J.JCP.2016.07.001.

[12] P. Vachal, R. V. Garimella, and M. J. Shashkov, "Untangling of 2D meshes in ALE simulations," *J Comput Phys*, vol. 196, no. 2, pp. 627–644, May 2004, doi: 10.1016/J.JCP.2003.11.011.

[13] W. Kim and H. Choi, "Immersed boundary methods for fluid-structure interaction: A review," *Int J Heat Fluid Flow*, vol. 75, pp. 301–309, Feb. 2019, doi: 10.1016/J.IJHEATFLUIDFLOW.2019.01.010.

[14] R. Mittal and G. Iaccarino, "IMMERSED BOUNDARY METHODS," *https://doi.org/10.1146/annurev.fluid.37.061903.175743*, vol. 37, pp. 239–261, Jan. 2005, doi: 10.1146/ANNUREV.FLUID.37.061903.175743.

[15] S. Ndanou, N. Favrie, and S. Gavrilyuk, "Multi-solid and multi-fluid diffuse interface model: Applications to dynamic fracture and fragmentation," *J Comput Phys*, vol. 295, pp. 523–555, Aug. 2015, doi: 10.1016/j.jcp.2015.04.024.

[16] N. S. Ghaisas, A. Subramaniam, and S. K. Lele, "A unified high-order Eulerian method for continuum simulations of fluid flow and of elastic–plastic deformations in solids," *J Comput Phys*, vol. 371, pp. 452–482, Oct. 2018, doi: 10.1016/j.jcp.2018.05.035.

[17] A. López Ortega, M. Lombardini, D. I. Pullin, and D. I. Meiron, "Numerical simulation of elastic-plastic solid mechanics using an Eulerian stretch tensor approach and HLLD Riemann solver," *J Comput Phys*, vol. 257, no. PA, pp. 414–441, 2014, doi: 10.1016/j.jcp.2013.10.007.

[18] P. T. Barton, "An interface-capturing Godunov method for the simulation of compressible solid-fluid problems," *J Comput Phys*, vol. 390, pp. 25–50, Aug. 2019, doi: 10.1016/j.jcp.2019.03.044.

[19] N. Favrie, S. L. Gavrilyuk, and R. Saurel, "Solid-fluid diffuse interface model in cases of extreme deformations," *J Comput Phys*, vol. 228, no. 16, pp. 6037–6077, Sep. 2009, doi: 10.1016/j.jcp.2009.05.015.

[20] I. Peshkov, M. Pavelka, E. Romenski, and M. Grmela, "Continuum mechanics and thermodynamics in the Hamilton and the Godunov-type formulations," *Continuum Mechanics and Thermodynamics*, vol. 30, no. 6, pp. 1343–1378, 2018, doi: 10.1007/s00161-018-0621-2.

[21] P. T. Barton, "A level-set based Eulerian method for simulating problems involving high strain-rate fracture and fragmentation," *Int J Impact Eng*, vol. 117, pp. 75–84, Jul. 2018, doi: 10.1016/j.ijimpeng.2018.03.002.

[22] S. Schoch, K. Nordin-Bates, and N. Nikiforakis, "An Eulerian algorithm for coupled simulations of elastoplastic-solids and condensed-phase explosives," *J Comput Phys*, vol. 252, pp. 163–194, Nov. 2013, doi: 10.1016/J.JCP.2013.06.020.

[23] A. López Ortega, M. Lombardini, D. I. Pullin, and D. I. Meiron, "Numerical simulations of the Richtmyer-Meshkov instability in solid-vacuum interfaces using calibrated plasticity laws," *Phys Rev E Stat Nonlin Soft Matter Phys*, vol. 89, no. 3, pp. 1–9, 2014, doi: 10.1103/PhysRevE.89.033018.

[24] P. T. Barton, B. Obadia, and D. Drikakis, "A conservative level-set based method for compressible solid/fluid problems on fixed grids," *J Comput Phys*, vol. 230, no. 21, pp. 7867–7890, Sep. 2011, doi: 10.1016/J.JCP.2011.07.008.

[25] N. Gokhale, N. Nikiforakis, and R. Klein, "A dimensionally split Cartesian cut cell method for hyperbolic conservation laws," *J Comput Phys*, vol. 364, pp. 186–208, Jul. 2018, doi: 10.1016/J.JCP.2018.03.005.

[26] G. H. H. Miller and P. Colella, "A Conservative Three-Dimensional Eulerian Method for Coupled Fluid-Solid Shock Capturing," *J Comput Phys*, vol. 183, no. 1, pp. 1–21, Nov. 2002, doi: 10.1006/JCPH.2002.7158.

[27] G. Allaire, S. Clerc, and S. Kokh, "A five-equation model for the numerical simulation of interfaces in two-phase flows," *Comptes Rendus de l'Académie des Sciences - Series I - Mathematics*, vol. 331, no. 12, pp. 1017–1022, Dec. 2000, doi: 10.1016/S0764-4442(00)01753-5.

[28] R. Saurel and C. Pantano, "Diffuse interfaces and capturing methods in compressible two-phase flow," *Annu Rev Fluid Mech*, vol. 50, no. 1, pp. 1–14, Jan. 2017, doi: 10.1146/)).

[29] R. Saurel, F. Petitpas, and R. A. Berry, "Simple and efficient relaxation methods for interfaces separating compressible fluids, cavitating flows and shocks in multiphase mixtures," *J Comput Phys*, vol. 228, pp. 1678–1712, 2009, doi: 10.1016/j.jcp.2008.11.002.

[30] M. Pelanti and K. M. Shyue, "A numerical model for multiphase liquid–vapor–gas flows with interfaces and cavitation," *International Journal of Multiphase Flow*, vol. 113, pp. 208–230, 2019, doi: 10.1016/j.ijmultiphaseflow.2019.01.010.

[31] G. Nykteri and M. Gavaises, "Numerical modeling of droplet rim fragmentation by laser-pulse impact using a multiscale two-fluid approach," *Phys Rev Fluids*, vol. 7, no. 10, p. 103604, Oct. 2022, doi: 10.1103/PHYSREVFLUIDS.7.103604/FIGURES/17/MEDIUM.

[32] V. Maltsev, M. Skote, and P. Tsoutsanis, "High-order methods for diffuse-interface models in compressible multi-medium flows: A review," *Physics of Fluids*, vol. 34, no. 2, 2022, doi: 10.1063/5.0077314.

[33] A. K. Kapila, R. Menikoff, J. B. Bdzil, S. F. Son, and D. S. Stewart, "Two-phase modeling of deflagration-to-detonation transition in granular materials: Reduced equations," *Physics of Fluids*, vol. 13, no. 10, pp. 3002–3024, Oct. 2001, doi: 10.1063/1.1398042.

[34] K. Schmidmayer, S. H. Bryngelson, and T. Colonius, "An assessment of multicomponent flow models and interface capturing schemes for spherical bubble dynamics," Mar. 2019, Accessed: Jul. 09, 2019. [Online]. Available: http://arxiv.org/abs/1903.08242

[35] V. Coralic and T. Colonius, "Finite-volume WENO scheme for viscous compressible multicomponent flows," *J Comput Phys*, vol. 274, pp. 95–121, 2014, doi: 10.1016/j.jcp.2014.06.003.

[36] V. Coralic and T. Colonius, "Shock-induced collapse of a bubble inside a deformable vessel.," *Eur J Mech B Fluids*, vol. 40, pp. 64–74, Jul. 2013, doi: 10.1016/j.euromechflu.2013.01.003.

[37] S. Bidi, P. Koukouvinis, A. Papoutsakis, A. Shams, and M. Gavaises, "Numerical study of real gas effects during bubble collapse using a disequilibrium multiphase model," *Ultrason Sonochem*, vol. 90, p. 106175, Nov. 2022, doi: 10.1016/J.ULTSONCH.2022.106175.

[38] N. Kyriazis, P. Koukouvinis, and M. Gavaises, "Numerical investigation of bubble dynamics using tabulated data," *International Journal of Multiphase Flow*, vol. 93, pp. 158–177, Jul. 2017, doi: 10.1016/J.IJMULTIPHASEFLOW.2017.04.004.

[39] A. Theodorakakos, G. Strotos, N. Mitroglou, C. Atkin, and M. Gavaises, "Friction-induced heating in nozzle hole micro-channels under extreme fuel pressurisation," *Fuel*, vol. 123, pp. 143–150, May 2014, doi: 10.1016/J.FUEL.2014.01.050.

[40] M. G. Mithun, P. Koukouvinis, and M. Gavaises, "Numerical simulation of cavitation and atomization using a fully compressible three-phase model," *Phys Rev Fluids*, vol. 3, no. 6, p. 064304, Jun. 2018, doi: 10.1103/PHYSREVFLUIDS.3.064304/FIGURES/13/THUMBNAIL.

[41] M. Gavaises, M. Murali-Girija, C. Rodriguez, P. Koukouvinis, M. Gold, and R. Pearson, "Numerical simulation of fuel dribbling and nozzle wall wetting," *International Journal of Engine Research*, vol. 23, no. 1, pp. 132–149, Jan. 2022, doi: 10.1177/1468087420985189/ASSET/IMAGES/LARGE/10.1177_1468087420985189-FIG15.JPEG.

[42] E. Gomez Santos, J. Shi, R. Venkatasubramanian, G. Hoffmann, M. Gavaises, and W. Bauer, "Modelling and prediction of cavitation erosion in GDi injectors operated with E100 fuel," *Fuel*, vol. 289, p. 119923, Apr. 2021, doi: 10.1016/J.FUEL.2020.119923.

[43] E. Gomez Santos, J. Shi, M. Gavaises, C. Soteriou, M. Winterbourn, and W. Bauer, "Investigation of cavitation and air entrainment during pilot injection in real-size multi-

hole diesel nozzles," *Fuel*, vol. 263, p. 116746, Mar. 2020, doi: 10.1016/J.FUEL.2019.116746.

[44] P. Koukouvinis, N. Mitroglou, M. Gavaises, M. Lorenzi, and M. Santini, "Quantitative predictions of cavitation presence and erosion-prone locations in a high-pressure cavitation test rig," *J Fluid Mech*, vol. 819, pp. 21–57, May 2017, doi: 10.1017/JFM.2017.156.

[45] "Evaluation of an Eulerian multi-material mixture formulation based on a single inverse deformation gradient tensor field (Journal Article) | OSTI.GOV." Accessed: Aug. 12, 2023. [Online]. Available: https://www.osti.gov/biblio/1423820

[46] A. Murrone and H. Guillard, "A five equation reduced model for compressible two phase flow problems," *J Comput Phys*, vol. 202, no. 2, pp. 664–698, 2005, doi: 10.1016/j.jcp.2004.07.019.

[47] A. Shams, S. Bidi, and M. Gavaises, "Investigation of the ultrasound-induced collapse of air bubbles near soft materials," *Ultrason Sonochem*, vol. 102, p. 106723, Jan. 2024, doi: 10.1016/J.ULTSONCH.2023.106723.

[48] S. Bidi, P. Koukouvinis, A. Papoutsakis, A. Shams, and M. Gavaises, "Numerical study of real gas effects during bubble collapse using a disequilibrium multiphase model," *Ultrason Sonochem*, vol. 90, p. 106175, Nov. 2022, doi: 10.1016/J.ULTSONCH.2022.106175.

[49] E. Klaseboer and B. C. Khoo, "Boundary integral equations as applied to an oscillating bubble near a fluid-fluid interface," *Comput Mech*, vol. 33, no. 2, pp. 129–138, Jan. 2004, doi: 10.1007/s00466-003-0508-2.

[50] E. Klaseboer and B. C. Khoo, "An oscillating bubble near an elastic material," *J Appl Phys*, vol. 96, no. 10, pp. 5808–5818, Nov. 2004, doi: 10.1063/1.1803925.

[51] E.-A. BRUJAN, K. NAHEN, P. SCHMIDT, and A. VOGEL, "Dynamics of laser-induced cavitation bubbles near an elastic boundary," *J Fluid Mech*, vol. 433, pp. 251–281, Apr. 2001, doi: 10.1017/S0022112000003347.

[52] J. B. Freund, R. K. Shukla, and A. P. Evan, "Shock-induced bubble jetting into a viscous fluid with application to tissue injury in shock-wave lithotripsy," *J Acoust Soc Am*, vol. 126, no. 5, pp. 2746–2756, Nov. 2009, doi: 10.1121/1.3224830.

[53] K. Kobayashi, T. Kodama, and H. Takahira, "Shock wave-bubble interaction near soft and rigid boundaries during lithotripsy: Numerical analysis by the improved ghost fluid method," *Phys Med Biol*, vol. 56, no. 19, pp. 6421–6440, Oct. 2011, doi: 10.1088/0031-9155/56/19/016.

[54] C. K. Turangan, G. P. Ong, E. Klaseboer, and B. C. Khoo, "Experimental and numerical study of transient bubble-elastic membrane interaction," *J Appl Phys*, vol. 100, no. 5, p. 054910, Sep. 2006, doi: 10.1063/1.2338125.

[55] S. W. Fong, E. Klaseboer, C. K. Turangan, B. C. Khoo, and K. C. Hung, "Numerical analysis of a gas bubble near bio-materials in an ultrasound field," *Ultrasound Med Biol*, vol. 32, no. 6, pp. 925–942, Jun. 2006, doi: 10.1016/j.ultrasmedbio.2006.03.005.

[56] G. A. Curtiss, D. M. Leppinen, Q. X. Wang, and J. R. Blake, "Ultrasonic cavitation near a tissue layer," *J Fluid Mech*, vol. 730, pp. 245–272, Sep. 2013, doi: 10.1017/jfm.2013.341.

[57] C. Chen, Y. Gu, J. Tu, X. Guo, and D. Zhang, "Microbubble oscillating in a microvessel filled with viscous fluid: A finite element modeling study," *Ultrasonics*, vol. 66, pp. 54–64, Mar. 2016, doi: 10.1016/J.ULTRAS.2015.11.010.

[58] S. P. Wang, Q. X. Wang, D. M. Leppinen, A. M. Zhang, and Y. L. Liu, "Acoustic bubble dynamics in a microvessel surrounded by elastic material," *Physics of Fluids*, vol. 30, no. 1, p. 012104, Jan. 2018, doi: 10.1063/1.5005534.

[59] S. Cao, G. Wang, O. Coutier-Delgosha, and K. Wang, "Shock-induced bubble collapse near solid materials: effect of acoustic impedance," *J Fluid Mech*, vol. 907, 2021, doi: 10.1017/jfm.2020.810.

[60] E. Koukas, A. Papoutsakis, and M. Gavaises, "Numerical investigation of shock-induced bubble collapse dynamics and fluid–solid interactions during shock-wave lithotripsy," *Ultrason Sonochem*, vol. 95, p. 106393, May 2023, doi: 10.1016/J.ULTSONCH.2023.106393.

[61] S. Ndanou, "Etude Mathématique et Numérique des Modèles Hyperélastiques et Visco-plastiques:Applications aux Impacts Hypervéloces," 2017.

[62] P. S. Yarmolenko *et al.*, "Thresholds for thermal damage to normal tissues: An update," *Int J Hyperthermia*, vol. 27, no. 4, p. 320, Jun. 2011, doi: 10.3109/02656736.2010.534527.

[63] G. R. Ter Haar, "High Intensity Focused Ultrasound for the Treatment of Tumors," *Echocardiography*, vol. 18, no. 4, pp. 317–322, May 2001, doi: 10.1046/J.1540-8175.2001.00317.X.

[64] R. G. Holt and R. A. Roy, "Measurements of bubble-enhanced heating from focused, mhz-frequency ultrasound in a tissue-mimicking material," *Ultrasound Med Biol*, vol. 27, no. 10, pp. 1399–1412, Oct. 2001, doi: 10.1016/S0301-5629(01)00438-0.

[65] X. Ma, X. Zhao, B. Huang, X. Fu, and G. Wang, "Physical investigation of non-spherical bubble collapse near a rigid boundary," 2019.

[66] W. Wu, B. Wang, and G. Xiang, "Impingement of high-speed cylindrical droplets embedded with an air/vapour cavity on a rigid wall: Numerical analysis," *J Fluid Mech*, vol. 864, pp. 1058–1087, 2019, doi: 10.1017/jfm.2019.55.

[67] T. Kondo and K. Ando, "Simulation of high-speed droplet impact against a dry/wet rigid wall for understanding the mechanism of liquid jet cleaning," *Physics of Fluids*, vol. 31, no. 1, p. 13303, 2019.

[68] R. Dubois, E. Goncalves da Silva, and P. Parnaudeau, "High performance computing of stiff bubble collapse on CPU-GPU heterogeneous platform," *Computers and Mathematics with Applications*, vol. 99, pp. 246–256, 2021, doi: 10.1016/j.camwa.2021.07.010.

[69] T. Trummler, S. H. Bryngelson, K. Schmidmayer, S. J. Schmidt, T. Colonius, and N. A. Adams, "Near-surface dynamics of a gas bubble collapsing above a crevice," *J Fluid Mech*, vol. 899, 2020.

[70] E. Koukas, A. Papoutsakis, and M. Gavaises, "Numerical investigation of shock-induced bubble collapse dynamics and fluid–solid interactions during shock-wave lithotripsy," *Ultrason Sonochem*, vol. 95, p. 106393, May 2023, doi: 10.1016/J.ULTSONCH.2023.106393.

[71] A. Mishra, J. Mondal, A. Roy, R. Lakkaraju, and P. Ghosh, "Jet and shock characteristics of collapsing cavitating bubble in cryogenic environment," *Indian Journal of Cryogenics*, vol. 45, no. 1, pp. 19–24, 2020, doi: 10.5958/2349-2120.2020.00002.3.

[72] X. Ma *et al.*, "Numerical simulation of single bubble dynamics under acoustic travelling waves," *Ultrason Sonochem*, vol. 42, no. December 2017, pp. 619–630, 2018, doi: 10.1016/j.ultsonch.2017.12.021.

[73] S. Qiu, X. Ma, B. Huang, D. Li, G. Wang, and M. Zhang, "Numerical simulation of single bubble dynamics under acoustic standing waves," *Ultrason Sonochem*, vol. 49, no. May, pp. 196–205, 2018, doi: 10.1016/j.ultsonch.2018.08.006.

[74] Q. Nguyen, V. Nguyen, T. Phan, T. Duy, S. Park, and W. Park, "Numerical study of dynamics of cavitation bubble collapse near oscillating walls Numerical study of dynamics of cavitation bubble collapse near oscillating walls," vol. 013306, no. January, 2023, doi: 10.1063/5.0132049.

[75] P. Koukouvinis *et al.*, "Parametric Investigations of the Induced Shear Stress by a Laser-Generated Bubble," *Langmuir*, vol. 34, no. 22, pp. 6428–6442, 2018, doi: 10.1021/acs.langmuir.8b01274.

[76] S. Y. Tong, S. P. Wang, S. Yan, and S. Li, "Fluid-structure interactions between a near-field underwater explosion bubble and a suspended plate," *AIP Adv*, vol. 12, no. 9, 2022, doi: 10.1063/5.0107299.

[77] A. Papoutsakis, P. Koukouvinis, and M. Gavaises, "Solution of cavitating compressible flows using Discontinuous Galerkin discretisation," *J Comput Phys*, vol. 410, p. 109377, Jun. 2020, doi: 10.1016/J.JCP.2020.109377.

[78] M. L. Huber, E. W. Lemmon, I. H. Bell, and M. O. McLinden, "The NIST REFPROP Database for Highly Accurate Properties of Industrially Important Fluids," *Ind Eng Chem Res*, vol. 61, no. 42, pp. 15449–15472, Oct. 2022, doi: 10.1021/ACS.IECR.2C01427.

[79] D. Y. Peng and D. B. Robinson, "A New Two-Constant Equation of State," *Industrial and Engineering Chemistry Fundamentals*, vol. 15, no. 1, pp. 59–64, 1976, doi: 10.1021/I160057A011/ASSET/I160057A011.FP.PNG_V03.

[80] M. Cismondi and J. Mollerup, "Development and application of a three-parameter RK-PR equation of state," *Fluid Phase Equilib*, vol. 232, no. 1–2, pp. 74–89, 2005, doi: 10.1016/j.fluid.2005.03.020.

[81] O. Le Métayer, R. Saurel, O. Le Métayer, R. Saurel, and T. N. Stiffened-gas, "The Noble-Abel Stiffened-Gas equation of state To cite this version : HAL Id : hal-01305974 The Noble-Abel Stiffened-Gas Equation of State," 2016.

[82] J. Chandran R and A. Salih, "A modified equation of state for water for a wide range of pressure and the concept of water shock tube," *Fluid Phase Equilib*, vol. 483, pp. 182–188, 2019, doi: 10.1016/j.fluid.2018.11.032.

[83] S. A. Beig, B. Aboulhasanzadeh, and E. Johnsen, "Temperatures produced by inertially collapsing bubbles near rigid surfaces," *J Fluid Mech*, vol. 852, pp. 105–125, 2018, doi: 10.1017/jfm.2018.525.

[84] C. Peng, S. Tian, G. Li, and M. C. Sukop, "Simulation of laser-produced single cavitation bubbles with hybrid thermal Lattice Boltzmann method," *Int J Heat Mass Transf*, vol. 149, p. 119136, Mar. 2020, doi: 10.1016/J.IJHEATMASSTRANSFER.2019.119136.

[85] Q. Yu, X. Ma, Z. Xu, J. Zhao, D. Wang, and Z. Huang, "Thermodynamic effect of single bubble near a rigid wall," *Ultrason Sonochem*, vol. 71, p. 105396, Mar. 2021, doi: 10.1016/J.ULTSONCH.2020.105396.

[86] M. R. Baer and J. W. Nunziato, "A two-phase mixture theory for the deflagration-to-detonation transition (ddt) in reactive granular materials," *International Journal of Multiphase Flow*, vol. 12, no. 6, pp. 861–889, Nov. 1986, doi: 10.1016/0301-9322(86)90033-9.

[87] E. Goncalves Da Silva and P. Parnaudeau, "Numerical study of pressure loads generated by a shock-induced bubble collapse," *Physics of Fluids*, vol. 33, no. 11, Nov. 2021, doi: 10.1063/5.0069332/1063604.

[88] H. Wu *et al.*, "Influence of Surface Tension on Dynamic Characteristics of Single Bubble in Free-Field Exposed to Ultrasound," *Micromachines 2022, Vol. 13, Page 782*, vol. 13, no. 5, p. 782, May 2022, doi: 10.3390/MI13050782.

[89] T. H. Phan, V. T. Nguyen, T. N. Duy, D. H. Kim, and W. G. Park, "Influence of phase-change on the collapse and rebound stages of a single spark-generated cavitation

bubble," *Int J Heat Mass Transf*, vol. 184, p. 122270, Mar. 2022, doi: 10.1016/J.IJHEATMASSTRANSFER.2021.122270.

[90] S. Bidi, P. Koukouvinis, A. Papoutsakis, A. Shams, and M. Gavaises, "Numerical study of real gas effects during bubble collapse using a disequilibrium multiphase model," *Ultrason Sonochem*, vol. 90, no. September, p. 106175, 2022, doi: 10.1016/j.ultsonch.2022.106175.

[91] N. Kyriazis, P. Koukouvinis, and M. Gavaises, "Numerical investigation of bubble dynamics using tabulated data," vol. 93, pp. 158–177, 2017, doi: 10.1016/j.ijmultiphaseflow.2017.04.004.

[92] M. J. Ivings, D. M. Causon, and E. F. Toro, "On Riemann solvers for compressible liquids," *Int J Numer Methods Fluids*, vol. 28, no. 3, pp. 395–418, 1998, doi: 10.1002/(SICI)1097-0363(19980915)28:3<395::AID-FLD718>3.0.CO;2-S.

[93] P. A. Thompson and G. S. Beavers, "Compressible-fluid dynamics," 1972.

[94] W. Wagner and H.-J. Kretzschmar, *International Steam Tables-Properties of Water and Steam based on the Industrial Formulation IAPWS-IF97: Tables, Algorithms, Diagrams, and CD-ROM Electronic Steam Tables-All of the equations of IAPWS-IF97 including a complete set of supplementary backward*. Springer Science & Business Media, 2007.

[95] D. E. Winterbone and A. Turan, "General Thermodynamic Relationships," in *Advanced Thermodynamics for Engineers*, Elsevier, 2015, pp. 141–162. doi: 10.1016/B978-0-444-63373-6.00007-1.

[96] H. Nazari-Mahroo, K. Pasandideh, H. A. Navid, and R. Sadighi-Bonabi, "Influence of liquid compressibility on the dynamics of single bubble sonoluminescence," *Phys Lett A*, vol. 382, no. 30, pp. 1962–1967, Aug. 2018, doi: 10.1016/j.physleta.2018.04.058.

[97] F. Denner, "The Gilmore-NASG model to predict single-bubble cavitation in compressible liquids," *Ultrason Sonochem*, vol. 70, no. May 2020, p. 105307, 2021, doi: 10.1016/j.ultsonch.2020.105307.

[98] P. Koukouvinis, M. Gavaises, O. Supponen, and M. Farhat, "Numerical simulation of a collapsing bubble subject to gravity," *Physics of Fluids*, vol. 28, no. 3, 2016, doi: 10.1063/1.4944561.

[99] Q. Zeng, S. R. Gonzalez-Avila, R. Dijkink, P. Koukouvinis, M. Gavaises, and C.-D. Ohl, "Wall shear stress from jetting cavitation bubbles," *J Fluid Mech*, vol. 846, pp. 341–355, Jul. 2018, doi: 10.1017/jfm.2018.286.

[100] M. Koch, J. M. Rosselló, C. Lechner, W. Lauterborn, and R. Mettin, "Dynamics of a Laser-Induced Bubble above the Flat Top of a Solid Cylinder—Mushroom-Shaped Bubbles and the Fast Jet," *Fluids*, vol. 7, no. 1, p. 2, Dec. 2021, doi: 10.3390/fluids7010002.

[101] J. H. Dymond and R. Malhotra, "The Tait equation: 100 years on," *Int J Thermophys*, vol. 9, no. 6, pp. 941–951, 1988, doi: 10.1007/BF01133262.

[102] A. H. Koop, "Numerical Simulation of Unsteady Three-Dimensional Sheet Cavitation," University of Twente, 2008.

[103] R. Saurel, J. P. Cocchi, and P. B. Butler, "Numerical study of cavitation in the wake of a hypervelocity underwater projectile," *J Propuls Power*, vol. 15, no. 4, pp. 513–522, 1999, doi: 10.2514/2.5473.

[104] E. Goncalves, Y. Hoarau, and D. Zeidan, "Simulation of shock-induced bubble collapse using a four-equation model," *Shock Waves*, vol. 29, no. 1, pp. 221–234, Jan. 2019, doi: 10.1007/s00193-018-0809-1.

[105] J. Zhang, T. L. Jackson, and A. M. D. Jost, "Effects of air chemistry and stiffened EOS of air in numerical simulations of bubble collapse in water," *Phys Rev Fluids*, vol. 2, no. 5, p. 053603, May 2017, doi: 10.1103/PhysRevFluids.2.053603.

[106] T. Flatten, A. Morin, and S. T. Munkejord, "On solutions to equilibrium problems for systems of stiffened gases," *SIAM J Appl Math*, vol. 71, no. 1, pp. 41–67, 2011, doi: 10.1137/100784321.

[107] W. Wagner and A. Pruß, "The IAPWS Formulation 1995 for the Thermodynamic Properties of Ordinary Water Substance for General and Scientific Use," *J Phys Chem Ref Data*, vol. 31, no. 2, pp. 387–535, Jun. 2002, doi: 10.1063/1.1461829.

[108] E. W. Lemmon, I. H. Bell, M. L. Huber, and M. O. McLinden, "NIST Standard Reference Database 23: Reference Fluid Thermodynamic and Transport Properties-REFPROP, Version 10.0, National Institute of Standards and Technology," 2018, doi: https://doi.org/10.18434/T4/1502528.

[109] P. Koukouvinis, A. Vidal-Roncero, C. Rodriguez, M. Gavaises, and L. Pickett, "High pressure/high temperature multiphase simulations of dodecane injection to nitrogen: Application on ECN Spray-A," *Fuel*, vol. 275, p. 117871, 2020.

[110] E. F. Toro, *Riemann solvers and numerical methods for fluid dynamics: a practical introduction*. Springer Science & Business Media, 2013.

[111] A. López Ortega, M. Lombardini, D. I. Pullin, and D. I. Meiron, "Numerical simulation of elastic–plastic solid mechanics using an Eulerian stretch tensor approach and HLLD Riemann solver," *J Comput Phys*, vol. 257, no. PA, pp. 414–441, Jan. 2014, doi: 10.1016/J.JCP.2013.10.007.

[112] E. Johnsen and T. Colonius, "Implementation of WENO schemes in compressible multicomponent flow problems," *J Comput Phys*, vol. 219, no. 2, pp. 715–732, Dec. 2006, doi: 10.1016/J.JCP.2006.04.018.

[113] K. Schmidmayer, F. Petitpas, S. Le Martelot, and É. Daniel, "ECOGEN: An open-source tool for multiphase, compressible, multiphysics flows ☆,☆☆," *Comput Phys Commun*, vol. 251, p. 107093, 2020, doi: 10.17632/5bvx4g39dw.1.

[114] W. Zhang, A. Almgren, and V. Beckner, "AMReX: a framework for block-structured adaptive mesh refinement," *The Journal of Open Source Software*, vol. 4, no. 37, 2019, doi: 10.21105/joss.01370.

[115] W. Zhang, A. Myers, K. Gott, A. Almgren, and J. Bell, "AMReX: Block-structured adaptive mesh refinement for multiphysics applications," *International Journal of High Performance Computing Applications*, vol. 35, no. 6, pp. 508–526, Nov. 2021, doi: 10.1177/10943420211022811/ASSET/IMAGES/LARGE/10.1177_10943420211022811-FIG9.JPEG.

[116] M. J. Berger and P. Colella, "Local adaptive mesh refinement for shock hydrodynamics," *J Comput Phys*, vol. 82, no. 1, pp. 64–84, May 1989, doi: 10.1016/0021-9991(89)90035-1.

[117] J. B. Keller and M. Miksis, "Bubble oscillations of large amplitude," *J Acoust Soc Am*, vol. 68, no. 2, pp. 628–633, Aug. 1980, doi: 10.1121/1.384720.

[118] C. E. Brennen, *Cavitation and bubble dynamics*. Cambridge university press, 2014.

[119] J. Bezanson, S. Karpinski, V. B. Shah, and A. Edelman, "Julia: A Fast Dynamic Language for Technical Computing," Sep. 2012, Accessed: Jul. 25, 2023. [Online]. Available: https://arxiv.org/abs/1209.5145v1

[120] C. Rackauckas and Q. Nie, "DifferentialEquations.jl – A Performant and Feature-Rich Ecosystem for Solving Differential Equations in Julia," *J Open Res Softw*, 2017.

[121] A. T. de Hoop and J. H. van der Hijden, "Generation of acoustic waves by an impulsive point source in a fluid/solid configuration with a plane boundary," *J Acoust Soc Am*, vol. 75, no. 6, pp. 1709–1715, Jun. 1984, doi: 10.1121/1.390970.

[122] J. Diaz, A. Ezziani, and N. Legoff, "Gar6more3D." 2013.

[123] E. Johnsen and T. Colonius, "Shock-induced collapse of a gas bubble in shockwave lithotripsy," *J Acoust Soc Am*, vol. 124, no. 4, p. 2011, Oct. 2008, doi: 10.1121/1.2973229.

[124] C. C. Church, "A theoretical study of cavitation generated by an extracorporeal shock wave lithotripter," *J Acoust Soc Am*, vol. 86, no. 1, pp. 215–227, Jul. 1989, doi: 10.1121/1.398328.

[125] B. Dollet, P. Marmottant, and V. Garbin, "Bubble Dynamics in Soft and Biological Matter," *Annu Rev Fluid Mech*, vol. 51, no. 1, pp. 331–355, Jan. 2019, doi: 10.1146/annurev-fluid-010518-040352.

[126] A. M. Handorf, Y. Zhou, M. A. Halanski, and W. J. Li, "Tissue Stiffness Dictates Development, Homeostasis, and Disease Progression," *http://dx.doi.org/10.1080/15476278.2015.1019687*, vol. 11, no. 1, pp. 1–15, Jan. 2015, doi: 10.1080/15476278.2015.1019687.

[127] L. Mancia *et al.*, "Modeling tissue-selective cavitation damage," *Phys Med Biol*, vol. 64, no. 22, p. 225001, Nov. 2019, doi: 10.1088/1361-6560/AB5010.

[128] M. Cristofaro, W. Edelbauer, P. Koukouvinis, and M. Gavaises, "A numerical study on the effect of cavitation erosion in a diesel injector," *Appl Math Model*, vol. 78, pp. 200–216, Feb. 2020, doi: 10.1016/J.APM.2019.09.002.

[129] F. A. Godínez, R. Mayén-Mondragón, J. E. V. Guzmán, O. Chávez, M. Gavaises, and R. Montoya, "Bioinspired snapping-claw apparatus to study hydrodynamic cavitation

effects on the corrosion of metallic samples," *Review of Scientific Instruments*, vol. 91, no. 6, Jun. 2020, doi: 10.1063/5.0007069/965928.

[130] E. Gomez Santos, J. Shi, R. Venkatasubramanian, G. Hoffmann, M. Gavaises, and W. Bauer, "Modelling and prediction of cavitation erosion in GDi injectors operated with E100 fuel," *Fuel*, vol. 289, p. 119923, Apr. 2021, doi: 10.1016/J.FUEL.2020.119923.

[131] N. Mitroglou, M. Lorenzi, M. Santini, and M. Gavaises, "Application of X-ray micro-computed tomography on high-speed cavitating diesel fuel flows," *Exp Fluids*, vol. 57, no. 11, pp. 1–14, Nov. 2016, doi: 10.1007/S00348-016-2256-Z/FIGURES/9.

[132] P. Koukouvinis, N. Mitroglou, M. Gavaises, M. Lorenzi, and M. Santini, "Quantitative predictions of cavitation presence and erosion-prone locations in a high-pressure cavitation test rig," *J Fluid Mech*, vol. 819, pp. 21–57, May 2017, doi: 10.1017/JFM.2017.156.

[133] S. J. Shaw, W. P. Schiffers, T. P. Gentry, and D. C. Emmony, "The interaction of a laser-generated cavity with a solid boundary," *J Acoust Soc Am*, vol. 107, no. 6, pp. 3065–3072, Jun. 2000, doi: 10.1121/1.429335.

[134] G. N. Sankin and P. Zhong, "Interaction between shock wave and single inertial bubbles near an elastic boundary," *Phys Rev E Stat Nonlin Soft Matter Phys*, vol. 74, no. 4 Pt 2, p. 046304, 2006, doi: 10.1103/PHYSREVE.74.046304.

[135] Y. Fung, *Biomechanics: mechanical properties of living tissues*. Springer Science & Business Media, 2013.

[136] R. W. Ogden and G. A. Holzapfel, *Mechanics of biological tissue*. Springer, 2006.

[137] S. C. Cowin, *Bone mechanics handbook*. CRC press, 2001.

[138] J. D. Humphrey and S. L. Delange, "An introduction to biomechanics," *Solids and Fluids, Analysis and Design. Springer, Heidelberg*, 2004.

[139] T. Kodama and K. Takayama, "Dynamic behavior of bubbles during extracorporeal shock-wave lithotripsy," *Ultrasound Med Biol*, vol. 24, no. 5, pp. 723–738, Jun. 1998, doi: 10.1016/S0301-5629(98)00022-2.

[140] E.-A. BRUJAN, K. NAHEN, P. SCHMIDT, and A. VOGEL, "Dynamics of laser-induced cavitation bubbles near elastic boundaries: influence of the elastic modulus," *J Fluid Mech*, vol. 433, pp. 283–314, Apr. 2001, doi: 10.1017/S0022112000003335.

[141] A. B. Sieber, D. B. Preso, and M. Farhat, "Cavitation bubble dynamics and microjet atomization near tissue-mimicking materials," *Physics of Fluids*, vol. 35, no. 2, p. 27101, Feb. 2023, doi: 10.1063/5.0136577/2869190.

[142] A. Philipp, M. Delius, C. Scheffczyk, A. Vogel, and W. Lauterborn, "Interaction of lithotripter-generated shock waves with air bubbles," *J Acoust Soc Am*, vol. 93, no. 5, pp. 2496–2509, May 1993, doi: 10.1121/1.406853.

[143] J. J. Quirk and S. Karni, "On the dynamics of a shock–bubble interaction," *J Fluid Mech*, vol. 318, pp. 129–163, Jul. 1996, doi: 10.1017/S0022112096007069.

[144] T. Kodama and Y. Tomita, "Cavitation bubble behavior and bubble-shock wave interaction near a gelatin surface as a study of in vivo bubble dynamics," *Appl Phys B*, vol. 70, no. 1, pp. 139–149, Jan. 2000, doi: 10.1007/s003400050022.

[145] P. Prentice, A. Cuschieri, K. Dholakia, M. Prausnitz, and P. Campbell, "Membrane disruption by optically controlled microbubble cavitation," *Nat Phys*, vol. 1, no. 2, pp. 107–110, Nov. 2005, doi: 10.1038/nphys148.

[146] Richard Saurel, F. Petitpas, and R. A. Berry, "Simple and efficient relaxation methods for interfaces separating compressible fluids, cavitating flows and shocks in multiphase mixtures," *J Comput Phys*, vol. 228, no. 5, pp. 1678–1712, 2009, doi: 10.1016/j.jcp.2008.11.002.

[147] C. E. Brennen, *Cavitation and bubble dynamics*. 2014. doi: 10.1017/CBO9781107338760.

[148] D. L. Sokolov, M. R. Bailey, L. A. Crum, P. M. Blomgren, B. A. Connors, and A. P. Evan, "Prefocal alignment improves stone comminution in shockwave lithotripsy," *J Endourol*, vol. 16, no. 10, pp. 709–715, 2002.

[149] M. R. Bailey, V. A. Khokhlova, O. A. Sapozhnikov, S. G. Kargl, and L. A. Crum, "Physical mechanisms of the therapeutic effect of ultrasound (a review)," *Acoust Phys*, vol. 49, pp. 369–388, 2003.

[150] E. Johnsen and T. Colonius, “Shock-induced collapse of a gas bubble in shockwave lithotripsy,” *J Acoust Soc Am*, vol. 124, no. 4, pp. 2011–2020, 2008, doi: 10.1121/1.2973229.

[151] A. R. Moritz and F. C. Henriques Jr, “Studies of thermal injury: II. The relative importance of time and surface temperature in the causation of cutaneous burns,” *Am J Pathol*, vol. 23, no. 5, p. 695, 1947.

[152] M. Cismondi and J. Mollerup, “Development and application of a three-parameter RK–PR equation of state,” *Fluid Phase Equilib*, vol. 232, no. 1–2, pp. 74–89, May 2005, doi: 10.1016/J.FLUID.2005.03.020.

[153] E. Vlaisavljevich *et al.*, “Effects of tissue stiffness, ultrasound frequency, and pressure on histotripsy-induced cavitation bubble behavior,” *Phys Med Biol*, vol. 60, no. 6, p. 2271, Feb. 2015, doi: 10.1088/0031-9155/60/6/2271.

[154] S. A. Beig, B. Aboulhasanzadeh, and E. Johnsen, “Temperatures produced by inertially collapsing bubbles near rigid surfaces,” *J Fluid Mech*, vol. 852, pp. 105–125, Oct. 2018, doi: 10.1017/JFM.2018.525.